An Iron-Based Photoelectrode

Von der Naturwissenschaftlichen Fakultät der

Gottfried Wilhelm Leibniz Universität Hannover

zur Erlangung des Grades

Doktor der Naturwissenschaften (Dr. rer. nat)

genehmigte Dissertation

von

Luis Ignacio Granone, Licenciado en Química (Argentinien)

2019

Referent: Prof. Dr. rer. nat. Detlef W. Bahnemann

Korreferentin: Prof. Dr. rer. nat. Nadja-C. Bigall

Korreferentin: Prof. Dr. Cecilia B. Mendive

Tag der Promotion: 25.03.2019

For my Family

Acknowledgments

At this point, I would like to acknowledge

Prof. Dr. Detlef Bahnemann for granting me the opportunity to conduct my doctoral studies within his research group. I thank him for supporting me and giving me absolute freedom for developing my research work.

Dr. Ralf Dillert for his guidance and for being always willing to discuss scientific questions. I thank him for showing me what science is and for sharing his enormous knowledge and experience.

Prof. Dr. Thomas Scheper for giving me the opportunity to conduct my doctoral studies at the Institute of Technical Chemistry and for his willingness to accept being the Chair of the Examination Board.

Prof. Dr. Cecilia Mendive for being my first contact with academic science and for showing me her passion for Chemistry. I thank her for agreeing to be one of the co-referees of this thesis. I would also like to acknowledge the members of Prof. Dr. Mendive's research group, especially Dr. Mariano Curti for his support.

Prof. Dr. Nadja Bigall for accepting to be one of the co-referees of this thesis.

My current and former colleagues from Prof. Dr. Bahnemann's group for their cooperation and support. I am specially thankful to Dr. Jenny Schneider for her invaluable help and assistance during the beginning of my doctoral studies and during my stay in Hannover.

Prof. Dr. Thorsten Gesing, Prof. Dr. Thomas Bredow, Prof. Dr. Paul Heitjans, Prof. Dr. Alexei Emeline, Prof. Dr. Franz Renz, Dr. Lars Robben, Anna Ulpe, Stephen Klimke, Moritz Jahns, and Konstantin Nikitin for their scientific cooperation.

My family for their support during my doctoral studies. Special thanks go to my wife Melisa for being always by my side, and to our daughter Maite. Thank you.

Kurzzusammenfassung

Der Spinell $ZnFe_2O_4$ (ZFO) ist ein eisenbasierter Halbleiter, der in Hinblick auf die Anwendung als Photoanodenmaterial für die photoelektrochemische Wasserspaltung in Tandemzellen intensiv untersucht wird. Die für die photoelektrochemische Wasseroxidation an ZFO-Photoanoden berichteten Wirkungsgrade liegen derzeit jedoch etwa eine Größenordnung unter dem theoretisch erreichbaren Maximalwert. Darüber hinaus zeigen die veröffentlichten Wirkungsgrade eine große Streuung zwischen den auf verschiedenen Wegen hergestellten ZFO-Photoanoden sowie eine schlechte Reproduzierbarkeit der Messergebnisse. Kürzlich wurde berichtet, dass die Kationenverteilung, also die Anordnung der Fe^{3+}- und Zn^{2+}-Kationen innerhalb des Sauerstoffgitters, die photoelektrochemische Aktivität des Halbleiters beeinflusst. Der Einfluss der Kationenverteilung auf andere physikalisch-chemische Eigenschaften, die in direktem Zusammenhang mit der photoelektrochemischen Aktivität stehen, wird bisher jedoch kaum verstanden. Der zur Charakterisierung der Kationenverteilung verwendete Parameter ist der Inversionsgrad $0 \leq x \leq 1$, der gemäß der Strukturformel $^T[Zn_{1-x}Fe_x]^O[Zn_xFe_{2-x}]O_4$ die Verteilung der Kationen auf die Tetraederlücken T und die Oktaederlücken O des kubisch-flächenzentrierten Sauerstoffgitters kennzeichnet.

Im Rahmen dieser Arbeit wurden hochreine ZFO-Proben mit Inversionsgraden zwischen $x \approx 0{,}07$ und $x \approx 0{,}20$ synthetisiert. Die Proben zeigten innerhalb der experimentellen Bestimmungsgrenzen gleiche Teilchengrößen, Kristallitgrößen und Kristallinität, wie durch XRD-Messungen in Kombination mit einer Rietveld-Verfeinerung, Mössbauer-Spektroskopie, Raman-Spektroskopie, Rasterelektronenmikroskopie und Elementanalyse bestätigt wurde. Sauerstoff-fehlstellen wurden nicht festgestellt. Somit unterscheiden sich die verschiedenen ZFO-Proben ausschließlich im Inversionsgrad als einzige unabhängige Variable. Die Lichtabsorption, der Ladungsträgertransport und die elektronischen Eigenschaften wurden mittels UV-Vis-NIR-Reflektionsmessungen, Impedanzspektroskopie sowie

zeitgemittelter und transienter Photolumineszenzspektroskopie untersucht. Um die photoelektrochemische Aktivität der ZFO-Proben mit unterschiedlichen Inversionsgraden zu vergleichen, wurde die Effizienz der Methanoloxidation unter Bestrahlung mit simuliertem Sonnenlicht bestimmt.

Es wurde gefunden, dass die Kationenverteilung die Bandlückenenergie des Materials nicht beeinflusst, jedoch einen großen Einfluss auf den Ladungsträgertransport und die elektronischen Eigenschaften des ZFO hat. Die photoelektrochemische Aktivität nahm mit zunehmendem Inversionsgrad zu. Dieser Einfluss wurde hauptsächlich auf den verbesserten Ladungstransport in Proben mit höherem Inversionsgrad zurückgeführt. Außerdem wurde festgestellt, dass Änderungen der Übergangswahrscheinlichkeit der lichtinduzierten elektronischen Übergänge von ZFO, die mit dem Erhöhen des Inversionsgrades einhergehen, in geringerem Maße zusätzlich zur beobachteten Steigerung der photoelektro-chemischen Aktivität beitragen.

Diese Arbeit liefert einen grundlegenden Einblick in den Einfluss des Inversionsgrades auf die photoelektrochemische Aktivität von ZFO. Darüber hinaus tragen die hier präsentierten Ergebnisse zum Verständnis einiger Faktoren bei, die den Wirkungsgrad von ZFO-Photoanoden herabsetzen.

Schlagworte: Spinell $ZnFe_2O_4$, Inversionsgrad, Kationenverteilung, Photoelektrochemie, Photoanode.

Abstract

Spinel $ZnFe_2O_4$ (ZFO) is a widely studied iron-based semiconductor for application as photoanode material in photoelectrochemical water splitting tandem cells. However, the current benchmark efficiency reported for photoelectrochemical water oxidation at ZFO photoanodes is approximately one order of magnitude smaller than the predicted theoretical maximum. In addition, a large dispersion between the efficiencies reported for ZFO photoanodes prepared by different synthetic approaches, as well as poor reproducibility, become obvious from published data. It has been recently reported that the cation distribution, *i.e.*, the ordering of the Fe^{3+} and Zn^{2+} cations within the oxygen lattice, has an impact on the photoelectrochemical activity of the semiconductor. However, the impact of the cation distribution on physicochemical properties directly related to the photoelectrochemical activity was poorly understood. The parameter employed to characterize the cation distribution is the degree of inversion, *x*, defined as $^T[Zn_{1-x}Fe_x]^O[Zn_xFe_{2-x}]O_4$, with $0 \leq x \leq 1$ (the superscripts T and O denote tetrahedral and octahedral sites, respectively).

In this work, highly pure ZFO samples exhibiting degrees of inversion ranging from $x \approx 0.07$ to $x \approx 0.20$ were synthesized. The samples exhibited, within the limit of the experimental determination, equal particle size, crystallite size, and crystallinity, as was confirmed by XRD plus Rietveld refinement, Mössbauer spectroscopy, Raman spectroscopy, scanning electron microscopy, and elemental analysis. Oxygen vacancies were not detected. Therefore, the degree of inversion is assumed to be the only independent variable between the different samples. The light absorption, charge carrier transport, and electronic properties were investigated by UV-Vis-NIR reflectivity, impedance spectroscopy, and time-averaged as well as transient photoluminescence spectroscopy, respectively. The photoelectrochemical efficiency for the methanol oxidation reaction under simulated solar irradiation was determined in order to compare the activity of the ZFO samples having different degrees of inversion.

It was found that the cation distribution does not affect the band gap energy of ZFO but has a large impact on the charge carrier transport and the electronic properties. An increase in the photoelectrochemical activity was observed by increasing the degree of inversion. This impact was mainly ascribed to the enhanced charge carrier transport properties of the samples having higher degrees of inversion. In addition, changes in the probability of the photoinduced electronic transitions of ZFO produced by increasing the degree of inversion were found to additionally contribute, to a lesser extent, to the observed enhancement in the photoelectrochemical activity.

This thesis provides a fundamental insight concerning the impact of the degree of inversion on the photoelectrochemical activity of ZFO. Furthermore, the results presented herein contribute to the understanding of some factors limiting the efficiency of ZFO photoanodes.

Keywords: Spinel $ZnFe_2O_4$, degree of inversion, cation distribution, photo-electrochemistry, photoanode.

Table of **Contents**

VIII

Chapter 1

Introduction

The depletion of fossil fuels and the increasing global warming are pushing mankind to exploit available sources of clean energy.[1] Therefore, emerging technologies taking advantage of renewable energy sources are gradually replacing technologies which use non-renewable resources.[2] One of the most important and abundant renewable energy reservoirs is the sun. Solar energy might be converted into thermal, electrical, or chemical energy *via* solar heating,[3] photovoltaic,[3] or photoelectrochemical[4,5] devices, respectively. A promising approach to convert solar energy into chemical energy is the photoelectrochemical water splitting tandem cell.[5] In a photoelectrochemical water splitting tandem cell (Fig. 1.1A), both, molecular hydrogen and molecular oxygen are produced by water reduction and oxidation, respectively. The energy necessary to drive this uphill reaction in which the free energy increases by 237 kJ mol^{-1} is provided by the solar irradiation.[6] In addition, light harvesting materials are required to achieve the solar-to-chemical energy conversion. The light harvesting material is usually a semiconductor capable of absorbing photons and generating excited states (Fig. 1.1B).[7] Photophysical and photochemical processes are initiated as the material returns to its original ground state. Several steps are involved in these processes.[8] First, during excitation with photons of energy larger than the band gap energy, electrons are transferred to the conduction band of the material creating vacancies (holes) in the valence band. The photogenerated charge carriers can undergo direct recombination, migrate to the surface, or become trapped at deep or superficial defect states. Deeply trapped species can recombine with trapped or free charge carriers. On the surface of a photoelectrode made of a semiconductor material, free or trapped electrons can initiate reduction while holes can initiate oxidation reactions of species being present in the surrounding electrolyte. Whether the electrons or the holes migrate to the surface depends on the band bending of the material, which can be controlled by the doping level of the semiconductor (Fig. 1.1B). When the

semiconductor contains mostly free electrons (n-type conductivity), the band bending favors the migration of the holes towards the surface of the material. However, when free holes are the majority charge carriers (p-type conductivity), the migration of electrons towards the surface of the material is promoted.[9] Thus, n-type semiconductors are used to prepare photoanodes to drive the water oxidation reaction ($2H_2O \rightarrow O_2 + 4H^+ + 4e^-$, $E° = +1.23$ V vs. RHE) while p-type semiconductors are used to prepared photocathodes to drive the water reduction reaction ($4H_2O + 4e^- \rightarrow 2H_2 + 4OH^-$, $E° = 0$ V vs. RHE).
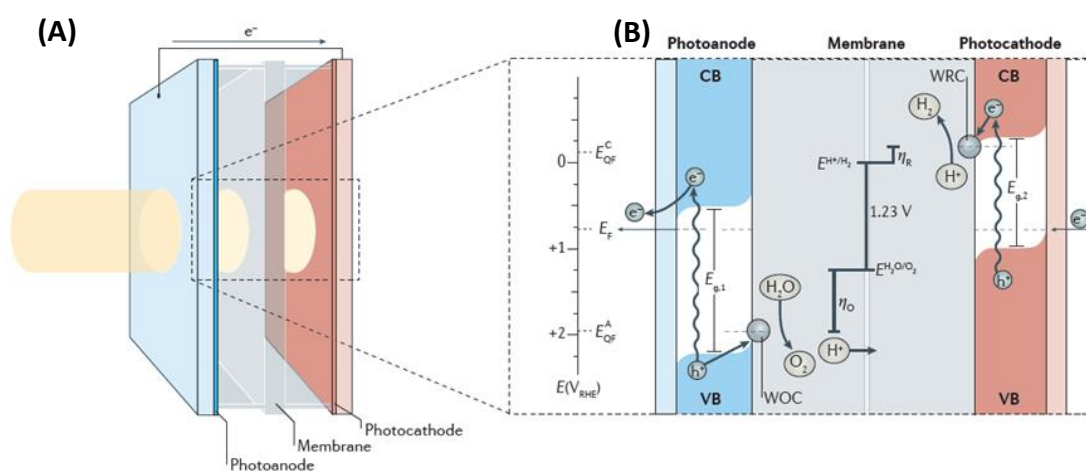
Fig. 1.1. **(A)** Scheme of a photoelectrochemical water splitting tandem cell. The solar light is transferred towards the anodic chamber. **(B)** Working principle of the photoelectrochemical water splitting tandem cell. After light excitation with energy larger than the band gap energy, electron-hole pairs are generated in both, the photoanode and the photocathode. Favored by the band bending, the photogenerated holes in the photoanode migrate towards the surface and oxidize water at a water oxidation catalyst (WOC). Likewise, the photogenerated electrons in the photocathode migrate towards the surface and reduce water at a water reduction catalyst (WRC). The electronic circuit is closed when the photogenerated electrons in the photoanode migrate through the external wire to recombine with the photogenerated holes in the photocathode. Reproduced with permission from Ref. 10.

The first report of the electrochemical photolysis of water at a semiconductor electrode was published by Fujishima, Honda, and Kikuchi in 1969.[11–13] The authors constructed a photoelectrochemical cell in which a titanium dioxide (TiO_2) electrode was connected with a platinum black counter electrode. By

irradiating with light having wavelengths shorter than 415 nm, molecular oxygen evolution was observed from the surface of TiO_2 and molecular hydrogen was evolved from the platinum counter electrode at a much lower bias voltage as compared to normal electrolysis. This pioneering research was the starting point for a rapid development of the fields of semiconductor photocatalysis and photoelectrochemistry. During the following decades, TiO_2 was the most widely studied semiconductor for solar energy conversion applications due to its high efficiency, high chemical stability, relatively low cost, abundance, and low toxicity.[8,9] However, as a consequence of its large band gap ($\approx$ 3.2 eV for the anatase polymorph), UVA irradiation, which accounts for less than 4 % of the total solar irradiation on the sea level, is required for the excitation.[14,15] Although several strategies such as non-metal doping, metal deposition, dye sensitization, or defect induction were developed in order to enhance the visible light efficiency of TiO_2,[16,17] other materials became more attractive for application-oriented research.

Highly efficient photoelectrochemical water splitting tandem cells have to be developed with semiconductors having the same advantages of TiO_2 (high efficiency, high chemical stability, relatively low cost, abundance, and low toxicity) but without the limitation of the low visible light activity. Although the ideal material meeting all these requirements has not been hitherto synthesized, several metal oxide semiconductors other than TiO_2 are potential candidates for solar assisted water oxidation or reduction.[18] Hematite (α-Fe_2O_3), the most thermodynamically stable form of iron oxide under ambient conditions, has been widely investigated as an n-type semiconductor for photoelectrochemical water oxidation.[19] The first report on an α-Fe_2O_3 photoanode was made by Hardee and Bard in 1976.[20] The authors reported the photoelectrochemical oxidation of water under visible light irradiation and showed that approximately 20 % of the total photocurrent is obtained at irradiation wavelengths ranging from 400 to 550 nm. α-Fe_2O_3 is prepared from abundant materials (iron is the fourth most common element in the earth's crust), it has a high stability, is relatively inexpensive, and

non-toxic.[21] In addition, a band gap value of $\approx$ 2.2 eV allows α-Fe_2O_3 to harvest visible light photons of wavelengths shorter than 550 nm. For α-Fe_2O_3 photoanodes, the maximum theoretical photocurrent for the photoelectrochemical water oxidation reaction under simulated solar irradiation (1000 W m^{-2}, AM1.5G filter) is approximately 12.6 mA cm^{-2}.[21] However, the current photocurrent benchmark reported for the water oxidation with an α-Fe_2O_3 photoanode is approximately 4.32 mA cm^{-2}, *i.e.*, 34 % of the maximum theoretical value.[22] More than 40 years after the findings of Hardee and Bard, the extensive research carried out by the photoelectrochemical scientific community provided an insight into the reasons limiting the activity of α-Fe_2O_3.[21] Thus, it is currently well-known that the large difference between the benchmark and the maximum theoretical photocurrent is mainly due to two intrinsic aspects of α-Fe_2O_3. One is the low electrical conductivity, which has been considered as a bottleneck in improving the efficiency of the photoelectrochemical water oxidation reaction.[23] Due to the low electrical conductivity, majority charge carriers are not efficiently transported to the electrode surface and, thus, high conversion efficiencies are not attained. The second drawback of α-Fe_2O_3 is the short charge carriers lifetime.[21] It is well-known that the charge carriers lifetime of α-Fe_2O_3 is limited by the extremely efficient nonradiative relaxation processes attributed to the high density of trap states.[24] It was reported for α-Fe_2O_3 thin films that photogenerated electrons recombine with holes or are trapped approximately 3 ps after their formation.[25] Although several strategies like morphology control, nanostructuring, and doping are known to partially overcome these limitations,[21,24] the ultrafast relaxation of the photogenerated electrons suggest that photocurrents close to the theoretical maximum will be difficult, if not impossible, to achieve.[21,24] Therefore, the research focus has been shifted to mixed iron oxides with the aim to develop new photoelectrochemically active semiconductors having the advantageous features of α-Fe_2O_3 but without its main limitations.[26] In this regard, ferrites have captured the attention of the scientific community due to promising results in the field of photoelectrochemistry.[27,28]

Ferrites with the empirical formula MFe_2O_4 (where M is a bivalent metal ion) normally crystallize in the spinel structure.[29] The spinel structure consists of O^{2-} anions arranged in a face-centered cubic structure. In the so-called normal spinel structure, the M^{2+} cations occupy tetrahedral sites and the Fe^{3+} cations occupy octahedral sites within the oxygen lattice ($^T[M]^O[Fe_2]O_4$, where the superscripts T and O denote the tetrahedral and octahedral sites, respectively). When all the M^{2+} cations in the normal structure are interchanged by Fe^{3+} cations, the ferrite adopts the so-called inverse spinel structure ($^T[Fe]^O[MFe]O_4$). Structural configurations in between normal and inverse are also possible and the degree of inversion, x, is the parameter employed to characterize them according to $^T[M_{1-x}Fe_x]^O[M_xFe_{2-x}]O_4$, with $0 \leq x \leq 1$. Thus, values of $x = 0$ and $x = 1$ describe the normal and inverse spinel structure, respectively. As well as most of the metal oxide semiconductors, spinel ferrites normally exhibit an n-type conductivity attributed to oxygen vacancies induced during the synthesis of the materials.[30,31] However, the synthesis of $CoFe_2O_4$, $NiFe_2O_4$, and $CuFe_2O_4$ exhibiting a p-type conductivity has been reported.[28] Therefore, spinel ferrites are used for both, photoelectrochemical water oxidation and water reduction.[27]

Spinel ferrites are synthesized by cost-effective techniques from earth-abundant materials and have a high chemical stability under water oxidation conditions.[28] Furthermore, it is well-known that the degree of inversion of spinel ferrites closely depends on the synthetic conditions.[32] Within spinel ferrites, $ZnFe_2O_4$ (ZFO) has been extensively studied for application in photoelectrochemical processes.[33] ZFO has many of the advantageous characteristics of α-Fe_2O_3 such as a relatively narrow band gap (1.9 – 2.3 eV) and an exceptional photostability in basic media.[33] At standard conditions (273.15 K and 100 kPa), the normal spinel structure ($^T[Zn]^O[Fe_2]O_4$) is the thermodynamically most stable configuration for bulk ZFO (Fig. 1.2A).[34] However, the preparation of bulk ZFO samples with cation distributions (Fig. 1.2B) ranging from $x \approx 0.02$ to $x \approx 0.20$ has been described in the literature.[34] Higher degrees of inversion up to $x = 0.94$ have been reported for nanoparticulate

ZFO.[35] Therefore, ZFO nanoparticles having different cation distributions are prepared by different synthetic routes. Akhtar *et al.*[36] reported that ZFO nanoparticles with a degree of inversion $x = 0.25$ or $x = 0.50$ are obtained by a sol-gel technique using citric acid or urea, respectively, as the complexing agent. ZFO thin films with a degree of inversion $x = 0.6$ were prepared by Nakashima *et al.*[37] *via* a radio-frequency sputtering method. Furthermore, Kamiyama *et al.*[38] showed that the cation distribution of ZFO normally increases as the particle size decreases.
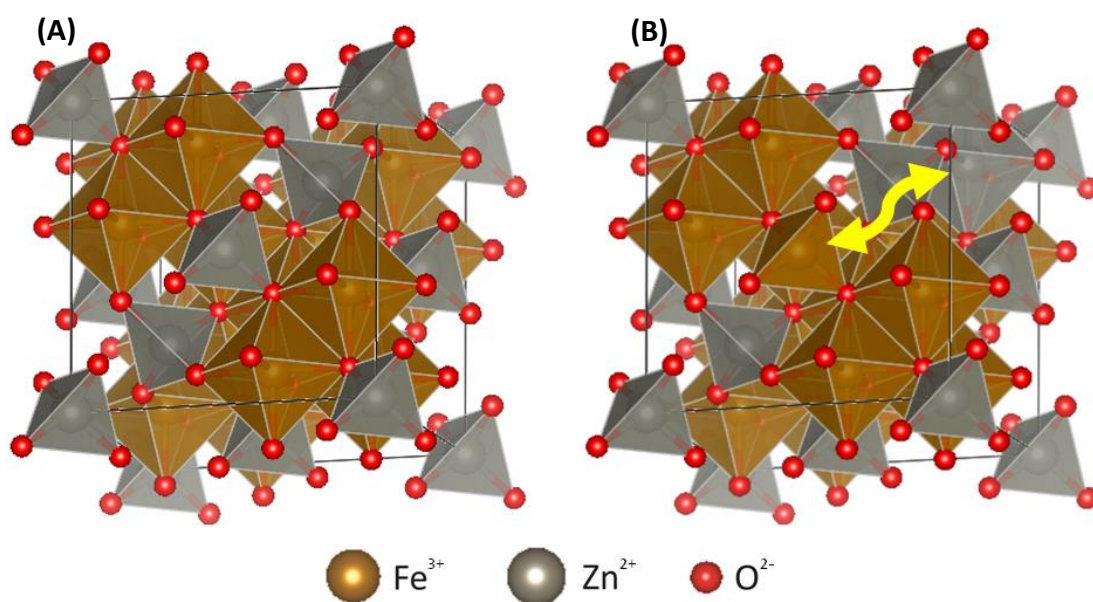

Fig. 1.2. **(A)** Crystallographic 3D structure of ZFO with a normal spinel arrangement ($x = 0$). All the Zn^{2+} cations (grey spheres) are placed in tetrahedral sites while all the Fe^{3+} cations (brown spheres) are located in octahedral sites within the O^{2-} (red spheres) lattice. **(B)** Crystallographic 3D structure of ZFO having a degree of inversion of $x = 0.125$. One Fe^{3+} cation is located in a tetrahedral site due to the inversion with a Zn^{2+} cation now located in an octahedral site. These two cations are indicated with a yellow arrow. The 3D structures were created with VESTA 3 visualization system.[39]

Results of several scientific investigations of ZFO photoanodes for the water oxidation reaction have been reported during the last four years.[33] Fig. 1.3 shows some of the most relevant results presented during this period of time. The current densities for the photoelectrochemical water oxidation reaction with an applied external bias of 1.23 V vs. RHE under simulated solar irradiation are inferior to those

of α-Fe_2O_3 and one order of magnitude smaller than the predicted maximum theoretical value (11 mA cm^{-2}). Furthermore, a large dispersion between the current densities reported for ZFO samples prepared by different techniques is observed from Fig. 1.3. Kim et al.[40] (spot (a) in Fig. 1.3) reported a current density of 0.24 mA cm^{-2} for a photoanode consisting of ZFO nanorods loaded with a cobalt phosphate (Co-Pi) water oxidation catalyst. A microwave annealing process was applied to the sample in order to improve both the crystallinity and the surface quality. In a later report, Kim et al.[41] (spot (b) in Fig. 1.3) showed that the photocurrent of a ZFO nanorod photoanode increases up to 0.32 mA cm^{-2} as oxygen vacancies are induced by heat treatment in an H_2 atmosphere. A current density of 0.35 mA cm^{-2} was reported by Hufnagel et al.[42] (spot (c) in Fig. 1.3) for a ZFO photoanode prepared by atomic layer deposition on an inverse opal structured substrate. Peeters et al.[43] (spot (d) in Fig. 1.3) reported a low current density of approximately 0.05 mA cm^{-2} for a dense ZFO photoanode prepared via a conventional chemical vapor deposition approach. A current density of 0.20 mA cm^{-2} was reported by Guijarro et al.[44] (spot (e) in Fig. 1.3) for a ZFO photoanode prepared following a procedure similar to that reported by Kim et al. The current density of the ZFO nanorod photoanode prepared by Kim et al. was further improved up to 0.92 mA cm^{-2} (spot (f) in Fig. 1.3) by the same research group using a NiFeO$_x$ water oxidation catalyst and incorporating a TiO$_2$ underlayer to block the electron back injection and to provide Ti^{4+} for doping of the ZFO.[45] Finally, Zhu et al.[46] (upper spot (g) in Fig. 1.3) recently established the benchmark photocurrent of 1.0 mA cm^{-2} using a nanorod-array ZFO photoanode annealed in an H_2 atmosphere and loaded with a NiFeO$_x$ water oxidation catalyst. The authors controlled the crystallinity and the degree of inversion of the samples by performing the synthesis at temperatures ranging from 773 to 1073 K. Interestingly, they reported that ZFO samples with a poor crystallinity and a high degree of inversion ($x \approx 0.19$, upper spot (g) in Fig. 1.3) exhibit a higher efficiency for the photoelectrochemical water oxidation than samples with higher crystallinity and lower degree of inversion ($x \approx 0.13$, lower spot (g) in Fig. 1.3). An exception to this behavior was reported for the sample with the

lowest crystallinity and the highest degree of inversion ($x \approx 0.30$, middle spot (g) in Fig. 1.3), which was prepared at the lowest temperature (773 K). The authors ascribed the observed results to a high concentration of surface defects in this sample, which mask the effect of the degree of inversion. It was suggested that the surface defects were repaired for the samples calcined at higher temperatures (883 to 1073 K).
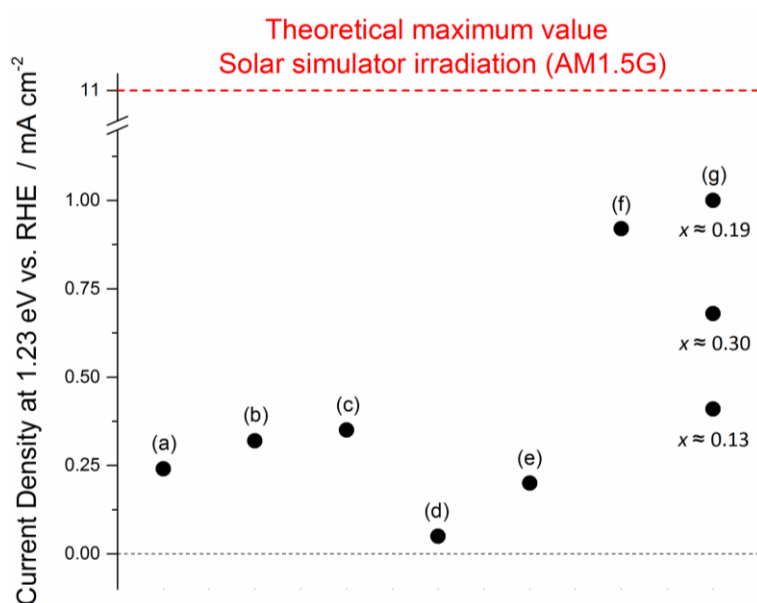
Fig. 1.3. Current densities reported in the literature during the past four years for the water oxidation reaction on ZFO photoanodes. The current densities were measured with an applied external bias of 1.23 V vs. RHE under simulated solar irradiation (1000 W m^{-2}). The red dashed line indicates the maximum theoretical photocurrent of about 11 mA cm^{-2} predicted for ZFO. The spots (a) to (g) correspond to Ref. 40 to 46, respectively. The different spots in (g) correspond to current densities for ZFO photoanodes with different degree of inversion.

As well as for α-Fe$_2$O$_3$, morphology control, nanostructuring, and doping are helpful approaches to enhance the photoelectrochemical activity of ZFO. By applying these strategies, the current densities of pristine ZFO are increased by a factor of ≈ 37.[45] However, as was shown by Zhu *et al.*[46], the degree of inversion has also a large impact on the photoelectrochemical activity of ZFO. As was mentioned above, the cation distribution of nanoparticulate ZFO closely depends on the synthetic conditions and values ranging from $x \approx 0$ to $x \approx 1$ are feasible.

Nevertheless, the degree of inversion is generally not reported in the papers analyzing the photoelectrochemical properties of ZFO. In fact, within the literature overview shown in Fig. 1.3, only Zhu *et al.*[46] have analyzed the cation distribution of their ZFO samples. Therefore, the large dispersion between the current densities reported for ZFO prepared by different techniques might be ascribed to the certainly different degrees of inversion of the samples. In order to understand why the degree of inversion affects the photoelectrochemical activity of ZFO, the correlation between the cation distribution and the physicochemical properties must be assessed.

The impact of the degree of inversion on the magnetism of ZFO is well-known[47,48] because the material is widely used in the electronics industry and, therefore, its magnetic properties play a fundamental role.[49] However, the magnetic properties do not significantly affect the photoelectrochemical activity of semiconductors.[24] A photoelectrochemical process depends on the synergetic interaction of six major processes, *i.e.*, the photon absorption, the exciton separation, the charge carrier diffusion, the charge carrier transport, the catalytic efficiency, and the mass transfer of reactants and products.[7] Scientific reports concerning the effect of the cation distribution of ZFO on these processes are scarce or non-existent.

The aim of this thesis was the study of the impact of the degree of inversion on the photon absorption, the exciton separation, and the charge carrier transport of ZFO. The final objective was to elucidate the reasons explaining the reported large impact of the cation distribution on the photoelectrochemical activity of ZFO. For this purpose, ZFO photoanodes having different cation distributions were prepared. The samples were extensively characterized by means of XRD plus Rietveld refinement, Mössbauer spectroscopy, Raman spectroscopy, scanning electron microscopy, and elemental analysis. A systematic study of the effect of the degree of inversion on the optical, dielectric, and electronic properties of ZFO, as

well as their correlation to the photoelectrochemical activity, is presented in this work.

The topics of this thesis are discussed in detail in four additional chapters comprising three peer-reviewed published articles. Chapter 2 includes the article entitled *Effect of the Degree of Inversion on Optical Properties of Spinel ZnFe$_2$O$_4$*,[50] in which the effects of the cation distribution on the Raman scattering and the UV-Vis-NIR reflectivity of ZFO are analyzed. Chapter 3 comprises the manuscript entitled *Effect of the Degree of Inversion on the Electrical Conductivity of Spinel ZnFe$_2$O$_4$*.[51] In this manuscript, the impact of the cation distribution on the charge carrier transport properties of ZFO are investigated. Chapter 4 includes the article entitled *Effect of the Degree of Inversion on the Photoelectrochemical Activity of Spinel ZnFe$_2$O$_4$*,[52] in which both, the electronic properties and the photoelectrochemical activity of ZFO are analyzed as a function of the cation distribution. Finally, Chapter 5 comprises a concluding discussion where the results presented in the previous chapters are summarized and correlated.

References

(1)   Panwar, N. L.; Kaushik, S. C.; Kothari, S. Role of Renewable Energy Sources in Environmental Protection: A Review. *Renew. Sustain. Energy Rev.* **2011**, *15*, 1513–1524.

(2)   Dincer, I. Renewable Energy and Sustainable Development: A Crucial Review. *Renew. Sustain. Energy Rev.* **2000**, *4*, 157–175.

(3)   Jamar, A.; Majid, Z. A. A.; Azmi, W. H.; Norhafana, M.; Razak, A. A. A Review of Water Heating System for Solar Energy Applications. *Int. Commun. Heat Mass Transf.* **2016**, *76*, 178–187.

(4)   Nozik, A. J. Photoelectrochemistry: Applications to Solar Energy Conversion. *Ann. Rev. Phys. Chem.* **1978**, *29*, 189–222.

(5)   Abe, R. Recent Progress on Photocatalytic and Photoelectrochemical Water Splitting under Visible Light Irradiation. *J. Photochem. Photobiol. C Photochem. Rev.* **2010**, *11*, 179–209.

(6)   Hisatomi, T.; Kubota, J.; Domen, K. Recent Advances in Semiconductors for Photocatalytic and Photoelectrochemical Water Splitting. *Chem. Soc. Rev.* **2014**, *43*, 7520–7535.

(7)   Takanabe, K. Photocatalytic Water Splitting: Quantitative Approaches toward Photocatalyst by Design. *ACS Catal.* **2017**, *7*, 8006–8022.

(8)   Hoffmann, M. R.; Martin, S. T.; Choi, W.; Bahnemann, D. W. Environmental Applications of Semiconductor Photocatalysis. *Chem. Rev.* **1995**, *95*, 69–96.

(9)   Schneider, J.; Matsuoka, M.; Takeuchi, M.; Zhang, J.; Horiuchi, Y.; Anpo, M.; Bahnemann, D. W. Understanding TiO_2 Photocatalysis: Mechanisms and Materials. *Chem. Rev.* **2014**, *114*, 9919–9986.

(10)   Sivula, K.; van de Krol, R. Semiconducting Materials for Photoelectrochemical Energy Conversion. *Nat. Rev. Mater.* **2016**, *1*, 15010.

(11)   Fujishima, A.; Honda, K.; Kikuchi, K. Photosensitized Electrolytic Oxidation on Semiconducting n-Type TiO_2 Electrode. *Kogyo Kagaku Zasshi* **1969**, *72*, 108–113.

(12)   Fujishima, A.; Honda, K. Electrochemical Photolysis of Water at a Semiconductor Electrode. *Nature* **1972**, *238*, 37–38.

(13)   Hashimoto, K.; Irie, H.; Fujishima, A. TiO_2 Photocatalysis: A Historical Overview and Future Prospects. *Jpn. J. Appl. Phys.* **2005**, *44*, 8269–8285.

(14)   Gueymard, C. A. Parameterized Transmittance Model for Direct Beam and Circumsolar Spectral Irradiance. *Sol. Energy* **2001**, *71*, 325–346.

(15)   Gueymard, C. A. The Sun's Total and Spectral Irradiance for Solar Energy Applications and Solar Radiation Models. *Sol. Energy* **2004**, *76*, 423–453.

(16)   Kumar, S. G.; Devi, L. G. Review on Modified TiO_2 Photocatalysis under UV/Visible Light: Selected Results and Related Mechanisms on Interfacial Charge Carrier Transfer Dynamics. *J. Phys. Chem. A* **2011**, *115*, 13211–13241.

(17)   Pelaez, M.; Nolan, N. T.; Pillai, S. C.; Seery, M. K.; Falaras, P.; Kontos, A. G.; Dunlop, P. S. M.; Hamilton, J. W. J.; Byrne, J. A.; Shea, K. O.; et al. A Review on the Visible Light Active Titanium Dioxide Photocatalysts for Environmental Applications. *Appl. Catal. B Environ.* **2012**, *125*, 331–349.

(18)   Roger, I.; Shipman, M. A.; Symes, M. D. Earth-Abundant Catalysts for Electrochemical and Photoelectrochemical Water Splitting. *Nat. Rev. Chem.* **2017**, *1*, 0003.

(19)   Tamirat, A. G.; Rick, J.; Dubale, A. A.; Su, W.-N.; Hwang, B.-J. Using Hematite for Photoelectrochemical Water Splitting: A Review of Current Progress and Challenges. *Nanoscale Horizons* **2016**, *1*, 243–267.

(20)   Hardee, K. L.; Bard, A. J. Semiconductor Electrodes. V. The Application of Chemically Vapor Deposited Iron Oxide Films to Photosensitized Electrolysis. *J. Electrochem. Soc.* **1976**, *123*, 1024–1026.

(21)   Sivula, K.; Le Formal, F.; Grätzel, M. Solar Water Splitting: Progress Using Hematite (α-Fe_2O_3) Photoelectrodes. *ChemSusChem* **2011**, *4*, 432–449.

(22)   Kim, J. Y.; Magesh, G.; Youn, D. H.; Jang, J.-W.; Kubota, J.; Domen, K.; Lee, J. S. Single-Crystalline, Wormlike Hematite Photoanodes for Efficient Solar Water Splitting. *Sci. Rep.* **2013**, *3*, 2681.

(23)   Li, S.; Cai, J.; Liu, Y.; Gao, M.; Cao, F.; Qin, G. Tuning Orientation of Doped Hematite Photoanodes for Enhanced Photoelectrochemical Water Oxidation. *Sol. Energy Mater. Sol. Cells* **2018**, 179, 328-333.

(24)   Cherepy, N. J.; Liston, D. B.; Lovejoy, J. A.; Deng, H.; Zhang, J. Z. Ultrafast Studies of Photoexcited Electron Dynamics in γ- and α-Fe_2O_3 Semiconductor Nanoparticles. *J. Phys. Chem. B* **1998**, *102*, 770–776.

(25) Joly, A. G.; Williams, J. R.; Chambers, S. A.; Xiong, G.; Hess, W. P.; Laman, D. M. Carrier Dynamics in α-Fe_2O_3 (0001) Thin Films and Single Crystals Probed by Femtosecond Transient Absorption and Reflectivity. *J. Appl. Phys.* **2006**, *99*, 053521.

(26) Alsalka, Y.; Granone, L. I.; Ramadan, W.; Hakki, A. Iron-Based Photocatalytic and Photoelectrocatalytic Nano-Structures : Facts, Perspectives, and Expectations. *Appl. Catal. B Environ.* **2019**, 244, 1065-1095.

(27) Dillert, R.; Taffa, D. H.; Wark, M.; Bredow, T.; Bahnemann, D. W. Research Update: Photoelectrochemical Water Splitting and Photocatalytic Hydrogen Production Using Ferrites (MFe_2O_4) under Visible Light Irradiation. *APL Mater.* **2015**, *3*, 104001.

(28) Taffa, D. H.; Dillert, R.; Ulpe, A. C.; Bauerfeind, K. C. L.; Bredow, T.; Bahnemann, D. W.; Wark, M. Photoelectrochemical and Theoretical Investigations of Spinel Type Ferrites ($M_xFe_{3-x}O_4$) for Water Splitting: A Mini-Review. *J. Photonics Energy* **2016**, *7*, 012009.

(29) Sickafus, K. E.; Wills, J. M.; Grimes, N. W. Structure of Spinel. *J. Am. Ceram. Soc.* **1999**, *82*, 3279–3292.

(30) Nunome, T.; Irie, H.; Sakamoto, N.; Sakurai, O.; Shinozaki, K.; Suzuki, H.; Wakiya, N. Magnetic and Photocatalytic Properties of n- and p-Type $ZnFe_2O_4$ Particles Synthesized Using Ultrasonic Spray Pyrolysis. *J. Ceram. Soc. Japan* **2013**, *121*, 26–30.

(31) Šutka, A.; Pärna, R.; Kleperis, J.; Käämbre, T.; Pavlovska, I.; Korsaks, V.; Malnieks, K.; Grinberga, L.; Kisand, V. Photocatalytic Activity of Non-Stoichiometric $ZnFe_2O_4$ under Visible Light Irradiation. *Phys. Scr.* **2014**, *89*, 044011.

(32) Siddique, M.; Butt, N. M. Effect of Particle Size on Degree of Inversion in Ferrites Investigated by Mössbauer Spectroscopy. *Phys. B Condens. Matter* **2010**, *405*, 4211–4215.

(33) Lee, D. K.; Lee, D.; Lumley, M. A.; Choi, K.-S. Progress on Ternary Oxide-Based Photoanodes for Use in Photoelectrochemical Cells for Solar Water Splitting. *Chem. Soc. Rev.* **2019**, 48, 2126-2157.

(34) O'Neill, H. S. C. Temperature Dependence of the Cation Distribution in Zinc Ferrite ($ZnFe_2O_4$) from Powder XRD Structural Refinements. *Eur. J. Miner.*

1992, *4*, 571–580.

(35) Šepelák, V.; Tkáčová, K.; Boldyrev, V. V.; Wigmann, S.; Becker, K. D. Mechanically Induced Cation Redistribution in $ZnFe_2O_4$ and Its Thermal Stability. *Phys. B* **1997**, *234–236*, 617–619.

(36) Akhtar, M. J.; Nadeem, M.; Javaid, S.; Atif, M. Cation Distribution in Nanocrystalline $ZnFe_2O_4$ Investigated Using X-Ray Absorption Fine Structure Spectroscopy. *J. Phys. Condens. Matter* **2009**, *21*, 405303.

(37) Nakashima, S.; Fujita, K.; Tanaka, K.; Hirao, K.; Yamamoto, T.; Tanaka, I. First-Principles XANES Simulations of Spinel Zinc Ferrite with a Disordered Cation Distribution. *Phys. Rev. B* **2007**, *75*, 174443.

(38) Kamiyama, T.; Haneda, K.; Sato, T.; Ikeda, S.; Asano, H. Cation Distribution in $ZnFe_2O_4$ Fine Particles Studied by Neutron Powder Diffraction. *Solid State Commun.* **1992**, *81*, 563–566.

(39) Momma, K.; Izumi, F. VESTA 3 for Three-Dimensional Visualization of Crystal, Volumetric and Morphology Data. *J. Appl. Crystallogr.* **2011**, *44*, 1272–1276.

(40) Kim, J. H.; Kim, J. H.; Jang, J. W.; Kim, J. Y.; Choi, S. H.; Magesh, G.; Lee, J.; Lee, J. S. Awakening Solar Water-Splitting Activity of $ZnFe_2O_4$ Nanorods by Hybrid Microwave Annealing. *Adv. Energy Mater.* **2015**, *5*, 1401933.

(41) Kim, J. H.; Jang, Y. J.; Kim, J. H.; Jang, J. W.; Choi, S. H.; Lee, J. S. Defective $ZnFe_2O_4$ Nanorods with Oxygen Vacancy for Photoelectrochemical Water Splitting. *Nanoscale* **2015**, *7*, 19144–19151.

(42) Hufnagel, A. G.; Peters, K.; Müller, A.; Scheu, C.; Fattakhova-Rohlfing, D.; Bein, T. Zinc Ferrite Photoanode Nanomorphologies with Favorable Kinetics for Water-Splitting. *Adv. Funct. Mater.* **2016**, *26*, 4435–4443.

(43) Peeters, D.; Taffa, D. H.; Kerrigan, M. M.; Ney, A.; Jöns, N.; Rogalla, D.; Cwik, S.; Becker, H. W.; Grafen, M.; Ostendorf, A.; et al. Photoactive Zinc Ferrites Fabricated via Conventional CVD Approach. *ACS Sustain. Chem. Eng.* **2017**, *5*, 2917–2926.

(44) Guijarro, N.; Bornoz, P.; Prévot, M. S.; Yu, X.; Zhu, X.; Johnson, M.; Jeanbourquin, X. A.; Le Formal, F.; Sivula, K. Evaluating Spinel Ferrites MFe_2O_4 (M = Cu, Mg, Zn) as Photoanodes for Solar Water Oxidation: Prospects and Limitations. *Sustain. Energy Fuels* **2018**, *2*, 103–117.

(45) Kim, J. H.; Jang, Y. J.; Choi, S. H.; Lee, B. J.; Kim, J. H.; Park, Y. Bin; Nam, C. M.;

Kim, H. G.; Lee, J. S. A Multitude of Modifications Strategy of $ZnFe_2O_4$ Nanorod Photoanodes for Enhanced Photoelectrochemical Water Splitting Activity. *J. Mater. Chem. A* **2018**, *6*, 12693–12700.

(46) Zhu, X.; Guijarro, N.; Liu, Y.; Schouwink, P.; Wells, R. A.; Le Formal, F.; Sun, S.; Gao, C.; Sivula, K. Spinel Structural Disorder Influences Solar-Water-Splitting Performance of $ZnFe_2O_4$ Nanorod Photoanodes. *Adv. Mater.* **2018**, *30*, 1801612.

(47) Mozaffari, M.; Eghbali Arani, M.; Amighian, J. The Effect of Cation Distribution on Magnetization of $ZnFe_2O_4$ Nanoparticles. *J. Magn. Magn. Mater.* **2010**, *322*, 3240–3244.

(48) Yuan, Q.; Pan, L.; Liu, R.; Wang, J.; Liao, Z.; Qin, L.; Bi, J.; Gao, D.; Wu, J. Cation Distribution and Magnetism in Quenched $ZnFe_2O_4$. *J. Electron. Mater.* **2018**, *47*, 3608–3614.

(49) Van Groenou, A. B.; Bongers, P. F.; Stuyts, A. L. Magnetism, Microstructure and Crystal Chemistry of Spinel Ferrites. *Mater. Sci. Eng.* **1968**, *3*, 317–392.

(50) Granone, L. I.; Ulpe, A. C.; Robben, L.; Klimke, S.; Jahns, M.; Renz, F.; Gesing, T. M. M.; Bredow, T.; Dillert, R.; Bahnemann, D. W. Effect of the Degree of Inversion on Optical Properties of Spinel $ZnFe_2O_4$. *Phys. Chem. Chem. Phys.* **2018**, *20*, 28267–28278.

(51) Granone, L. I.; Dillert, R.; Heitjans, P.; Bahnemann, D. W. Effect of the Degree of Inversion on the Electrical Conductivity of Spinel $ZnFe_2O_4$. *ChemistrySelect* **2019**, 4, 1232-1239.

(52) Granone, L. I.; Nikitin, K. V.; Emeline, A. V.; Dillert, R.; Bahnemann, D. W. Effect of the Degree of Inversion on the Photoelectrochemical Activity of Spinel $ZnFe_2O_4$. *Catalysts* **2019**, 9, 434.

Chapter 2

## Effect of the Degree of Inversion on Optical Properties of Spinel ZnFe₂O₄

2.1 Foreword

This chapter comprises the article *Effect of the Degree of Inversion on Optical Properties of Spinel ZnFe₂O₄* by Luis I. Granone, Anna C. Ulpe, Lars Robben, Stephen Klimke, Moritz Jahns, Franz Renz, Thorsten M. Gesing, Thomas Bredow, Ralf Dillert, and Detlef W. Bahnemann, published in *Physical Chemistry Chemical Physics*, **2018**, 20, 28267-28278. In this article, the synthesis and characterization of ZFO samples with degree of inversion increasing from $x \approx 0.07$ to $x \approx 0.20$ are presented. An experimental and theoretical analysis concerning the effect of the cation distribution on the Raman scattering and on the UV-Vis-NIR reflectivity of ZFO is reported. Prof. Dr. Thomas Bredow and Anna C. Ulpe (Mulliken Center for Theoretical Chemistry, University of Bonn) contributed to this article by performing the *ab initio* calculations. Prof. Dr. Thorsten M. Gesing and Dr. Lars Robben (Institute of Inorganic Chemistry and Crystallography and MAPEX Center for Materials and Processes, University of Bremen) contributed by performing the XRD measurements and providing support for the Rietveld refinements. Finally, Prof. Dr. Franz Renz, Stephen Klimke, and Moritz Jahns (Institute for Inorganic Chemistry, Gottfried Wilhelm Leibniz University Hannover) contributed by performing the Mössbauer measurements. The figures and tables identified through this chapter with the letter "A" are reproduced in Appendix A.

2.2 Abstract

Spinel ferrites ($^T[M_{1-x}Fe_x]^O[M_xFe_{2-x}]O_4$ with $0 \leq x \leq 1$, where M is a bivalent metal ion and the superscripts denote tetrahedral and octahedral sites) are materials commonly used in electronics due to their outstanding magnetic

properties. Thus, the effect of the degree of inversion, *x*, on these properties is well known. However, its effect on other properties of these materials has rarely been investigated in detail. Since ferrites gained much attention during the last decade as visible light active photocatalysts and photoelectrocatalysts, understanding the effect of the degree of inversion on the optical properties became necessary. Among photocatalytically and photoelectrocatalytically active spinel ferrites, zinc ferrite (ZnFe$_2$O$_4$, ZFO) is one of the most widely studied materials. In this work, five ZFO samples with degrees of inversion varying from 0.07 to 0.20 were prepared by a solid-state reaction employing different annealing temperatures and subsequent quenching. Raman and UV-Vis-NIR spectra were measured and analyzed together with theoretical results obtained from *ab initio* calculations. Changes in the UV-Vis-NIR spectra associated with electronic transitions of tetrahedrally and octahedrally coordinated Fe^{3+} ions are distinguished. However, the optical band gap of the material remains unchanged as the degree of inversion varies. Based on the experimental and theoretical results, a new assignment for the Raman active internal modes and the electronic transitions of ZFO is proposed.
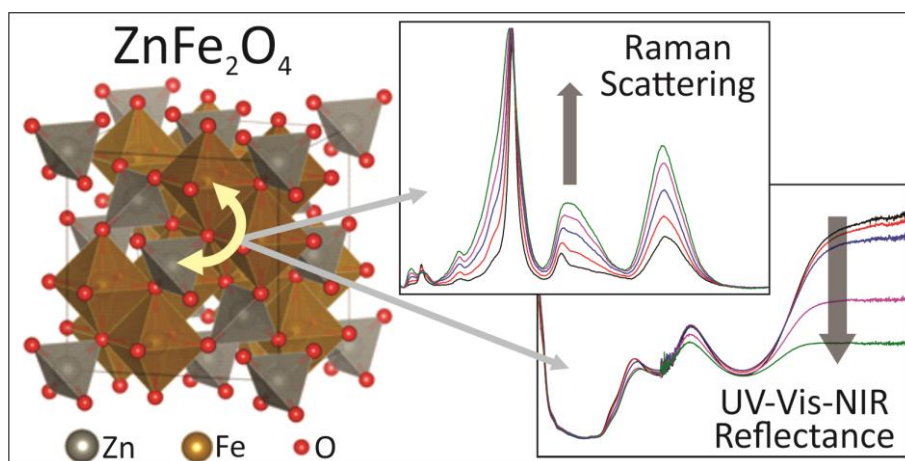
2.3 Introduction

Spinel ferrites are versatile materials with several applications in the fields of information storage,[1] magnetic fluids,[2] microwave devices,[3] and catalysis.[4]

Undoubtedly, their outstanding magnetic properties make spinel ferrites such interesting materials for these purposes.[5] However, other properties, such as semiconductivity, are nowadays scientifically explored. Recently, semiconducting spinel ferrites (MFe$_2$O$_4$, M = metal ion) have attracted the attention in the fields of photocatalysis and photoelectrocatalysis.[6,7] Applications of spinel ferrites in these research areas include artificial photosynthesis,[7] carbon dioxide conversion,[8] hydrogen and oxygen generation via water splitting,[9–11] and water treatment.[12] Properties such as narrow band gaps ($\approx$ 2 eV), high chemical stability, abundance, and low cost make spinel ferrites promising materials for the applications mentioned above.[6,7]

MFe$_2$O$_4$ crystallizes in a face-centered cubic structure like the mineral spinel (MgAl$_2$O$_4$), after which this class of materials is named. In the so-called normal structure, M^{2+} and Fe^{3+} ions occupy 1/8 of the tetrahedral sites and 1/2 of the octahedral sites available in the O^{2-} lattice, respectively. However, when all the M^{2+} ions at the tetrahedral sites are exchanged by Fe^{3+} ions from the octahedral sites, the material adopts a so-called inverse structure. The parameter commonly employed to characterize the cation disorder is the degree of inversion, x, defined as the fraction of M^{2+} ions occupying octahedral sites, according to ^{T}[M$_{1-x}$Fe$_x$]^O[M$_x$Fe$_{2-x}$]O$_4$.

Among photocatalytically and photoelectrocatalytically active spinel ferrites, zinc ferrite (ZnFe$_2$O$_4$, ZFO) is one of the most widely studied materials.[13,14] At standard conditions (273.15 K and 100 kPa), the normal structure is the thermodynamically most stable configuration for bulk ZFO.[15] Nevertheless, it is known that ZFO does not usually exhibit a normal structure and the degree of inversion closely depends on the synthetic conditions.[15–20] This effect is especially pronounced when nanoparticulate ZFO samples are synthesized. Akhtar et al.[18] reported the sol-gel synthesis of ZFO nanoparticles having degrees of inversion of 0.5 or 0.25 when urea or citric acid, respectively, are used as precursors. Kamiyama et al.[19] reported the co-precipitation synthesis of ZFO nanoparticles with a degree

of inversion of 0.142 and Nakashima et al.[20] prepared nanoparticulate ZFO with a degree of inversion of 0.6 by radio-frequency sputtering. ZFO nanoparticles having a high degree of inversion have been prepared by Kurian and Mathew[21] using a solvothermal technique. They reported a degree of inversion of 0.54.[21] Šepelák et al.[22] investigated the effect of high-energy ball-milling in the cation distribution of nanoscaled ZFO. The authors showed an increase in the degree of inversion from 0 to 0.94, i.e., from normal spinel to almost completely inversed spinel by increasing the milling time.

Mozaffari et al.[23] and Yuan et al.[24] reported that the magnetization of ZFO increases as the degree of inversion becomes larger. Harris et al.[25] reviewed the effect of the degree of inversion of mechanochemically processed ZFO nanoparticles not only on the magnetization but also on the Néel temperature and the nuclear magnetic properties, including hyperfine field distributions, isomer shifts, and quadrupole interactions. ZFO samples prepared by mechanochemical methods show degrees of inversion close to 2/3.[25] As a consequence, a ferrimagnetic behavior is observed at room temperature for the highly disordered ZFO samples. Conversely, an antiferromagnetic behavior with a Néel temperature of 10.5 K is observed for normal ZFO.[25]

Although the effect of the degree of inversion on the magnetic properties is well known, some other physicochemical properties have not been until now investigated in detail. Among these, the optical properties are of utmost importance for the characterization of a material with applications in optoelectronics, photocatalysis, and photoelectrocatalysis. On the one hand, the UV and visible light absorptivity of a material is directly related with the maximum photonic efficiency that can be expected under defined experimental conditions. On the other hand, Raman spectroscopy is a commonly employed technique for the characterization of ZFO. Wang et al.[26] reported a first order Raman spectrum of a ZFO sample having a degree of inversion of 0.10. The authors correlated the observed signals with the five Raman active internal modes predicted by the factor group analysis.[26] The

experimental data presented in the current study demonstrate that some of the signals detected by Wang *et al.* are originated due to a symmetry perturbation because of the cation disordering and, thus, are not active internal modes. Regarding the absorptivity of ZFO, Pailhé et al.[27] reported a diffuse reflectance Vis-NIR spectrum of a sample with a degree of inversion of 0.140. For the interpretation of some of the electronic transitions, the authors considered the splitting of the Fe(3d) orbitals on the basis of the Russell-Saunders coupling.[27] However, they also assigned some transitions on the basis of a simple splitting of the Fe(3d) orbitals (into t_{2g} and e_g orbitals), thus presenting ambiguous results.

To the best of our knowledge, the effect of the degree of inversion on the Raman scattering and UV-Vis-NIR absorptivity of ZFO has not been studied in detail before. For the first time, Raman spectra of normal and inverted ZFO were calculated, obtaining an excellent agreement with the experimental results. The combination of *ab initio* calculations and experimental data allowed to describe how the optical properties of ZFO evolve as the degree of inversion increases from $x \approx 0.07$ to $x \approx 0.20$. Furthermore, fundamental properties such as the assignment of the Raman active internal modes and the electronic transitions were analyzed. The experimental and theoretical evidence presented in this work supports a new interpretation for both, the Raman active internal modes and the electronic transitions of spinel ZFO.

2.4 Materials and Methods

Polycrystalline ZFO samples were synthesized by means of a solid-state reaction. Stoichiometric amounts of ZnO (Sigma Aldrich, ≥ 99.0%) and Fe_2O_3 (Sigma Aldrich, ≥ 99.0%) powders were mixed together using an agate mortar. The mixture was calcined in air at 1073 K with a heating rate of 350 K h^{-1}. After 12 hours, the sample was cooled to room temperature and grinded again in an agate mortar. Aliquots of 0.500 g were pressed into 13 mm diameter pellets applying a pressure of

55 MPa. The pellets were calcined at 1273 K with a heating rate of 150 K h^{-1}. After 2 hours at this temperature, the samples were cooled to 1073 K with a cooling rate of 100 K h^{-1}, then kept at 1073 K for 12 hours, cooled to 773 K at a rate of 100 K h^{-1}, kept at 773 K for 50 hours, and finally quenched in cold water. Some of the pellets (referred from now as ZFO_773) were retained for further characterization. The rest were divided into four sets of samples. The samples were heated up with a rate of 300 K h^{-1} and calcined at 873, 973, 1073, and 1173 K for 25, 20, 12, and 10 hours, respectively. After this period of time, the calcined pellets were immediately quenched in cold water. These samples will be referred as ZFO_873, ZFO_973, ZFO_1073, and ZFO_1173.

Powder X-Ray diffraction data were collected with an StadiMP diffractometer (Stoe & Cie., Darmstadt, Germany) using monochromatized MoKα$_1$ radiation (λ = 70.9300 pm) and a Mythen2 1K detector (Dectris, Baden-Daettwil, Switzerland). Flat samples for transmission measurements were prepared by placing the sample between two thin mylar foils and fixing these with a metal ring providing a 3 mm hole. The diffraction pattern were recorded in transmission geometry in the 2θ range from 2° to 92°, collecting 5977 data points with a step width of 0.015° 2θ and 270 s measurement time per step. Rietveld refinements were carried out using the Bruker DIFFRAC^{plus} TOPAS V4.2 software (Bruker AXS Inc., Madison, Wisconsin, USA). The space group $Fd\bar{3}m$, with the zinc and iron ions placed in tetrahedral and octahedral sites, respectively, was assumed as starting point for the refinement. The scale factors, lattice parameters, oxygen positional parameters, inversion parameters, the three isotropic displacement parameters, and the zero point were optimized during the refinements. The standard instrumental parameters were determined with a LaB₆ standard (SRM 660c, NIST).

Mössbauer measurements were performed in transmission mode using a Miniaturized Mössbauer Spectrometer MIMOS II with the sample perpendicular to the ^{57}Co/Rh source. The samples were placed into a spherical sample holder and the cap was subsequently rotated to align the crystals in the *xy*-plane. All isomer shifts

are given relative to α-Fe at room temperature. The data were fitted by least-squares method using Lorentzian line shapes with the Recoil 1.05 Mössbauer Analysis software.[28]

Raman measurements were made employing a confocal Bruker Senterra micro-Raman spectrometer. Depolarized spectra were collected at ambient conditions in backscattering geometry using an Olympus BX 51 microscope that allows the incident 785 nm, 633 nm, or 532 nm laser beam to be focused on the sample as a spot of about 2 μm in diameter. An integration time of 5 s, 20 co-additions, and a power of 50 mW, 2 mW, and 2 mW for the 785 nm, 633 nm, and 532 nm lasers, respectively, were used. The instrumental precision was within ± 3 cm^{-1}.

Raman spectra were calculated using the CRYSTAL14 program package,[29] employing triple-ζ basis sets. The frequencies were calculated using the range separated functional HSE06,[30] while the intensities were calculated with B3LYP.[31] A well-converged Monkhorst-Pack grid of 8x8x8 was sufficient. The atomic positions of normal and inverse ZFO were optimized using an experimental lattice parameter of a = 844.32 pm.[32]

UV-Vis-NIR spectroscopy was carried out with an Agilent Carry 5000 device equipped with an external DRA-2500 Diffuse Reflectance Accessory. The spectra were collected in the range of 200 nm to 2000 nm with a data acquisition interval of 1 nm, an averaging time of 0.1 s, a scan rate of 600 nm min^{-1}, and a spectral bandwidth of 2 nm. The instrumental precision was within ± 0.5 nm. The optical band gaps were determined by the derivation of absorption spectrum fitting method (DASF).[33]

Optical spectra of normal and inverse ZFO were calculated using the Vienna *ab initio* Simulation Package (VASP)[34] version 5.4.4. A carefully converged quasi-particle GW0[35] algorithm was employed and to gain insight about the optical properties, the Bethe-Salpeter-Equations (BSE)[36] were solved afterwards. For

normal ZFO, an experimental structure[32] was used, while for inverse ZFO, an optimization of atomic positions was performed.

The composition of the samples was determined analytically by means of inductively coupled plasma optical emission spectrometry (ICP-OES) using a Spectroflame and Spectro Arcos from Spectro Analytical Instruments. Fe and Zn were quantified by measuring the optical emission at 259.941 nm and 213.856 nm, respectively, and comparing with the calibration curve prepared using the respective ICP standards (Carl Roth). Prior to the analysis, the samples were dissolved in freshly distilled 16% HCl (Carl Roth) at 473 K using an ultraWAVE microwave digestion system from MLS GmbH.

The structural and morphological properties of the samples were analyzed using a JEOL JSM-6700F scanning electron microscope provided with a lower secondary electron image detector. An acceleration voltage of 2.0 kV and a 25000 times magnification were employed.

2.5 Results and Discussions

ZFO samples with degree of inversion of approximately 0.07, 0.10, 0.13, 0.16, and 0.20 were synthesized by means of a solid-state reaction. An initial calcination at 1273 K was carried out for all the samples in order to ensure the homogeneity of the crystallinity and the crystallite size between them. The degree of inversion was modified by further calcination steps at temperatures ranging from 773 K to 1173 K and subsequent quenching of the samples in cold water. The samples were characterized employing XRD and Rietveld refinement (Fig. A1), Mössbauer spectroscopy (Table A1 and Fig. A2), Raman spectroscopy (Fig. 2.2 and Fig. A5), and elemental analysis. The elemental analysis revealed a Fe to Zn ratio close, within the experimental error, to 2:1 as expected for ZFO. This ratio will also hold in the case that a mixture of equal amounts of Fe$_2$O$_3$ and ZnO is present.

However, XDR (Fig. A1) and Raman (Fig. 2.2) data give no indication of the presence of ZnO or hematite (α-Fe_2O_3). Maghemite (γ-Fe_2O_3), having a spinel structure, might not be distinguished from ZFO in an XRD diffractogram. However, the presence of γ-Fe_2O_3 is excluded based on the Raman (Fig. A6) and Mössbauer data (Fig. A3). The strongest Raman scattering signal of γ-Fe_2O_3, located at 670 cm^{-1}, might not be differentiated from the broad ZFO band at ca. 647 cm^{-1}.[37] However, the next strongest and characteristic band of γ-Fe_2O_3, located at 718 cm^{-1},[37] is not observed in the Raman spectra of ZFO (Fig. A6). A more conclusive evidence of the absence of γ-Fe_2O_3 comes from the Mössbauer data. A sextet is observed in the Mössbauer spectrum of γ-Fe_2O_3 (Fig. A3) due to its room temperature ferrimagnetism.[37] However, only two duplets (due to the Fe^{3+} cations present in tetrahedral and octahedral sites) are observed in the Mössbauer spectra of the ZFO samples (Fig. A2). This is because of the room temperature paramagnetism of the ZFO samples. Therefore, the presence of γ-Fe_2O_3 as secondary phase in the ZFO samples is excluded.

The values deduced from Rietveld refinement and Mössbauer spectroscopy together with the structural parameters and the iron to zinc molar ratios obtained from the elemental analysis of the different quenched ZFO samples are given in Table 2.1. Neither secondary phases nor impurities could be detected from the XRD patterns. Furthermore, none of the samples showed Mössbauer signals attributable to Fe^{2+}. Hence, the absence of Fe^{2+} and, therefore, of oxygen vacancies has been confirmed by Mössbauer spectroscopy.

As becomes obvious from Fig. 2.1A, the degree of inversion increases linearly with the calcination temperature from 0.074 ± 0.011 at 773 K to 0.203 ± 0.017 at 1173 K. A similar behavior was reported by O'Neill[15] using powder XRD structure refinements, and by Pavese et al.[16] from in situ high-temperature neutron powder diffraction data evaluation (Fig. 2.1B). The results from O'Neill show a monotonic increase in the degree of inversion from 0.019 at 773 K to 0.149 at 1073

K, and then a plateau. The author suggested that this plateau results from the re-ordering kinetics at temperatures higher than 1173 K being too fast to allow a quenching of the sample.[16] This effect was not observed by Pavese *et al.* because their measurements were done in situ.[16]

Table 2.1. Refined structural parameters, degree of inversion deduced from Mössbauer spectroscopy, and Fe to Zn molar ratios of the different temperature annealed ZFO samples. n_{Fe}/n_{Zn} is the Fe to Zn molar ratio, *x* is the degree of inversion, *a* is the lattice parameter, x(O) is the oxygen positional parameter on 32e: x,x,x in $Fd\bar{3}m$, L$_{Vol}$(IB) is the average crystallite size, and B$_{Zn}$, B$_{Fe}$, and B$_o$ are the isotropic displacement parameters concerning the Zn^{2+}, Fe^{3+}, and O^{2-} ions, respectively.

Calcination temperature / K	n_{Fe}/n_{Zn}	Degree of inversion x			a / pm	x(O)	L$_{Vol}$(IB)/ nm	B$_{Zn}$ / Å^2	B$_{Fe}$ / Å^2	B$_o$ / Å^2
		Rietveld Refinement (RR)	Mössbauer Spectroscopy (MS)	$\left(\frac{x_{RR}+x_{MS}}{2}\right)$						
773	1.98 ± 0.04	0.073(7)	0.074 ± 0.015	0.074 ± 0.011	844.285(5)	0.26025(13)	306(6)	0.38(1)	0.37(1)	0.39(3)
873	1.98 ± 0.05	0.106(6)	0.102 ± 0.020	0.104 ± 0.013	844.433(5)	0.26001(11)	293(5)	0.48(1)	0.37(1)	0.50(2)
973	1.97 ± 0.04	0.131(6)	0.136 ± 0.010	0.134 ± 0.008	844.374(5)	0.26001(11)	302(5)	0.53(1)	0.52(1)	0.56(2)
1073	1.98 ±0.03	0.161(7)	0.156 ± 0.012	0.159 ± 0.010	844.432(5)	0.25996(12)	327(6)	0.50(1)	0.53(1)	0.53(2)
1173	1.98 ±0.07	0.196(7)	0.210 ± 0.028	0.203 ± 0.017	844.427(5)	0.25954(13)	283(6)	0.34(1)	0.36(1)	0.41(3)

A comprehensible work regarding the thermodynamics of the cation disorder and the dependence of the degree of inversion with the temperature have been done by Callen *et al.*,[38] Navrotsky and Kleppa,[39] O'Neill and Navrotsky,[40,41] and O'Neill.[15] The cation distribution in ZFO can be treated as a dynamic equilibrium according to the following interchange reaction between ions being present in tetrahedral (subscript "T") and octahedral sites (subscript "O"):

$$^T Zn + {}^O Fe \rightleftarrows {}^O Zn + {}^T Fe$$
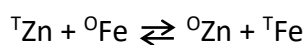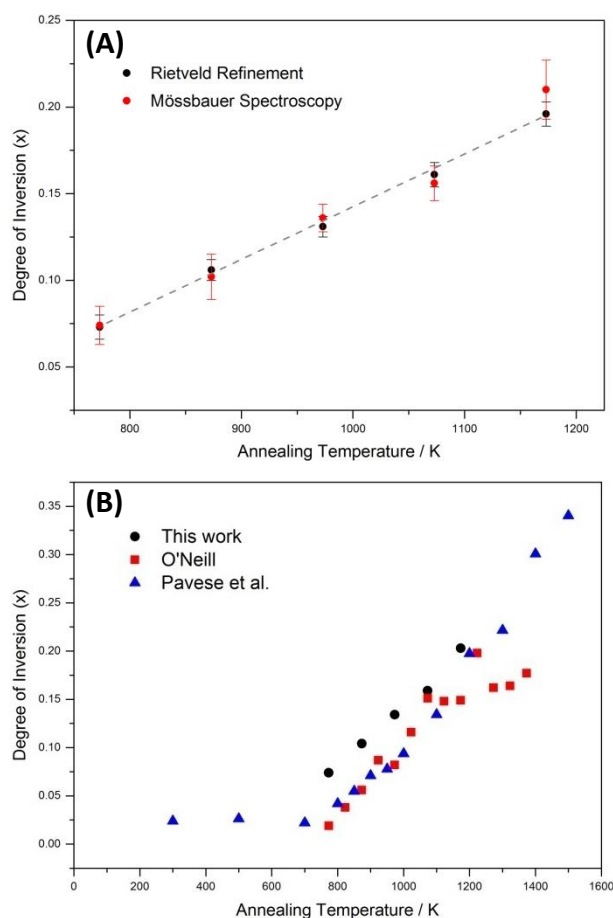
Fig. 2.1. **(A)** Degree of inversion, x, versus the annealing temperature. **(B)** Comparison of the present result with values obtained by O'Neill[15] and Pavese *et al.*[16]

A summary reviewing the thermodynamic analysis of the temperature effect on the degree of inversion is presented in the supporting information (Fig. A4).

The Raman spectra of the different ZFO samples are shown in Fig. 2.2. In agreement with the XRD data, no signals attributed to impurities or secondary phases are identified. The ZFO sample with the lowest degree of inversion (ZFO_773, $x = 0.074 \pm 0.011$) shows five bands at 176.5 ± 3 cm^{-1}, 251 ± 3 cm^{-1} (weak), 352 ± 3 cm^{-1}, 447 ± 3 cm^{-1}, and 647 ± 3 cm^{-1} and one minor signal at 155 ± 3 cm^{-1}. The sharp signal at 352 ± 3 cm^{-1} exhibits a broad shoulder at smaller wavenumbers while the band at 447 ± 3 cm^{-1} presents a broad shoulder at higher wavenumbers. The broad signal at 647 ± 3 cm^{-1} can be deconvoluted into two Gaussian-shape signals at ca. 644 cm^{-1} and 675 cm^{-1} (Fig. A7). Comparing with the

Raman spectra measured with 532 nm and 633 nm laser excitations (Fig. A5), the relative intensities of the bands change markedly. Interestingly, a signal not present in the spectra obtained with 785 nm laser excitation is observed at 573.5 ± 3 cm^{-1} for the samples having a low degree of inversion. This signal decreases rapidly as the degree of inversion of the samples increases. A group-theoretical analysis of the vibrational spectrum for the spinel structure made by White and DeAngelis[42] predicted five Raman active internal modes: A_{1g}, E_g, and three T_{2g}.[42] Because normal and inverse spinel crystallize in the same space group, no change is expected in the number of active internal Raman modes. Nevertheless, when the degree of inversion is neither 0 nor 1 ($0 < x < 1$), the symmetry is perturbed and the number of normal modes increases.[43] The five predicted Raman active internal modes for the normal structure can be attributed to the signals at 176.5 ± 3 cm^{-1}, 352 ± 3 cm^{-1}, 447 ± 3 cm^{-1}, 573.5 ± 3 cm^{-1}, and 647 ± 3 cm^{-1}. The weak band at 251 ± 3 cm^{-1}, and the shoulders and broadening observed for most of the signals are direct consequences of the non-zero degree of inversion, as will be discussed below. Even the sample with a degree of inversion close to 0 (ZFO_773, $x = 0.074 ± 0.011$) shows all the mentioned deviations.

Distinctive changes can be observed in the Raman scattering as the degree of inversion of the ZFO samples increases. Fig. 2.3 shows the magnification of four different regions of the Raman spectra presented above. The first interval, from 141.5 cm^{-1} to 202 cm^{-1} (Fig. 2.3A), exhibits pronounced changes. As the degree of inversion increases, a band almost imperceptible for $x = 0.074 ± 0.011$ becomes higher in intensity at 156 ± 3 cm^{-1} and the sharp signal observed at 176.5 ± 3 cm^{-1} decreases in intensity. Interestingly, this decrease is accompanied by a growth of a shoulder at higher wavenumbers, resulting in a broad band from 168 cm^{-1} to 198 cm^{-1}. Supposing that the Raman mode at 176.5 ± 3 cm^{-1} is due to vibrations of the AO_4 tetrahedral groups, the broadening of this band can be explained by the exchange of Zn atoms by lighter Fe atoms, resulting in a shift in the vibration frequency to higher wavenumbers.
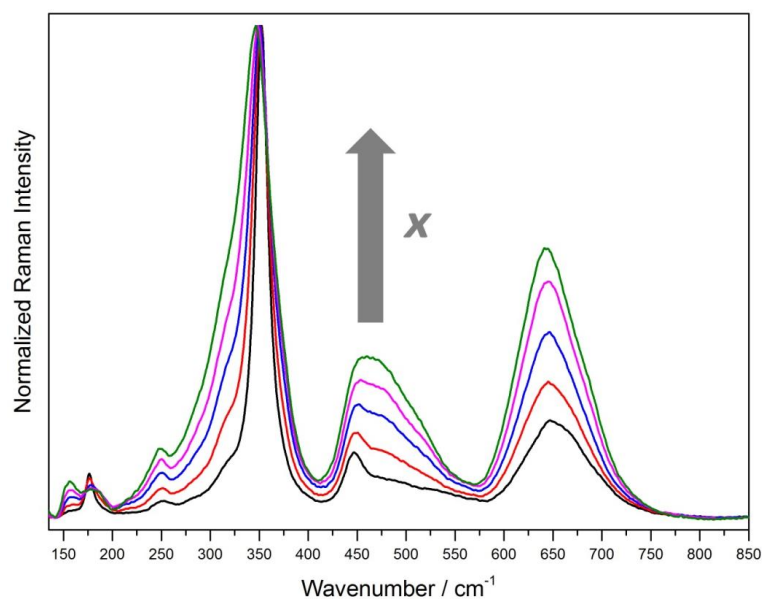
Fig. 2.2. Normalized Raman spectra of the ZFO samples with increasing degree of inversion (— ZFO_773, $x = 0.074 \pm 0.011$; — ZFO_873, $x = 0.104 \pm 0.013$; — ZFO_973, $x = 0.134 \pm 0.008$; — ZFO_1073, $x = 0.159 \pm 0.010$; — ZFO_1173, $x = 0.203 \pm 0.017$) obtained using a 785 nm laser as the excitation source.

In the region from 215 cm^{-1} to 415 cm^{-1} (Fig. 2.3B), an increase in the intensity of the weak signal at 251 ± 3 cm^{-1} and a broadening of the main band at 352 ± 3 cm^{-1} with a small shift of the maximum to smaller wavenumbers are observed as the degree of inversion of the samples increases. The broadening is due to the growth of the shoulder situated at 315 ± 3 cm^{-1}. This shoulder exhibits a weak intensity for the sample with $x = 0.074 \pm 0.011$. Supposing that the signals in this spectral region are predominantly ruled by the vibration of the AO$_6$ octahedral groups, the growth of this shoulder at lower wavenumbers is in concordance with the exchange of Fe atoms by heavier Zn atoms. Regarding the behavior of the weak signal at 251 ± 3 cm^{-1}, it can be assumed that it arises due to the perturbation in the symmetry produced by the cation disordering. Hence, this signal is not one of the five predicted Raman active internal modes for the normal structure.

Prominent changes in the Raman spectra are noticed in the interval from 415 cm^{-1} to 570 cm^{-1} (Fig. 2.3C). As the degree of inversion increases, the shoulder of the band observed at 447 ± 3 cm^{-1} for the sample with $x = 0.074 \pm 0.011$ grows

markedly. This finally results in a broad band from 415 cm^{-1} to 560 cm^{-1} with a maximum at 460 ± 3 cm^{-1} for the sample with x = 0.203 ± 0.017. Supposing that the signal at 447 ± 3 cm^{-1} arises from the vibrations of the AO_4 tetrahedral groups, the increase in the intensity of the shoulder at higher wavenumbers is again a direct consequence of the exchange of Zn atoms by lighter Fe atoms. As was mentioned above, the Raman active internal mode at 573.5 ± 3 cm^{-1} is not intense enough to be detected using a 785 nm excitation source. Despite this signal is observed in the spectra obtained using 532 nm and 633 nm laser excitations, the intensity decreases rapidly as the degree of inversion increases (Fig. A5). This suggests that the vibration of Zn atoms in the tetrahedral sites is also related to this Raman band. Because the signal decreases in intensity with the increasing degree of inversion, the weak band becomes rapidly imperceptible.

A particular change is observed in the region between 575 cm^{-1} and 730 cm^{-1} (Fig. 2.3D). As the degree of inversion increases from 0.074 ± 0.011 to 0.203 ± 0.017, the intensity of the broad band at 647 ± 3 cm^{-1} grows markedly. The increase in the relative intensity of this band in comparison to the main signal at 352 ± 3 cm^{-1} can clearly be seen in Fig. 2.2. In the Raman spectra measured with 532 nm and 633 nm laser excitations, the band at 647 ± 3 cm^{-1} becomes the main signal for the samples having higher degrees of inversion (Fig. A5). This increase in intensity is accompanied by a shift of the position of the maximum from 647 ± 3 cm^{-1} to 642 ± 3 cm^{-1}.

It should be noticed that the ratio between two Raman scattering signals seems to depend on the degree of inversion. The intensity ratio between the Raman shifts at 352 and 647 cm^{-1} vs. the degree of inversion was fitted with an exponential decay function. The obtained results are shown in the supporting information (Fig. A8).
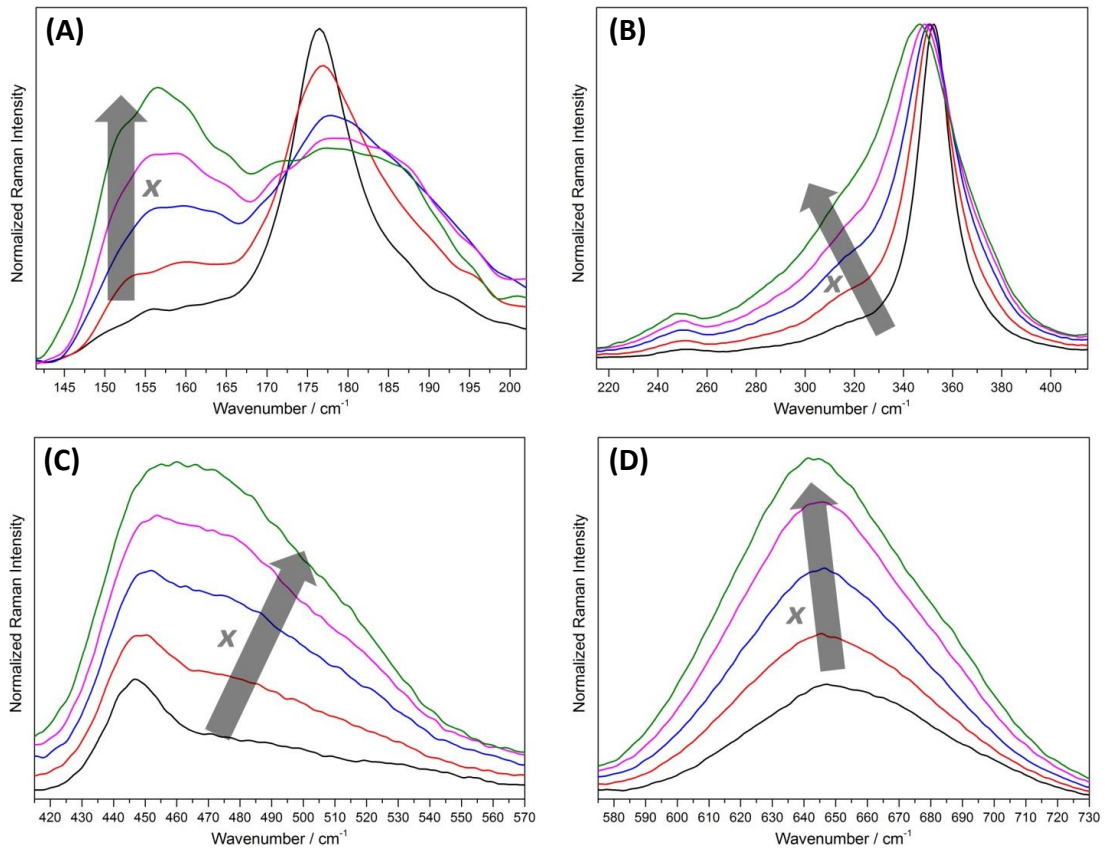
Fig. 2.3. Raman spectra (785 nm excitation source) from **(A)** 141.5 cm^{-1} to 202 cm^{-1}, **(B)** 215 cm^{-1} to 415 cm^{-1}, **(C)** 415 cm^{-1} to 570 cm^{-1}, and **(D)** 575 cm^{-1} to 730 cm^{-1} of the ZFO samples with increasing degree of inversion (— ZFO_773, x = 0.074 ± 0.011; — ZFO_873, x = 0.104 ± 0.013; — ZFO_973, x = 0.134 ± 0.008; — ZFO_1073, x = 0.159 ± 0.010; — ZFO_1173, x = 0.203 ± 0.017).

Fig. 2.4A shows the calculated Raman spectra of normal and inverse ZFO. The position and relative intensity of the calculated frequencies for a degree of inversion of x = 0 show a reasonably good agreement with the experimental result obtained for $x ≈ 0.073$. It is worth mentioning that the FWHM of the Raman signals cannot be calculated (therefore, an arbitrary value of 8 cm^{-1} was used to plot the results) and that vibrational wavenumbers from DFT calculations are typically larger than the observed experimentally. [44] This is not only due to the harmonic approximation but also to the finite basis sets.[44] Furthermore, the computation of vibrational wavenumbers was shown to be dependent on the method.[44,45] Howard *et al.* considered vibrational wavenumbers within 20 cm^{-1} of the reference values as accurate. Thus, the calculated spectrum for x = 0, with deviations of 15.5 to 48 cm^{-1}

(5.7 to 8.8%, respectively) from the experimental data obtained for a ZFO sample with $x \approx 0.073$, is reasonably good. Scaling factors are often applied to improve the agreement between the calculated and experimental results.[44] Using scaling factors would also align the calculated spectrum presented in Fig. 2.4B with the experimental spectrum obtained for ZFO with $x \approx 0.073$. However, this is not scientifically reasonable since the degree of inversion of the calculated ZFO ($x = 0$) and the synthesized ZFO ($x \approx 0.073$) are not equal. Since the maximal inversion achieved experimentally is $x = 0.203 \pm 0.017$, the calculated spectrum with an inversion of $x = 1$ cannot be compared directly. Nevertheless, the trends observed experimentally upon increasing disorder may be related to the theoretical spectra.
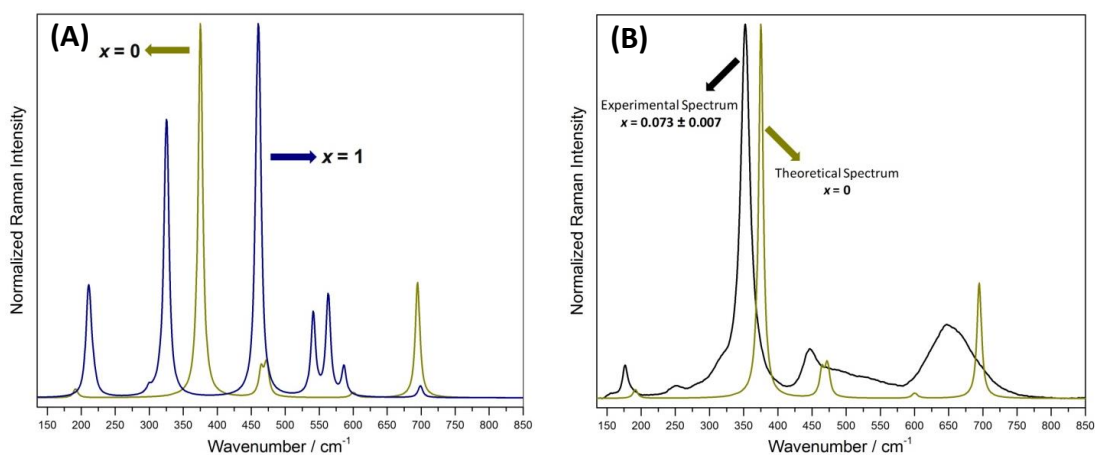
Fig. 2.4. **(A)** Calculated Raman spectra of ZFO with $x = 0$ and $x = 1$. **(B)** Comparison between the calculated Raman spectrum of ZFO with $x = 0$ and the experimental Raman spectrum of ZFO with $x = 0.074 \pm 0.011$.

In the region from 150 cm^{-1} to 250 cm^{-1} it can be seen a prominent signal shift to higher wavenumbers with increasing intensity as the inversion increases. In agreement with the experimental result, the Raman signal observed in this region for $x = 0$ is shifted to higher wavenumbers in the calculated spectrum for $x = 1$. Vibrational analysis confirms the assumption that this signal arises from wagging of the tetrahedral ion, explaining the shift to higher wavenumbers when Zn atoms are replaced by the lighter Fe atoms.

The Raman signal located at 375 cm^{-1} for the normal ZFO shifts to 325 cm^{-1} and exhibits a shoulder at 310 cm^{-1}. This trend is once more in very good agreement with the experimental results. Vibrations of both, the octahedrally and tetrahedrally coordinated ions contribute to this signal.

The double peak obtained at 464 cm^{-1} and 472 cm^{-1} for $x = 0$ shifts to slightly smaller wavenumbers (459 cm^{-1} and 462 cm^{-1}) under inversion and increases in intensity, being the most pronounced signal for $x = 1$. Although the vibrational analysis mainly ascribes these signals to the wagging of the tetrahedrally coordinated ions, as was supposed above, this behavior is not completely in line with the experimental results shown in Fig. 2.3C.

The calculated spectrum for $x = 0$ shows a small signal at 600 cm^{-1}, which splits into three signals at 541 cm^{-1}, 563 cm^{-1}, and 586 cm^{-1} for $x = 1$. This effect cannot be observed in the experimental spectrum obtained with 785 nm laser excitation since those signals vanish between the rather broad bands located at higher and lower wavenumbers. Nevertheless, the spectra measured with 532 nm and 633 nm laser excitations (Fig. A5) show a weak signal at 573 ± 3 cm^{-1}, comparable with the calculated signal at 600 cm^{-1}, for the sample with $x = 0.074 \pm 0.011$. The intensity of this signal decreases as the degree of inversion increases. This decrease might be attributed to the split of this signal into three bands at lower wavenumbers, which contribute to the broadness of the band observed between 415 cm^{-1} and 560 cm^{-1}.

The calculated signal at 695 cm^{-1} undergoes a slight shift to 699 cm^{-1} upon inversion, accompanied by a decreased intensity, which is contradictory to the experimental results (see Fig. 2.3D). This signal can mainly be ascribed to a symmetrical stretching of the ZnO_4-tetrahedra in the normal ZFO, and FeO_4-tetrahedra in the inverse ZFO.

As becomes clear from the above discussion, the degree of inversion has a great effect on the Raman scattering properties of ZFO. It is not surprising to find

spectra in the literature showing different signal positions as well as diverse assignments.[26,46] Furthermore, most authors presume a normal structure for the ZFO samples, thus not determining the degree of inversion. This assumption is not necessarily correct as the ordering of the sample can be easily modified by the temperature of preparation. Moreover, there are reports showing low-temperature synthesized ZFO nanoparticles with high degrees of inversion.[18–20] Wang *et al.*[26] presented a Raman spectrum of ZFO with x = 0.10 together with an assignment of the bands. The signals at 221 cm^{-1}, 246 cm^{-1}, 355 cm^{-1}, 451 cm^{-1}, and 647 cm^{-1} were identified as the five Raman active internal modes predicted by the group-theoretical analysis, having F_{2g}, E_g, F_{2g}, F_{2g}, and A_{1g} symmetry, respectively. The authors attributed the signals above 600 cm^{-1} to the motion of oxygen in the tetrahedral AO_4 groups. The low-frequency modes were attributed to vibrations in the octahedral BO_6 sites. The distinctive signals at 355 cm^{-1}, 451 cm^{-1}, and 647 cm^{-1} agree with the results presented in this work but a discrepancy is found with the vibrations at 221 cm^{-1} and 246 cm^{-1}. As was mentioned above, the weak band at 251 ± 3 cm^{-1} arises from the disorder of the sample and is not one of the Raman active internal modes for the normal structure predicted by the group-theoretical analysis. The signal at 221 cm^{-1} was not observed in the present work neither for the 785 nm nor for the 532 nm and 633 nm laser excitations (Fig. A5). A signal at 176.5 cm^{-1} appears in the result presented by Wang *et al.* but the resolution in this region, close to the acquisition limit of the spectrum, is poor. Finally, the internal mode reported in the present work at 573.5 ± 3 cm^{-1} is not observed by Wang *et al.* because this signal becomes very weak while using a 785 nm laser excitation. The assignment of the Raman active internal modes proposed in this work and the assignment made by Wang *et al*. are presented in Table 2.2.

The UV-Vis-NIR diffuse reflectance spectra of the different ZFO samples are shown in Fig. 2.5. Three predominant absorption bands are observed in the regions from 220 nm to 670 nm, 670 nm to 950 nm, and 950 nm to 1600 nm. The bands around 795 nm (ca. 1.56 eV) and 1200 nm (ca. 1.03 eV) present typical Gaussian

shapes, whereas the band with a maximum around 425 nm saturates the detector and then decreases in intensity from ca. 400 nm. The former band exhibits masked signals around 451 nm, 532 nm, and 614 nm. The determination and origin of these signals will be discussed below. Less reflectivity, namely more absorption, in the region between 500 nm and 700 nm is observed as the degree of inversion of the sample increases. This explains the darkening of the samples as x changes from 0.074 ± 0.011 to 0.203 ± 0.017 (Fig. A9). The reflectivity of NIR radiation between 1400 nm and 2000 nm also decreases as the degree of inversion increases.

Table 2.2. Assignment of the Raman active internal modes for normal ZFO proposed in the present work together with the assignment made by Wang *et al.*[26]

Raman active internal mode	Frequency / cm^{-1}		
	This work		Wang *et al.*
	Theoretical	Experimental	
F$_{2g}$	191	176.5 ± 3	221
E$_g$	375	352 ± 3	246
F$_{2g}$	464/472	447 ± 3	355
F$_{2g}$	600	573 ± 3	451
A$_{1g}$	695	647 ± 3	647

Three types of electronic transitions are found in Fe^{3+} rich oxides: ligand field transitions, transitions due to ligand-to-metal charge-transfer, and transitions resulting from simultaneous excitation of magnetically-coupled Fe^{3+} neighboring cations.[47] The latter transitions are expected to be negligible for ZFO since there are no face-sharing FeO$_6$ structures. The ligand field transitions for a Fe^{3+} ion occupying an octahedral site are due to the excitation of electrons from t$_{2g}$ into e$_g$ orbitals. These orbitals are formed by the splitting of the 3d orbitals due to the electrical field of the surrounding O^{2-} anions. Furthermore, both the t$_{2g}$ and e$_g$ orbitals are

also split because of the exchange energy (Russell-Saunders coupling) and the resulting energetic states can be found in the respective Tanabe-Sugano diagram (Fig. A10). According to this diagram, a high spin Fe^{3+} ion exhibits a $^6A_{1g}$ ground state and the first three possible electronic transition are: $^6A_{1g}(G) \rightarrow {}^4T_{1g}(G)$ $[(t^{\alpha}_{2g})^3(e^{\alpha}_g)^2 \rightarrow (t^{\alpha}_{2g})^3(e^{\alpha}_g)^1(t^{\beta}_{2g})^1]$, $^6A_{1g}(G) \rightarrow {}^4T_{2g}(G)$ $[(t^{\alpha}_{2g})^3(e^{\alpha}_g)^2 \rightarrow (t^{\alpha}_{2g})^3(e^{\alpha}_g)^1(t^{\beta}_{2g})^1]$, and $^6A_{1g}(G) \rightarrow {}^4A_{1g}(G)$ $[(t^{\alpha}_{2g})^3(e^{\alpha}_g)^2 \rightarrow (t^{\alpha}_{2g})^2(t^{\beta}_{2g})^1(e^{\alpha}_g)^2]$. Although all the transitions from the ground $^6A_{1g}$ state are spin and parity-forbidden, they become allowed due to the magnetic coupling of electronic spins of neighboring Fe^{3+} cations.[48–50]
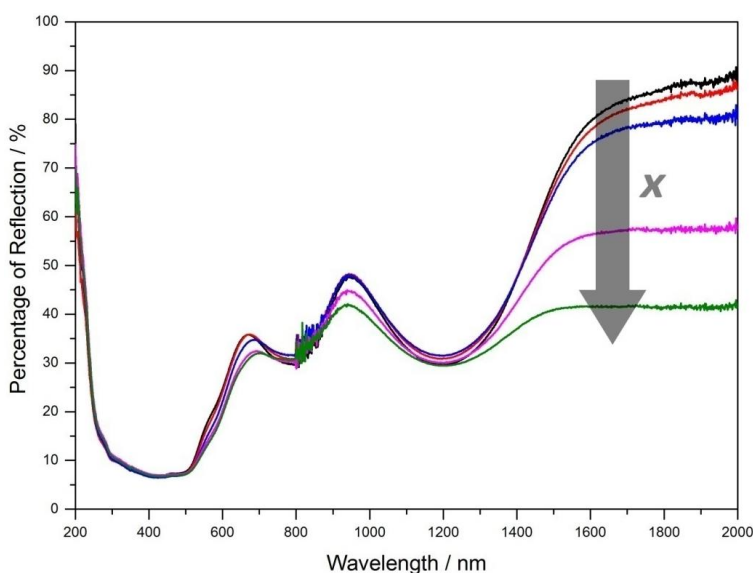
Fig. 2.5. UV-Vis-NIR diffuse reflectance spectra of the ZFO samples with increasing degree of inversion (— ZFO_773, x = 0.074 ± 0.011; — ZFO_873, x = 0.104 ± 0.013; — ZFO_973, x = 0.134 ± 0.008; — ZFO_1073, x = 0.159 ± 0.010; — ZFO_1173, x = 0.203 ± 0.017).

On the basis of the Tanabe-Sugano diagram, an assignment of the experimentally observed UV-Vis-NIR bands was done (Table 2.3). The signals at 1200 nm and 795 nm can be assigned to the $^6A_{1g} \rightarrow {}^4T_{1g}(G)$ and $^6A_{1g} \rightarrow {}^4T_{2g}(G)$ transitions, respectively. This corresponds with a value of ca. 14164 cm^{-1} (1.76 eV) for the energy of the octahedral crystal field, and ca. 624 cm^{-1} for the Racah parameter (Fig. A10). Additionally, the energy for the $^6A_{1g} \rightarrow {}^4A_{1g}(G)$ and $^6A_{1g} \rightarrow {}^4T_{2g}(D)$ transitions is estimated to be ca. 20248 cm^{-1} (494 nm, 2.51 eV) and 22300 cm^{-1} (448 nm, 2.76 eV), respectively. The latter value is in good agreement with the

signal at 451 nm masked within the broad band from 220 to 670 nm. Transitions from non-bonding molecular orbitals localized on the oxygen atoms to the antibonding t_{2g} Fe(3d) orbitals are reported in the literature for a vast variety of iron-based oxides.[47,51] Because this electronic excitation is responsible for the optical band gap of the semiconducting ZFO, the derivation absorption spectrum fitting method (DASF)[33] was applied to get more insight into the energy and the nature of the transition. Because the measured diffuse reflectance spectra do not correlate directly to the absorption spectra, the Kubelka-Munk radiative transfer model[45] was first applied to determine the absorption coefficient. Rietveld refinement (Table 2.1) and SEM pictures (Fig. A11) reveal that the particles have similar size and shape. Thus, it was assumed that the different ZFO samples have the same scattering properties. The full mathematical deduction of the DASF model for diffuse reflectance data is presented in the supporting information. As can be seen from Fig. 2.6, three clear bands are observed at 2.02 eV (614 nm), 2.33 eV (532 nm), and 2.75 eV (451 nm), and a weak signal is observed at 2.58 eV (481 nm). The bands at 2.58 eV and 2.75 eV can be assigned to the $^6A_{1g} \rightarrow {}^4A_{1g}(G)$ and $^6A_{1g} \rightarrow {}^4T_{2g}(D)$ transitions, respectively (Fig. A10). Consequently, the signal observed at 2.02 eV can be attributed to the $O^{2-} + Fe^{3+} \rightarrow O^- + Fe^{2+}$ transition. Moreover, the DASF analysis shows that this is an allowed and indirect transition (Fig. A12). Finally, the band at 2.33 eV can be attributed to a direct $O^{2-} + Fe^{3+} \rightarrow O^- + Fe^{2+}$ transition. Table 2.3 lists the proposed assignment for the experimentally observed electronic transitions of ZFO.

Surprisingly, all the bands can be assigned considering only electronic transitions in the octahedrally coordinated Fe^{3+} ions. Similar results are known for other iron-based oxides having Fe^{3+} in both tetrahedral and octahedral positions.[47] Pailhé et al.[27] also assigned the UV-Vis-NIR absorption bands of a ZFO sample with x = 0.140 to transitions involving Fe^{3+} in octahedral sites. Nevertheless, despite the authors deduced some of the transitions considering the orbital splitting due to the Russell-Saunders coupling, they mixed two different models by assigning transitions

on the basis of a simple splitting of the Fe(3d) orbitals (into t_{2g} and e_g orbitals) as well.

Table 2.3. Assignment of the experimentally observed electronic transitions of ZFO according to the ligand field theory considering Russell-Saunders coupling.

Wavelength / nm	Transition
1200	$^6A_{1g} \rightarrow {}^4T_{1g}(G)$
795	$^6A_{1g} \rightarrow {}^4T_{2g}(G)$
614	$O^{2-} + Fe^{3+} \rightarrow O^- + Fe^{2+}$ (indirect)
532	$O^{2-} + Fe^{3+} \rightarrow O^- + Fe^{2+}$ (direct)
481	$^6A_{1g} \rightarrow {}^4A_{1g}(G)$
451	$^6A_{1g} \rightarrow {}^4T_{2g}(D)$
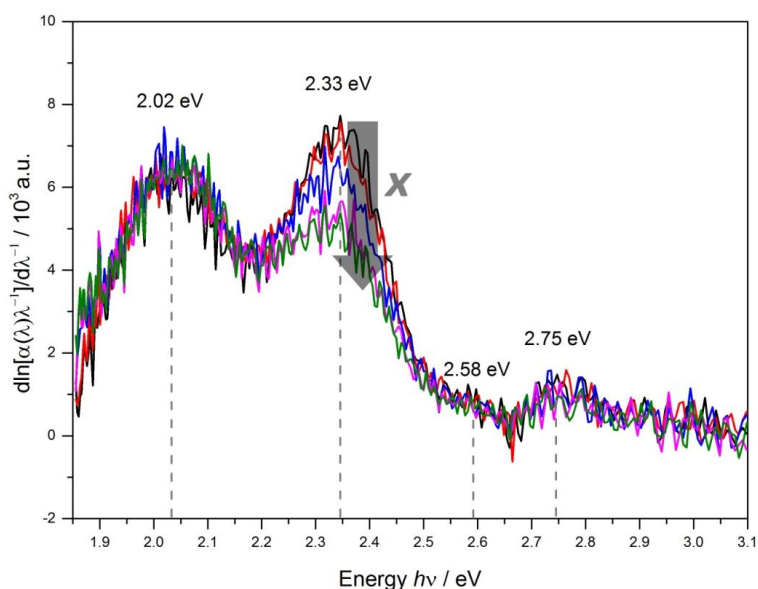
Fig. 2.6. Derivation of Absorption Spectrum Fitting (DASF) method calculated from 670 nm to 400 nm for the ZFO samples with increasing degree of inversion (— ZFO_773, $x = 0.074 \pm 0.011$; — ZFO_873, $x = 0.104 \pm 0.013$; — ZFO_973, $x = 0.134 \pm 0.008$; — ZFO_1073, $x = 0.159 \pm 0.010$; — ZFO_1173, $x = 0.203 \pm 0.017$).

By comparing the spectra for the ZFO samples with different degrees of inversion, the presence of transitions involving tetrahedrally coordinated Fe^{3+} ions can be analyzed. The UV-Vis-NIR spectra from 0.90 to 6.0 eV and the deconvolution of the three distinctive reflection bands employing Gaussian shaped curves are shown in Fig. 2.7. As the degree of inversion of the samples increases, the percentage of reflection at ca. 1.5 eV becomes higher (absorption decreases), and a broadening is observed for the band at ca. 1.0 eV (absorption increases). The amount of Fe^{3+} ions in octahedrally coordinated sites has a considerable effect on the signal around 1.5 eV. As this value decreases, the absorption in this region becomes smaller. This effect is consistent with the assignment of this band to a transition involving Fe^{3+} ions in octahedral sites. On the other hand, an increasing amount of Fe^{3+} ions in tetrahedrally coordinated sites generates a higher absorption in the region around 1.0 eV. This signal cannot be attributed solely to transitions involving Fe^{3+} ions in tetrahedral sites because the intensity is already very high for the sample containing only 3.8 % ($x = 0.074 \pm 0.011$) of tetrahedrally coordinated Fe^{3+} ions and does not grow proportionally as the degree of inversion increases. Nevertheless, considering that the transitions originating from tetrahedrally coordinated Fe^{3+} ions might not be significantly different in energy than those arising from the octahedrally coordinated,[51] an overlapping of both types of transitions can be expected at around 1.0 eV. Therefore, the broadening of the band in the NIR region close to 1.0 eV can be explained by the contribution of the ligand field transitions due to Fe^{3+} ions occupying tetrahedral sites.
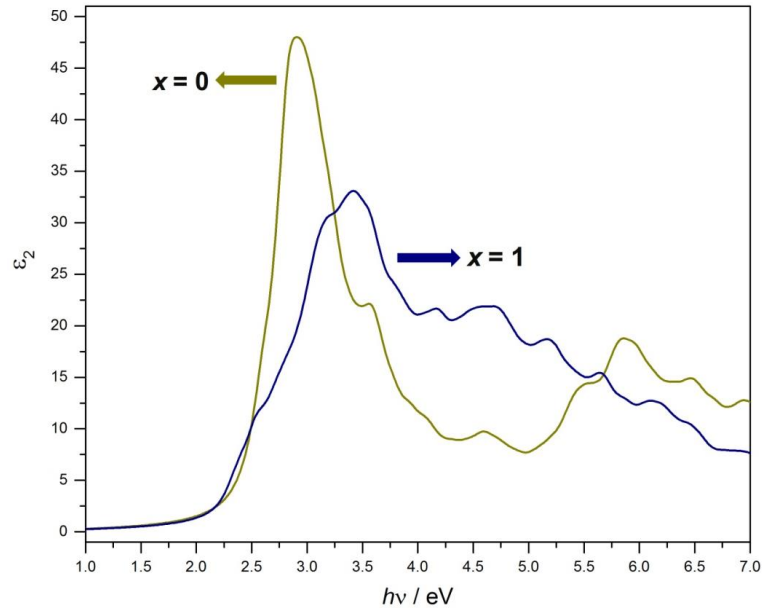
The imaginary part of the dielectric function, ε_2, which is directly related to the probability of photon absorption[52], was calculated in dependency on the excitation energy for ZFO with a degree of inversion of $x = 0$ and $x = 1$. The resulting spectra are given in Fig. 2.8.
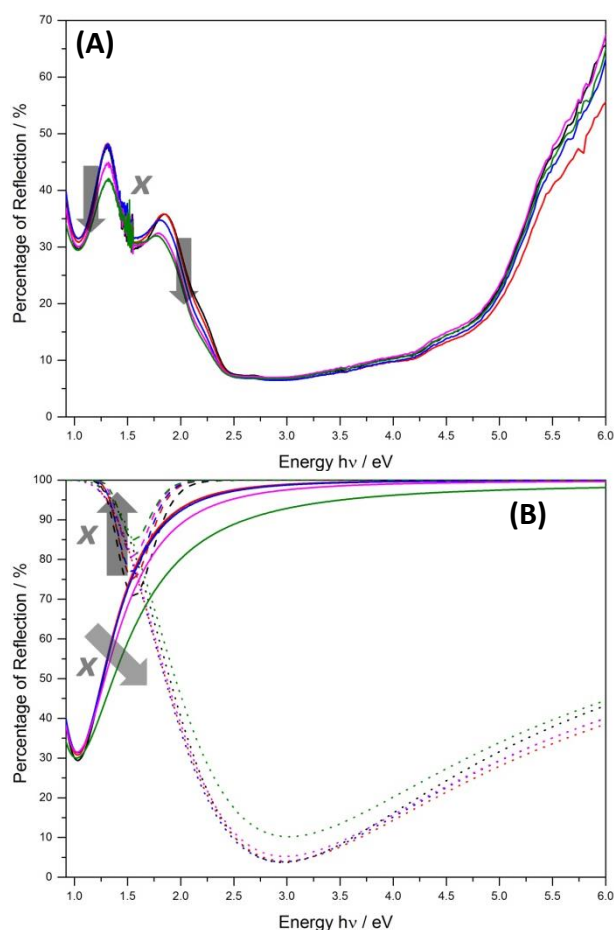
Fig. 2.7. **(A)** UV-VIS-NIR diffuse reflectance spectra from 0.9 to 6.0 eV of the ZFO samples with increasing degree of inversion. **(B)** Deconvolution of the UV-VIS-NIR diffuse reflectance spectra employing Gaussian-shaped curves. The full line, dash line, and pointed line corresponds to the reflection bands at 1.03 eV, 1.56 eV, and 3.00 eV, respectively. ▬ ZFO_773, x = 0.074 ± 0.011; ▬ ZFO_873, x = 0.104 ± 0.013; ▬ ZFO_973, x = 0.134 ± 0.008; ▬ ZFO_1073, x = 0.159 ± 0.010; ▬ ZFO_1173, x = 0.203 ± 0.017.

Since the used theoretical approach is no multideterminantal ansatz, intra-atomic transitions cannot be described. The onset of the spectrum for the normal and the inverse ZFO is located at 2.3 and 2.1 eV, respectively. The position of the O^{2-} + Fe^{3+} → O^- + Fe^{2+} transition is in excellent agreement with the experimental result. Furthermore, both experiment and theory state that there is no difference in the band gap energy for different degrees of inversion. The theoretical spectrum in Fig. 2.8 shows that, upon inversion, the intensity of the band gap excitation decreases dramatically. A similar effect can be seen in Fig. 2.6 for the signal

attributed to the direct band gap transition. As the degree of inversion increases, the area of the signal, and thus the absorption coefficient, decreases.

Fig. 2.8. Calculated imaginary part of the dielectric function ε_2 for optical spectrum of ZFO for ZFO with $x = 0$ and $x = 1$.

2.6. Conclusions

The effect of the degree of inversion on the Raman scattering and the UV-VIS-NIR reflectivity of spinel ZFO is elucidated. Based on the strong evidence collected, a new assignment for both, the Raman active internal modes and the electronic transitions is proposed for normal ZFO. As the degree of inversion increases, a larger contribution from the ligand field transitions of the tetrahedrally coordinated Fe^{3+} ions into the visible light absorptivity of the material is observed, producing a characteristic darkening of the sample. Conversely, no effect is observed on the energies of the transitions due to ligand-to-metal charge-transfer between O^{2-} and Fe^{3+} ions. Thereby, the band gap energy, with values of 2.02 eV and 2.33 eV for the indirect and direct transition, respectively, is found to be independent of the degree of inversion.

2.7 Acknowledgements

2.8 References

(1)   Sharma, R.; Thakur, P.; Sharma, P.; Sharma, V. Ferrimagnetic Ni^{2+} Doped Mg-Zn Spinel Ferrite Nanoparticles for High Density Information Storage. *J. Alloys Compd.* **2017**, *704*, 7–17.

(2)   Pileni, M. P. Magnetic Fluids: Fabrication, Magnetic Properties, and Organization of Nanocrystals. *Adv. Funtional Mater.* **2001**, *11*, 323–336.

(3)   Pardavi-Horvath, M. Microwave Applications of Soft Ferrites. *J. Magn. Magn. Mater.* **2000**, *215*, 171–183.

(4)   Yan, K.; Wu, X.; An, X.; Xie, X. Facile Synthesis and Catalytic Property of Spinel Ferrites by a Template Method. *J. Alloys Compd.* **2013**, *552*, 405–408.

(5)   Van Groenou, A. B.; Bongers, P. F.; Stuyts, A. L. Magnetism, Microstructure and Crystal Chemistry of Spinel Ferrites. *Mater. Sci. Eng.* **1968**, *3*, 317–392.

(6)   Taffa, D. H.; Dillert, R.; Ulpe, A. C.; Bauerfeind, K. C. L.; Bredow, T.; Bahnemann, D. W.; Wark, M. Photoelectrochemical and Theoretical Investigations of Spinel Type Ferrites ($M_xFe_{3-x}O_4$) for Water Splitting: A Mini-Review. *J. Photonics Energy* **2016**, *7*, 012009.

(7)   Dillert, R.; Taffa, D. H.; Wark, M.; Bredow, T.; Bahnemann, D. W. Research Update: Photoelectrochemical Water Splitting and Photocatalytic Hydrogen Production Using Ferrites (MFe_2O_4) under Visible Light Irradiation. *APL Mater.* **2015**, *3*, 104001.

(8)   Song, G.; Xin, F.; Yin, X. Photocatalytic Reduction of Carbon Dioxide over

ZnFe$_2$O$_4$/TiO$_2$ Nanobelts Heterostructure in Cyclohexanol. *J. Colloid Interface Sci.* **2015**, *442*, 60–66.

(9) Boumaza, S.; Boudjemaa, A.; Bouguelia, A.; Bouarab, R.; Trari, M. Visible Light Induced Hydrogen Evolution on New Hetero-System ZnFe$_2$O$_4$/SrTiO$_3$. *Appl. Energy* **2010**, *87*, 2230–2236.

(10) Tahir, A. A.; Wijayantha, K. G. U. Photoelectrochemical Water Splitting at Nanostructured ZnFe$_2$O$_4$ Electrodes. *J. Photochem. Photobiol. A Chem.* **2010**, *216*, 119–125.

(11) Kim, J. H.; Kim, J. H.; Jang, J. W.; Kim, J. Y.; Choi, S. H.; Magesh, G.; Lee, J.; Lee, J. S. Awakening Solar Water-Splitting Activity of ZnFe$_2$O$_4$ Nanorods by Hybrid Microwave Annealing. *Adv. Energy Mater.* **2015**, *5*, 1401933.

(12) Valenzuela, M. A.; Bosch, P.; Jiménez-Becerrill, J.; Quiroz, O.; Páez, A. I. Preparation, Characterization and Photocatalytic Activity of ZnO, Fe$_2$O$_3$ and ZnFe$_2$O$_4$. *J. Photochem. Photobiol. A Chem.* **2002**, *148*, 177–182.

(13) Casbeer, E.; Sharma, V. K.; Li, X. Z. Synthesis and Photocatalytic Activity of Ferrites under Visible Light: A Review. *Sep. Purif. Technol.* **2012**, *87*, 1–14.

(14) Arimi, A.; Megatif, L.; Granone, L. I.; Dillert, R.; Bahnemann, D. W. Visible-Light Photocatalytic Activity of Zinc Ferrites. *J. Photochem. Photobiol. A Chem.* **2018**, *366*, 118-126.

(15) O'Neill, H. S. C. Temperature Dependence of the Cation Distribution in Zinc Ferrite (ZnFe$_2$O$_4$) from Powder XRD Structural Refinements. *Eur. J. Miner.* **1992**, *4*, 571–580.

(16) Pavese, A.; Levy, D.; Hoser, A. H. Cation Distribution in Synthetic Zinc Ferrite (Zn$_{0.97}$Fe$_{2.02}$O$_4$) from in Situ High-Temperature Neutron Powder Diffraction. *Am. Mineral.* **2000**, *85*, 1497–1502.

(17) Bræstrup, F.; Hauback, B. C.; Hansen, K. K. Temperature Dependence of the Cation Distribution in ZnFe$_2$O$_4$ Measured with High Temperature Neutron Diffraction. *J. Solid State Chem.* **2008**, *181*, 2364–2369.

(18) Akhtar, M. J.; Nadeem, M.; Javaid, S.; Atif, M. Cation Distribution in Nanocrystalline ZnFe$_2$O$_4$ Investigated Using X-Ray Absorption Fine Structure Spectroscopy. *J. Phys. Condens. Matter* **2009**, *21*, 405303.

(19) Kamiyama, T.; Haneda, K.; Sato, T.; Ikeda, S.; Asano, H. Cation Distribution in ZnFe$_2$O$_4$ Fine Particles Studied by Neutron Powder Diffraction. *Solid State*

Commun. **1992**, *81*, 563–566.

(20)   Nakashima, S.; Fujita, K.; Tanaka, K.; Hirao, K.; Yamamoto, T.; Tanaka, I. First-Principles XANES Simulations of Spinel Zinc Ferrite with a Disordered Cation Distribution. *Phys. Rev. B* **2007**, *75*, 174443.

(21)   Kurian, J.; Mathew, M. J. Structural, Optical and Magnetic Studies of CuFe$_2$O$_4$, MgFe$_2$O$_4$ and ZnFe$_2$O$_4$ Nanoparticles Prepared by Hydrothermal/Solvo-thermal Method. *J. Magn. Magn. Mater.* **2018**, *451*, 121–130.

(22)   Šepelák, V.; Tkáčová, K.; Boldyrev, V. V.; Wigmann, S.; Becker, K. D. Mechanically Induced Cation Redistribution in ZnFe$_2$O$_4$ and Its Thermal Stability. *Phys. B* **1997**, *234–236*, 617–619.

(23)   Mozaffari, M.; Eghbali Arani, M.; Amighian, J. The Effect of Cation Distribution on Magnetization of ZnFe$_2$O$_4$ Nanoparticles. *J. Magn. Magn. Mater.* **2010**, *322*, 3240–3244.

(24)   Yuan, Q.; Pan, L.; Liu, R.; Wang, J.; Liao, Z.; Qin, L.; Bi, J.; Gao, D.; Wu, J. Cation Distribution and Magnetism in Quenched ZnFe$_2$O$_4$. *J. Electron. Mater.* **2018**, *47*, 3608–3614.

(25)   Harris, V. G.; Šepelák, V. Mechanochemically Processed Zinc Ferrite Nanoparticles: Evolution of Structure and Impact of Induced Cation Inversion. *J. Magn. Magn. Mater.* **2018**, *465*, 603–610.

(26)   Wang, Z.; Schiferl, D.; Zhao, Y.; O'Neill, H. S. C. High Pressure Raman Spectroscopy of Spinel-Type Ferrite ZnFe$_2$O$_4$. *J. Phys. Chem. Solids* **2003**, *64*, 2517–2523.

(27)   Pailhé, N.; Wattiaux, A.; Gaudon, M.; Demourgues, A. Correlation between Structural Features and Vis-NIR Spectra of α-Fe$_2$O$_3$ Hematite and AFe$_2$O$_4$ Spinel Oxides (A = Mg, Zn). *J. Solid State Chem.* **2008**, *181*, 1040–1047.

(28)   Lagarec, K.; Rancourt, D. G. Recoil 1.05 Mössbauer Analysis Software. *Dep. Physics, Univ. Ottawa, Ottawa, ON, Canada* **2002**.

(29)   Dovesi, R.; Orlando, R.; Civalleri, B.; Roetti, R.; Saunders, V. R.; Zicovich-Wilson, C. M. CRYSTAL: A Computational Tool for the Ab Initio Study of the Electronic Properties of Crystals. *Z. Krist.* **2005**, *220*, 571–573.

(30)   Krukau, A. V.; Vydrov, O. A.; Izmaylov, A. F.; Scuseria, G. E. Influence of the Exchange Screening Parameter on the Performance of Screened Hybrid Functionals. *J. Chem. Phys.* **2006**, *125*, 224106.

(31) Stephens, P. J.; Devlin, F. J.; Chabalowski, C. F.; Frisch, M. J. Ab Initio Calculation of Vibrational Absorption and Circular Dichroism Spectra Using Density Functional Force Fields. *J. Phys. Chem.* **1994**, *98*, 11623–11627.

(32) Hill, R. J.; Craig, J. R.; Gibbs, G. V. Systematics of the Spinel Structure Type. *Phys. Chem. Miner.* **1979**, *4*, 317–339.

(33) Souri, D.; Tahan, Z. E. A New Method for the Determination of Optical Band Gap and the Nature of Optical Transitions in Semiconductors. *Appl. Phys. B* **2015**, *119*, 273–279.

(34) Kresse, G.; Furthmüller, J. Efficient Iterative Schemes for Ab Initio Total-Energy Calculations Using a Plane-Wave Basis Set. *Phys. Rev. B* **1996**, *54*, 11169–11186.

(35) Hedin, L. New Method for Calculating the One-Particle Green's Function with Application to the Electron-Gas-Problem. *Phys. Rev.* **1965**, *139*, A796–A823.

(36) Rohlfing, M.; Louie, S. G. Electron-Hole Excitations and Optical Spectra from First Principles. *Phys. Rev. B* **2000**, *62*, 4927–4944.

(37) Cornell, R. M.; Schwertmann, U. Characterization. In *The Iron Oxides: Structure, Properties, Reactions, Occurences and Uses*; WILEY-VCH: Darmstadt, **2004**; 139–183.

(38) Callen, H. B.; Harrison, S. E.; Kriessman, C. J. Cation Distributions in Ferrospinels. Theoretical. *Phys. Rev.* **1956**, *103*, 851–856.

(39) Navrotsky, A.; Kleppa, O. J. The Thermodynamics of Cation Distributions in Simple Spinels. *J. Inorg. Nucl. Chem.* **1967**, *29*, 2701–2714.

(40) O'Neill, H. S. C.; Navrotsky, A. Simple Spinels: Crystallographic Parameters, Cation Radii, Lattice Energies, and Cation Distribution. *Am. Mineral.* **1983**, *68*, 181–194.

(41) O'Neill, H. S. C.; Navrotsky, A. Cation Distributions and Thermodynamic Properties of Binary Spinel Solid Solutions. *Am. Mineral.* **1984**, *69*, 733–753.

(42) White, W. B.; DeAngelis, B. A. Interpretation of the Vibrational Spectra of Spinels. *Spectrochim. Acta* **1967**, *23A*, 985–995.

(43) Graves, P. R.; Johnston, C.; Campaniello, J. J. Raman Scattering in Spinel Structure Ferrites. *Mater. Res. Bull.* **1988**, *23*, 1651–1660.

(44) Scott, A. P.; Radom, L. Harmonic Vibrational Frequencies: An Evaluation of

Hartree-Fock, Møller-Plesset, Quadratic Configuration Interaction, Density Functional Theory, and Semiempirical Scale Factors. *J. Phys. Chem.* **1996**, *100*, 16502–16513.

(45) Howard, J. C.; Enyard, J. D.; Tschumper, G. S. Assessing the Accuracy of Some Popular DFT Methods for Computing Harmonic Vibrational Frequencies of Water Clusters. *J. Chem. Phys.* **2015**, *143*, 214103.

(46) Lazarević, Z. Ž.; Sekulić, D. L.; Ivanovski, V. N.; Romčević, N. Ž. A Structural and Magnetic Investigation of the Inversion Degree in Spinel $NiFe_2O_4$, $ZnFe_2O_4$ and $Ni_{0.5}Zn_{0.5}Fe_2O_4$ Ferrites Prepared by Soft Mechanochemical Synthesis. *Int. J. Chem. Mol. Nucl. Mater. Metall. Eng.* **2015**, *9*, 1066–1070.

(47) Sherman, D. M.; Waite, T. D. Electronic Spectra of Fe^{3+} Oxides and Oxide Hydroxides in the near IR to near UV. *Am. Mineral.* **1985**, *70*, 1262–1269.

(48) Ferguson, J.; Guggenheim, H. J.; Tanabe, Y. The Effects of Exchange Interactions in the Spectra of Octahedral Manganese. II. Compounds. *J. Phys. Soc. Japan* **1966**, *21*, 692–704.

(49) Krebs, J. J.; Maisch, W. G. Exchange Effects in the Optical-Absorption Spectrum of Fe^{3+} in Al_2O_3. *Phys Rev B* **1971**, *4*, 757–769.

(50) L. Lohr, L. Spin-Forbidden Electronic Excitations in Transition Metal Complexes. *Coord. Chem. Rev.* **1972**, *8*, 241–259.

(51) Sherman, D. M. The Electronic Structures of Fe^{3+} Coordination Sites in Iron Oxides: Applications to Spectra, Bonding, and Magnetism. *Phys. Chem. Miner.* **1985**, *12*, 161–175.

(52) Yu, P.; Cardona, M. *Fundamentals of Semiconductors*, 4th ed.; Stanley, H. E., Rhodes, W. T., Eds.; Springer, **2010**.

Chapter 3

# Effect of the Degree of Inversion on the Electrical Conductivity of Spinel ZnFe₂O₄

3.1 Foreword

This chapter comprises the manuscript *Effect of the Degree of Inversion on the Electrical Conductivity of Spinel ZnFe₂O₄* by Luis I. Granone, Ralf Dillert, Paul Heitjans, and Detlef W. Bahnemann, published in *ChemistrySelect*, **2019**, 4, 1232-1239. After the effect of the degree of inversion on the photon absorption properties of ZFO were presented in the previous section, another physicochemical property directly related to the photoelectrochemical activity of the material is analyzed in this manuscript. Herein, the charge carrier transport properties of the samples synthesized by the method described in the previous chapter are studied as a function of the degree of inversion. Prof. Dr. Paul Heitjans (Institute of Physical Chemistry and Electrochemistry, Gottfried Wilhelm Leibniz University Hannover) contributed to this manuscript by providing support for the impedance spectroscopy measurements. The figures and tables identified through this chapter with the letter "B" are reproduced in Appendix B.

3.2 Abstract

Spinel ferrites (MFe₂O₄, where M is a metal ion) in general, and zinc ferrite (ZnFe₂O₄, ZFO) in particular, have recently received considerable attention due to promising results in the field of photocatalysis and, especially, photoelectrochemistry. ZFO exhibits a variable crystal structure in which the distribution of the cations between octahedral and tetrahedral sites in the cubic close-packed oxygen lattice, i.e., the degree of inversion, is known to depend closely on the synthetic conditions. Although the effect on the magnetic and optical properties is well known, fundamental research is still missing to fully understand the

impact of the cation distribution on the photoelectrochemical activity. In this context, an utmost important physicochemical property is the electrical conductivity. In this work, the dielectric properties of ZFO samples with degrees of inversion ranging from 0.07 to 0.20 were investigated. The conductivity of the ZFO samples was found to increase as the degree of inversion increases. At an onset value of the degree of inversion between 0.13 and 0.16, the bulk conductivity increases by two orders of magnitude. This increase is a direct evidence of the high impact of the cation arrangement in the crystal lattice on the electronic properties of ZFO.
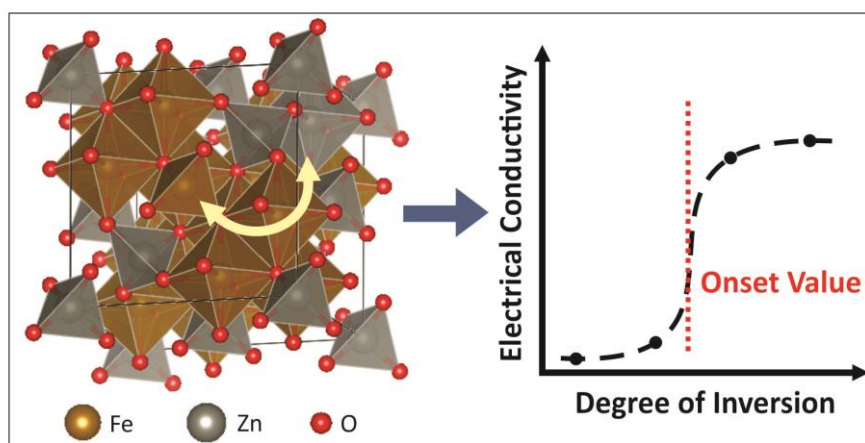
3.3 Introduction

Spinel ferrites (MFe_2O_4, M = metal ion) have proven to be versatile materials due to their magnetic,[1,2] optical,[3] catalytic,[4,5] photocatalytic,[6] and photoelectrochemical[6,7] properties. Along with these properties, a remarkable flexibility concerning the arrangement of the cations in the crystal structure has also been reported.[8] Normal spinel ferrites ($^T[M]^O[Fe_2]O_4$) crystallize in a face-centered cubic oxygen structure with M^{2+} cations occupying tetrahedral (T) sites and Fe^{3+} cations occupying octahedral (O) sites.[9] In a spinel unit cell, 7/8 of the tetrahedral and 1/2 of the octahedral sites remain unoccupied. When all the M^{2+} cations are exchanged by Fe^{3+} cations, the ferrite adopts the so-called inverse structure

(^{T}[Fe]^O[MFe]O$_4$) with M^{2+} cations occupying octahedral sites and Fe^{3+} cations occupying both octahedral and tetrahedral sites in a 1:1 ratio.[10,11] Other configurations between normal and inverse are commonly observed and the degree of inversion, *x,* is the parameter employed to describe them according to ^{T}[M$_{1-x}$Fe$_x$]^O[M$_x$Fe$_{2-x}$]O$_4$, where $0 \le x \le 1$. Among spinel ferrites, zinc ferrite (ZnFe₂O₄, ZFO) is widely studied due to its promising application in photoelectrochemistry as a photoanode material for solar-light-driven water oxidation.[12-16] The thermodynamically most stable configuration of ZFO at 273.15 K and 100 kPa is the normal spinel structure (x = 0).[17] However, several authors have shown that the degree of inversion strongly depends on the synthetic conditions.[17-23] Therefore, the study of the effect of the degree of inversion on physicochemical properties, such as the conductivity, is of utmost importance. The conductivity of a photocatalyst influences the charge carrier mobility and, thus, the charge separation and efficiency.[6,7] Zhu *et al.* have recently reported that ZFO samples with poor crystallinity and a high degree of inversion exhibit a higher efficiency for the photoelectrochemical water oxidation than samples with higher crystallinity and low degree of inversion.[16] Other authors have investigated the influence of the grain size and the synthetic conditions on the electrical properties of ZFO.[24–26] Ponpandian and Narayanasamy reported a decrease in the conductivity by the reduction of the grain size of nanocrystalline ZFO samples prepared by mechanical milling and heat treatment.[26] In disagreement with the results of Ponpandian and Narayanasamy, Shanmugavani *et al.* reported an increase in the conductivity with a reduction of grain size of nanocrystalline ZFO prepared by the combustion method.[24] Singh *et al.* studied the effect of intermediate annealing on the dielectric properties of ZFO samples synthesized by a nitrate route with a constant crystallite size of approximately 40 nm. The authors reported a decrease in the conductivity of the material annealed at higher temperatures.[25] Although it is reported that the degree of inversion generally increases as the grain size decreases,[20-22] it is also well known that particles with similar grain size can also exhibit different degrees of inversion. Therefore, the degree of inversion cannot be directly correlated to the grain size. Consequently, no

conclusions regarding the degree of inversion can be drawn by considering only the grain size.

To the best of our knowledge, a study of the effect of the degree of inversion on the dielectric properties of ZFO without the interference of other parameters such as the crystallite size, crystallinity, or oxygen vacancies content, was missing. In the present work, a systematic analysis of the effect of the degree of inversion on the dielectric properties of ZFO is presented. The crystallinity and crystallite size of the samples, synthesized with differing *x*, were in the same order of magnitude. Thus, the degree of inversion was found to be the only independent variable between the different ZFO samples.

3.4 Results and Discussions

Zinc ferrite (ZFO) pellets with varying degree of inversion were prepared by controlling the annealing temperature of the samples during post-synthetic heat treatment.[23] It is well known for bulk ZFO that the cation relocation is a temperature-dependent reversible process.[17–19] Hence, increasing degrees of inversion were obtained for the ZFO samples by calcination at temperatures ranging from 773 to 1173 K and subsequent quenching in cold water.[23] By two independent methods, *i.e.*, XRD measurements in combination with Rietveld refinement and Mössbauer spectroscopy, degrees of inversion of 0.074, 0.104, 0.134, 0.159, and 0.203 were determined for samples calcined at 773 K, 873 K, 973 K, 1073 K, and 1173 K, respectively. Due to the initial high-temperature calcination steps at 1073 and 1273 K, the crystallinity, crystallite size, and particle size of the different samples were in the same order of magnitude (Table 3.1). The absence of impurities or secondary phases, especially ZnO and γ-Fe$_2$O$_3$, was confirmed by XRD (Fig. B1 in the Supporting Information), Raman spectroscopy, and Mössbauer spectroscopy (Fig. B2). The Mössbauer spectra showed only doublets as expected for ZFO, thus confirming the absence of Fe^{2+} and, consequently, of oxygen vacancies for all the samples.

Furthermore, the elemental analysis revealed a Fe to Zn molar ratio close to 2:1 as expected for ZFO.[23] The values of the Fe to Zn molar ratio, the degree of inversion, the average crystallite size, and the average particle size determined for the ZFO samples calcined at different temperatures are summarized in Table 3.1.

Table 3.1. Calcination temperature, Fe to Zn molar ratio (n_{Fe}/n_{Zn}), degree of inversion x, average crystallite size ($d_{Crystallite}$), and average crystallite size ($d_{Particle}$) of the ZFO samples annealed at different temperatures. The data have been taken from Ref. 23.

Sample	Calcination temperature / K	n_{Fe} / n_{Zn}	Degree of inversion $x^{[a]}$	$d_{Crystallite}/$ nm	$d_{Particle}/$ nm
ZFO_773	773	1.98 ± 0.04	0.074 ± 0.011	306(6)	301 ± 55
ZFO_873	873	1.98 ± 0.05	0.104 ± 0.013	293(5)	300 ± 45
ZFO_973	973	1.97 ± 0.04	0.134 ± 0.008	302(5)	308 ± 28
ZFO_1073	1073	1.98 ±0.03	0.159 ± 0.010	327(6)	299 ± 35
ZFO_1173	1173	1.98 ±0.07	0.203 ± 0.017	283(6)	310 ± 22

[a] Averaged values obtained by Rietveld refinement and Mössbauer spectroscopy.

In order to access information regarding the effect of the degree of inversion on the dielectric properties of the material, impedance spectroscopy was performed. The impedance spectra of polycrystalline samples are normally modeled using equivalent circuits to extract valuable information such as the bulk conductivity or the relative permittivity.[27-29] Thus, a suitable correlation between the physical processes occurring due to the charge transfer through the sample and the elements of the proposed equivalent circuit is fundamental.[30] Table B1 gives an overview of the equivalent circuits used to model impedance spectra of spinel ferrites. Mandal *et al.* have used a simple equivalent circuit consisting of a resistor and a capacitor connected in parallel to fit the impedance spectra of polycrystalline $ZnFe_2O_4$ and

Zn$_{0.5}$Ni$_{0.5}$Fe$_2$O$_4$ samples. The authors related the resistive and capacitive elements to the charge transfer and accumulation, respectively, at the grain boundaries of the materials. The dominating role of the grain boundaries was attributed to the nanometric grain size of the samples.[31] Other authors have used equivalent circuits consisting of a series connection of two R‖C elements to model the charge transfer and accumulation at both, the grain and the grain boundaries of ferrite materials.[26,32-35] As the complexity of the impedance spectra increases, additional elements are normally included in the equivalent circuit to model the measured data. Mekap *et al.* and Syue *et al.* have used an equivalent circuit consisting of three R‖C elements connected in series to model the impedance spectra of ZnFe$_2$O$_4$ and Mn$_x$Zn$_{1-x}$Fe$_2$O$_4$ samples. Two of these R‖C elements were assigned to the charge transfer and accumulation processes at the grain and the grain boundaries while the third R‖C element was used to model the charge transfer and accumulation at the ferrite-electrode interface.[36,37] When the time constants of the R‖C elements forming a series array differ by orders of magnitude, consecutive semicircles are observed in a plot of the negative of the imaginary part of the complex impedance *vs.* the real part (Nyquist plot).[30] However, when the capacitance and the resistance of these elements are approximately in the same order of magnitude, a distorted semicircle is typically observed in a Nyquist plot. Several authors have reported similar equivalent circuits like the ones mentioned above in which some or all of the capacitors have been replaced by constant phase elements (CPEs) in order to properly model distorted semicircles (cf. equivalent circuits IV – VI in Table B1).[38-41] CPEs are widely used to describe the frequency dependence of a non-ideal capacitive behavior in an impedance spectrum.[42-44] However, the use of a CPE remains controversial[45-47] because this element usually does not provide information regarding the physical properties of the system.

In this work, pellets made of ZFO samples having different degrees of inversion were attached in a sandwich configuration between two gold-plated electrodes using graphite conductive adhesive. Impedance measurements were

performed in a N$_2$ atmosphere varying the temperature from 298 K to 448 K in steps of 25 K. The Nyquist plots obtained from the impedance measurements of the samples consisted of distorted semicircles with flattened shapes (Fig. 3.1 and Fig. B7-B11 in the Supporting Information). In order to find a suitable model to fit the obtained results, two boundary conditions were imposed. The first condition was that the proposed equivalent circuit should model the impedance spectra of all the samples, independently of their degree of inversion and the temperature of the samples applied during the impedance measurements. This condition is based on the assumption that the mechanisms of the charge transfer processes occurring in the different ZFO samples are not significantly affected by the cation distribution of the samples and the temperature employed during the measurement. The second constraint was to include no CPE in the proposed equivalent circuit. As was mentioned above, the physical significance of a CPE is still a matter of debate and, therefore, information concerning the charge transfer and accumulation processes occurring in the materials may not be accurately derived from equivalent circuits containing a CPE. Only three of the equivalent circuits given in Table B1 meet this condition. The fitting of a ZFO Nyquist plot by using these three equivalent circuits is shown in the Supporting Information (Fig. B3–B5). As becomes obvious from these graphs, the values calculated for series circuits with up to three R∥C elements do not fit the determined values. The quality of the fits improves as the number of R∥C elements in the series circuit increases. However, even the circuit used by Mekap *et al.* and Syue *et al.* consisting of three R∥C elements connected in series[36,37] does not provide an appropriate fit of the impedance spectra of the ZFO samples (Fig. B5). The experimental data were found to be fitted with sufficient accuracy by employing an equivalent circuit having a series connection of at least four R∥C elements (Fig. 3.1). Fig. 3.2 shows a schematic image of a ZFO electrode used for the measurements together with an illustration of the equivalent circuit applied for the fitting of the impedance spectra.
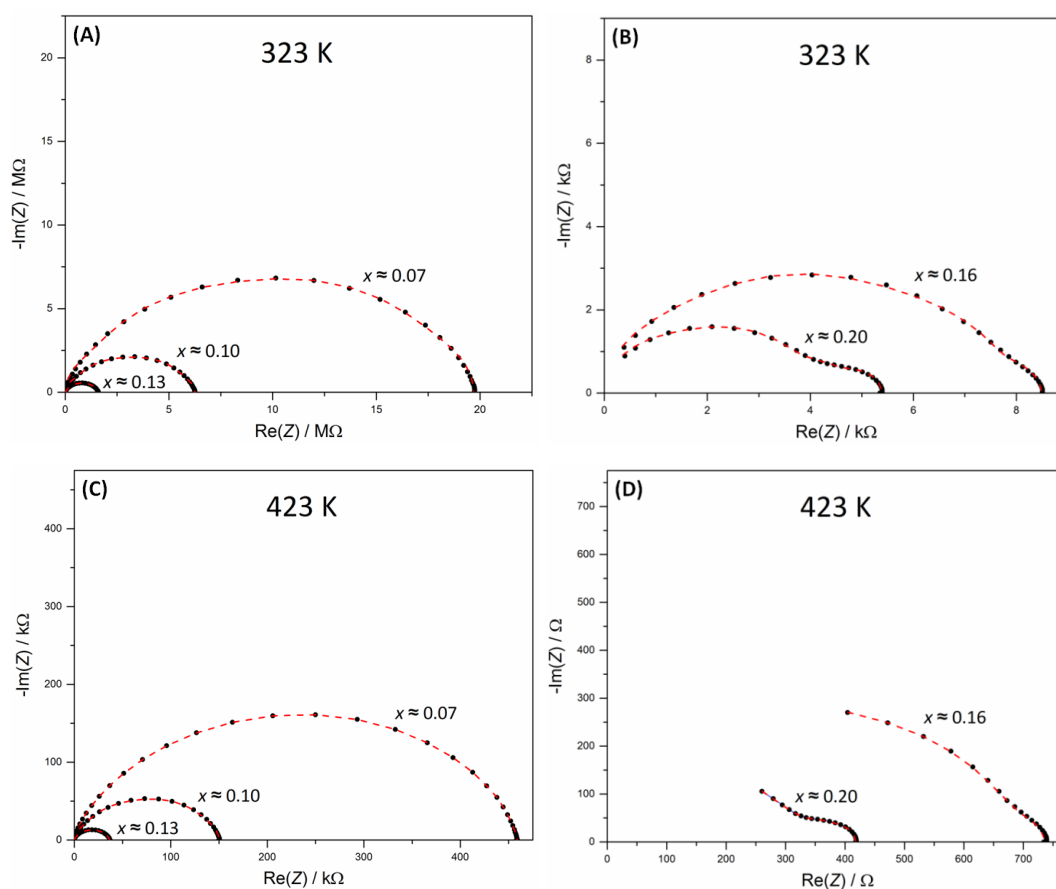
Fig. 3.1. Experimental (black points) and calculated (red dashed line) complex impedance data obtained at **(A-B)** 323 K and **(C-D)** 423 K for the ZFO samples with degree of inversion $x \approx 0.07$, 0.10, 0.13, 0.16, and 0.20. The complex impedance data were simulated with the equivalent circuit shown in Fig. 3.2 employing the EIS Spectrum Analyser software.[48]
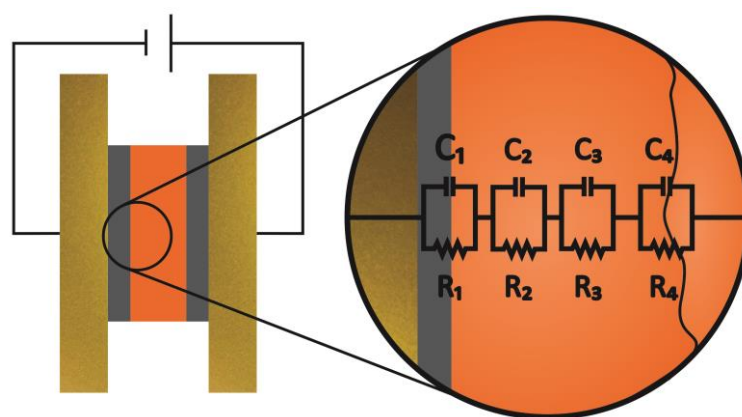
Fig. 3.2. Schematic image of a ZFO pellet attached with a graphite conductive adhesive in a sandwich configuration between two gold-plated electrodes. An equivalent circuit considering the charge transfer and accumulation at the electrode-sample interface, the bulk, and the grain boundaries of the polycrystalline material is schematized as well.

However, the obtained results lack physical meaning as far as the electrical double layer and the charge transfer of the grain, grain boundaries, and electrode-sample interface are unequivocally correlated to capacitive and resistive elements, respectively. It is well known that capacitance associated with the electron transport inside the grains of the material has a lower value than the capacitances associated with transport processes occurring at the grain boundaries and pores.[49] Typical values of the bulk capacitance (C_g) and the grain boundary capacitance are reported to be in the order of 10^{-12} F and 10^{-11}–10^{-8} F, respectively.[49] For the surface layer capacitance and the sample-electrode interface capacitance, larger values up to 10^{-5} F are reported.[49] In this study, capacitance values ranging from 10^{-9} F to 10^{-12} F are calculated for the ZFO samples (Tables B2–B6 in the Supporting Information). With the criterion that the lowest capacitance corresponds to the bulk capacitance,[49-52] C_g is immediately correlated to one of the capacitive elements of the equivalent circuit. After the capacitance value is known, the bulk resistance R_g is deduced. The same method was applied to determine the bulk properties of the ZFO samples at different temperatures. Fig. 3.1(A-D) shows the complex impedance data measured at 323 K and 423 K for the ZFO samples with x ranging from 0.07 to 0.20. The results obtained by fitting the experimental data of all ZFO samples measured from 298 K to 448 K at temperature intervals of 25 K using the described equivalent circuit are presented in the Supporting Information (Fig. B7–B11 and Tables B2–B6). The equivalent circuit shown in Fig. 3.2 considers the charge transfer and accumulation at the electrode-sample interface ($R_1\|C_1$), the bulk ($R_2\|C_2$), and the grain boundaries ($R_4\|C_4$) of the polycrystalline material. The nature of $R_3\|C_3$, which exhibits resistivity and capacitive values similar to those of the bulk resistance and capacitance (Tables B2–B6), is unclear. However, the occurrence of this R‖C element might be assumed to be due to two different reasons. One is the bulk inhomogeneity of the samples due to roughness or porosity, which are normally responsible for the flattened-shape of semicircles observed in Nyquist plots.[42] The second reason is related to the degree of inversion of the ZFO samples. It is well-known that the conduction mechanism in ZFO is the electron hopping between Fe^{3+} cations.[53] This mechanism might be affected if

the Fe^{3+} cations are placed either in tetrahedral or in octahedral sites. Thus, the degree of inversion introduces a structural anisotropy that is properly modeled by the $R_3\|C_3$ element. It is important to stress that, independently of the nature of $R_3\|C_3$, the bulk capacitance and resistance assigned using the criteria mentioned above ($R_2\|C_2$) can be used to extract information concerning the bulk conductivity of the material. Furthermore, due to the similarity between the resistivity and capacitive values of the $R_2\|C_2$ and $R_3\|C_3$ elements, no significant changes in the interpretation of the results are observed by correlating either $R_2\|C_2$ or $R_3\|C_3$ to the bulk electrical properties (Fig. B12 in the Supporting Information).

Relevant information like the bulk conductivity, the activation energy for conduction, or the relative permittivity are derived from R_g, as was reported by Lanfredi and Rodrigues.[30] Shortly, the bulk electrical conductivity σ_B is calculated as:

$$\sigma_B = l/(R_g A) \tag{3.1}$$

where l and A are the thickness and the area of the sample, respectively. Considering that the conductivity is thermally activated and follows an Arrhenius-type law, the activation energy E_A is deduced from the slope of a plot of $\ln(\sigma_B T)$ vs. $1/T$.

$$\sigma_B T = \sigma_0 \exp[-E_A/(kT)] \tag{3.2}$$

$$\ln(\sigma_B T) = \ln \sigma_0 - E_A/(kT) \tag{3.3}$$

where σ_0 (unit different from that of σ_B), k, and T are the pre-exponential factor, the Boltzmann's constant, and the temperature, respectively. The relative permittivity ε_B of the material is determined as:

$$\varepsilon_B = C_B l/(\varepsilon_0 A) \tag{3.4}$$

where ε_0 is the vacuum permittivity and C_B is the bulk capacitance.

The R_g values obtained from the fitting of the complex impedance data were used to calculate the bulk electrical conductivity of the different ZFO samples

according to Eq. 3.1. Table 3.2 and Fig. 3.3A show the results obtained for σ_B at 298 K for the ZFO samples with different degree of inversion. As the degree of inversion increases from 0.074 to 0.134, an increase of the conductivity is observed. However, σ_B remains in the order of the 10^{-9}–10^{-8} S cm^{-1}. Unexpectedly, there is an abrupt increase of two orders of magnitude when the degree of inversion increases from 0.134 to 0.159. The range of conductivity values obtained (10^{-9}–10^{-5} S cm^{-1}) is in good agreement with the values presented by Shanmugavani *et al.* for nanocrystalline ZFO prepared by the combustion method. The authors reported an increase in the conductivity with a reduction of the grain size.[24] It might thus be expected that the decrease in the grain size reported by Shanmugavani *et al.*[24] is accompanied by an increase in the degree of inversion. Nevertheless, the opposite result was presented by Ponpandian and Narayanasamy. These authors reported a decrease in the conductivity with a reduction of grain size of nanocrystalline ZFO samples prepared by mechanical milling and heat treatment.[26] It is well know that the degree of inversion increases and the grain size decreases with increasing milling time.[54,55] However, the crystallinity of the sample decreases as well. The ZFO samples with smallest grain sizes (7 and 13 nm) prepared by Ponpandian and Narayanasamy exhibit not only a very poor crystallinity but also the presence of oxygen vacancies created during the synthetic process.[26] Thus, the degree of inversion of these samples cannot be predicted. The conductivity is affected not only by the particle size or the degree of inversion but also by the oxygen vacancies content and crystallinity of the samples.[56] In a publication discussing the effect of the synthetic conditions on the dielectric properties of ZFO, Singh *et al.* reported an increase in the electrical resistivity (decrease in the conductivity) of approximately 1.4 orders of magnitude as the calcination temperature of a sample with constant crystallite size of 40 nm increases from 1073 K to 1273 K.[25] This result seems to contradict the results reported in the present work. However, it should be considered that Singh *et al.* synthesized the ZFO nanocrystals by a nitrate route.[25] Therefore, a high degree of inversion of at least 0.35 is expected for the samples annealed at low temperatures.[53,57] The thermodynamically predicted degree of inversion for ZFO at 573, 773, 1073, and 1273

K is approximately 0.04, 0.12, 0.16, and 0.22, respectively.[17,18] However, only when the temperature of calcination increases to values higher than 773 K, the cation diffusion becomes rapid enough[17] to significantly change the degree of inversion. Thus, the degree of inversion of the samples calcined at low temperature is kinetically controlled and its value is, consequently, larger as predicted by the thermodynamic equilibrium.[17] As the annealing temperature increases, the cation distribution process becomes thermodynamically controlled and the degree of inversion decreases toward the equilibrium value. Thus, it is expected that the sample annealed at 573 K exhibits the highest degree of inversion and, as the temperature increases, the degree of inversion as well as the conductivity of the samples decreases. In a recent publication, Zhu *et al.* reported conductivities of $89.1 \cdot 10^{-6}$ S cm^{-1} and $12.4 \cdot 10^{-6}$ S cm^{-1} for ZFO nanorods with degrees of inversion of 0.30 and 0.13, respectively.[16] This result is in good agreement with the conductivities measured here for the ZFO samples with a degree of inversion exceeding 0.13.

Table 3.2. Bulk electrical conductivity (σ_B), relative permittivity (ε_B), and activation energy obtained at 298 K for the ZFO samples with increasing degree of inversion.

Sample	Degree of inversion x	Bulk conductivity σ_B at 298 K / S cm^{-1}	Relative permittivity ε_B	Activation energy E$_A$ / eV
ZFO_773	0.074 ± 0.011	$(9.28 \pm 0.31) \cdot 10^{-9}$	4.6 ± 0.2	0.47 ± 0.01
ZFO_873	0.104 ± 0.013	$(2.64 \pm 0.07) \cdot 10^{-8}$	4.3 ± 0.1	0.49 ± 0.01
ZFO_973	0.134 ± 0.008	$(9.88 \pm 0.29) \cdot 10^{-8}$	3.9 ± 0.1	0.46 ± 0.02
ZFO_1073	0.159 ± 0.010	$(1.75 \pm 0.02) \cdot 10^{-5}$	3.1 ± 0.1	0.20 ± 0.03
ZFO_1173	0.203 ± 0.017	$(1.82 \pm 0.02) \cdot 10^{-5}$	3.1 ± 0.1	0.24 ± 0.01

Fig. 3.3B shows the AC conductivity of the ZFO samples at 298 K with increasing degree of inversion as a function of the frequency. The conductance spectra show a frequency-independent behavior at low frequencies. This region corresponds to the bulk conductivity and the extrapolation of the spectra to the limit of zero frequency gives the DC conductivity of the samples. In the high-frequency regime, the conductivity shows a logarithmic increase. This is due to the well-known increment in the electronic exchange of the electron hopping process occurring at

high frequencies.[24] Fig. 3.3C shows plots of $\ln(\sigma_B T)$ as a function of $10^3/T$. Considering a thermally activated conductivity that follows the Arrhenius law (Eq. 3.3), the activation energy is obtained from the slope of the plot presented in Fig. 3.3B.
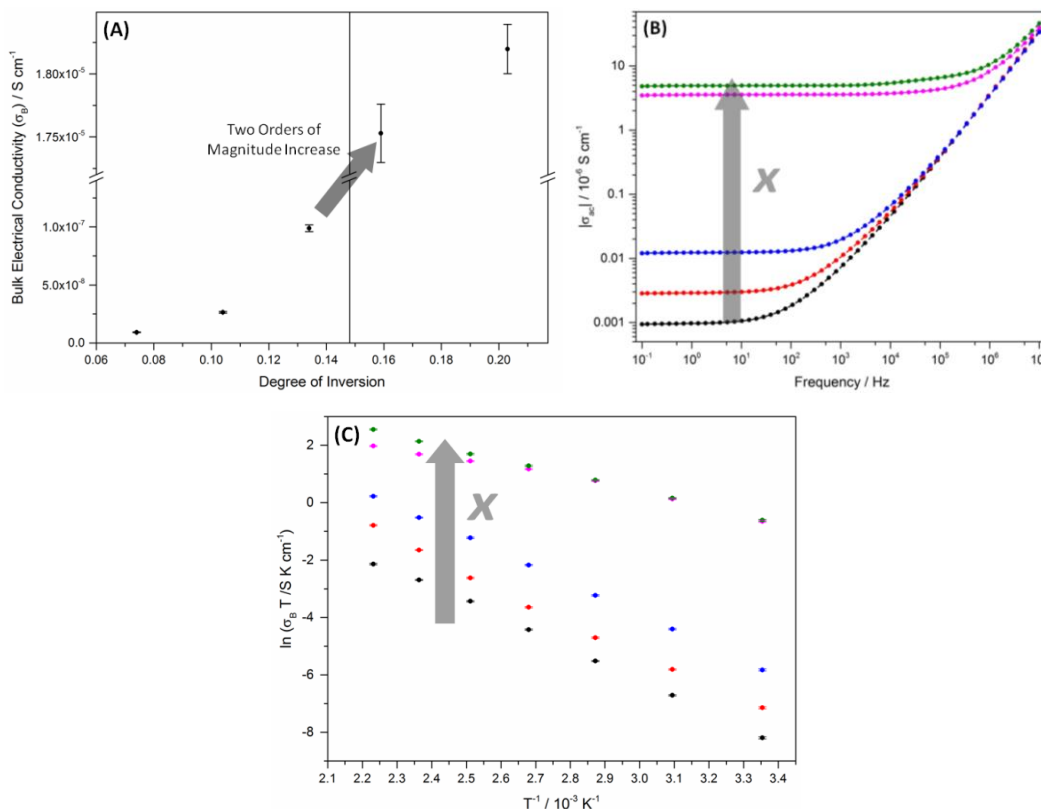
Fig. 3.3. **(A)** Bulk electrical conductivity (σ_B) obtained at 298 K for the ZFO samples as a function of the degree of inversion. **(B)** Module of the AC conductivity measured at 25 °C for the ZFO samples with increasing degree of inversion (grey arrow). **(C)** Plot of $\ln \sigma_B . T$ as a function of $10^3/T$ (Arrhenius plot, Eq. 3.3) for the ZFO samples with increasing degree of inversion (grey arrow). • ZFO_773, $x = 0.074 \pm 0.011$; • ZFO_873, $x = 0.104 \pm 0.013$; • ZFO_973, $x = 0.134 \pm 0.008$; • ZFO_1073, $x = 0.159 \pm 0.010$; • ZFO_1173, $x = 0.203 \pm 0.017$)

As can be seen from Table 3.3, the activation energy decreases to approximately a half of the initial value as the degree of inversion increases from 0.134 to 0.159. Activation energies around 0.45 eV are characteristic of the electron hopping process in Fe^{3+} cations at octahedral sites.[26] Conduction due to oxygen vacancies has an activation energy of approximately 0.93 eV[26] and such a change in the slope of the Arrhenius plot is not observed even in the high temperature regime. This is in agreement with the Mössbauer results that confirmed the absence of Fe^{2+}

and, hence, of oxygen vacancies for all the ZFO samples.[23] The reduction in the
activation energy suggests that the electron hopping becomes favored as the fraction
of Fe^{3+} cations in tetrahedral sites increases. Table 3.3 shows the activation energies
obtained for the ZFO samples with degree of inversion 0.134 and 0.203 together with
values extracted from the literature for a distorted normal (CdFe$_2$O$_4$) and two
distorted inverse (MgFe$_2$O$_4$ and NiFe$_2$O$_4$) spinel ferrites.

Table 3.3. Activation energies of ZnFe$_2$O$_4$ samples with $x \approx 0.07$ to 0.13 and $x \approx 0.16$ to 0.20
obtained in the present work together with activation energies of CdFe$_2$O$_4$, MgFe$_2$O$_4$, and NiFe$_2$O$_4$
extracted from the literature.

Compound	Structure	Activation energy / eV	Reference
ZnFe$_2$O$_4$	Distorted normal ($x \approx 0.074$ - 0.134)	0.46 – 0.49	This work
ZnFe$_2$O$_4$	Distorted normal ($x \approx 0.159$ - 0.203)	0.20 - 0.24	This work
CdFe$_2$O$_4$	Distorted normal[a]	0.46[b]	58
MgFe$_2$O$_4$	Distorted inverse[a]	0.19 - 0.23[b]	59,60
NiFe$_2$O$_4$	Distorted inverse[a]	0.17 – 0.20[b]	61,62

[a] According to Chaumont *et al.*[63], bulk CdFe$_2$O$_4$, MgFe$_2$O$_4$, and NiFe$_2$O$_4$ present degrees of
inversion of around 0.12, 0.92, and 0.94, respectively. [b] These activation energies were
determined with the Arrhenius equation $\sigma_B = \sigma_0 \exp[-E_A/(kT)]$ instead of the modified Arrhenius
equation (Eq. 3.2). However, the difference between both approaches is small.

As can be seen from Table 3.3, the activation energy of ZFO with $x = 0.134$ is
similar to that of CdFe$_2$O$_4$. It is well known that CdFe$_2$O$_4$ has a distorted normal spinel
structure with $x \approx 0.12$[63] and shows a conduction mechanism ruled by the electron
hopping in Fe^{3+} cations placed mainly in octahedral sites.[64] As the distortion of the
ZFO structure increases, *i.e.*, more Fe^{3+} cations are shifted from octahedral to
tetrahedral sites, the activation energy decreases to values similar to that of spinel
ferrites having a distorted inverse structure. The ZFO sample with $x = 0.203$ exhibits
an activation energy similar to that of MgFe$_2$O$_4$ and NiFe$_2$O$_4$.[59-62] Therefore, in
samples with a degree of inversion higher or equal than 0.159, the electron hopping
mechanism becomes remarkably favored by the Fe^{3+} cations placed in tetrahedral

sites. This is in agreement with the first-principles calculations reported by Sun *et al.*[65] The authors showed an insulator behavior for ZFO with a normal ($x = 0$) structure. Nevertheless, the calculations for ZFO structures with $x = 0.25$, $x = 0.50$, and $x = 1$ demonstrated that the density of states near the Fermi energy increases as the degree of inversion increases.[65] This change in the electronic structure might result in a higher conductivity. Another phenomenon affecting the dielectric properties is the superexchange interaction between Fe^{3+} cations present in O^{2-}-sharing octahedral and tetrahedral sites.[65,66] There are no Fe^{3+} cations located at tetrahedral sites in the normal ZFO structure. However, as the degree of inversion increases, Zn^{2+} in the tetrahedral positions are exchanged by Fe^{3+} cations (Fig. 3.4) thus enabling superexchange interactions. It is deduced from the results presented in Table 3.2, that a minimum degree of inversion between 0.13 and 0.16 is necessary for the superexchange interactions to have a considerable impact on the conductivity of ZFO.
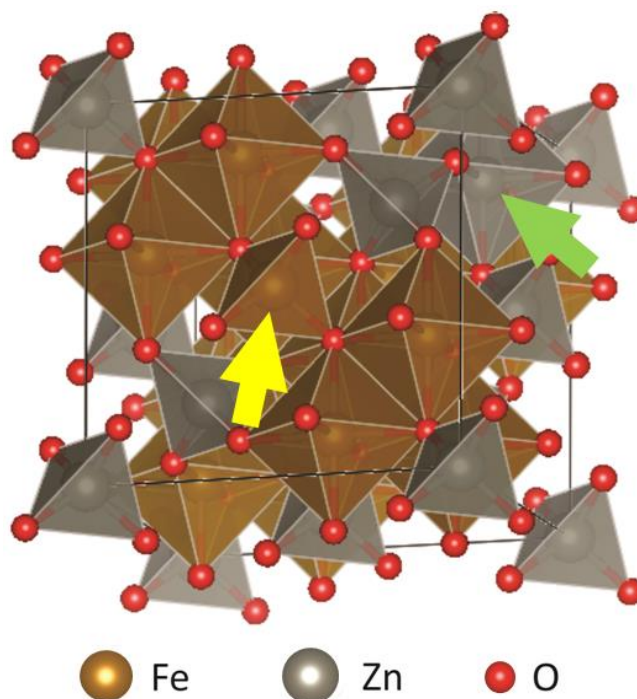
Fig. 3.4. Crystallographic 3D structure of ZFO with a degree of inversion of $x = 0.125$. The Fe^{3+} cation pointed with a yellow arrow is located in a tetrahedral site due to the inversion with a Zn^{2+} cation now located in an octahedral site (green arrow). This partial inversion enables the superexchange interaction between O^{2-}-sharing Fe^{3+} cations located in octahedral and tetrahedral sites. The 3D structure was created with VESTA 3 visualization system.[67]

The photoelectrochemical water oxidation efficiency of a material depends on the synergetic interaction between six major processes: the photon absorption, exciton separation, carrier diffusion, carrier transport, catalytic efficiency, and mass transfer of reactants and products.[68] The electrical conductivity has a large impact on two of these processes, *i.e.*, the carrier diffusion and carrier transport.[68,69] The reason is that the mobility of the charge carriers from the bulk of the material to the surface directly depends on the conductivity.[68] Therefore, an improvement on the carrier diffusion and the carrier transport processes and, thus, on the photoelectrochemical efficiency, are expected as the conductivity of the material increases.[16,69] Since small changes in the degree of inversion of ZFO lead to large changes in the conductivity, the cationic disorder has a major impact on its photoelectrochemical water oxidation efficiency.[16] Hence, the degree of inversion must be taken into consideration when the photoelectrochemical activity of ZFO is investigated.

3.5 Conclusions

A remarkable effect of the cation distribution within the oxygen lattice of spinel zinc ferrite on the electrical conductivity was clearly evidenced by the systematic analysis of samples having degrees of inversion increasing from 0.074 to 0.203. Other factors, such as oxygen vacancies and crystallite size, which are known to affect the electrical conductivity of ZFO, were excluded as the cause of the measured effect. Unexpectedly, the activation energy for the electrical conductivity was found to decrease from 0.46 to 0.20 eV when the degree of inversion exhibits a value between 0.13 and 0.16. As a consequence, the bulk conductivity increases by two orders of magnitude from $9.88 \cdot 10^{-8}$ S cm^{-1} to $1.75 \cdot 10^{-5}$ S cm^{-1}. Due to the partial inversion, the ratio of Fe^{3+} cations located in tetrahedral sites increases and the interaction between O^{2-}-sharing Fe^{3+} cations located in octahedral and tetrahedral sites becomes more pronounced. The electron hopping mechanism might be promoted by this interaction resulting in the observed increase in the conductivity.

From the obtained results, it becomes evident that the conductivity of ZFO is largely degree-of-inversion-dependent. Thus, the degree of inversion of a spinel ferrite should always be determined in order to achieve a significant characterization of the material. The presented results are a step forward to understand the implication of the degree of inversion in the physicochemical properties of ZFO.

3.6 Acknowledgements

3.7 References

(1)   Mathew, D. S.; Juang, R. S. An Overview of the Structure and Magnetism of Spinel Ferrite Nanoparticles and Their Synthesis in Microemulsions. *Chem. Eng. J.* **2007**, *129*, 51–65.

(2)   Van Groenou, A. B.; Bongers, P. F.; Stuyts, A. L. Magnetism, Microstructure and Crystal Chemistry of Spinel Ferrites. *Mater. Sci. Eng.* **1968**, *3*, 317–392.

(3)   Pardavi-Horvath, M. Microwave Applications of Soft Ferrites. *J. Magn. Magn. Mater.* **2000**, *215*, 171–183.

(4)   Lahiri, P.; Sengupta, S. K. Spinel Ferrites as Catalysts: A Study on Catalytic Effect of Coprecipitated Ferrites on Hydrogen Peroxide Decomposition. *Can. J. Chem.* **1991**, *69*, 33–36.

(5)   Albuquerzque, A. S.; Tolentino, M. V. C.; Ardisson, J. D.; Moura, F. C. C.; de Mendonça, R.; Macedo, W. A. A. Nanostructured Ferrites: Structural Analysis and Catalytic Activity. *Ceram. Int.* **2012**, *38*, 2225–2231.

(6)   Dillert, R.; Taffa, D. H.; Wark, M.; Bredow, T.; Bahnemann, D. W. Research Update: Photoelectrochemical Water Splitting and Photocatalytic Hydrogen

Production Using Ferrites (MFe$_2$O$_4$) under Visible Light Irradiation. *APL Mater.* **2015**, *3*, 104001.

(7) Taffa, D. H.; Dillert, R.; Ulpe, A. C.; Bauerfeind, K. C. L.; Bredow, T.; Bahnemann, D. W.; Wark, M. Photoelectrochemical and Theoretical Investigations of Spinel Type Ferrites (M$_x$Fe$_{3-x}$O$_4$) for Water Splitting: A Mini-Review. *J. Photonics Energy* **2016**, *7*, 012009.

(8) O'Neill, H. S. C.; Navrotsky, A. Simple Spinels: Crystallographic Parameters, Cation Radii, Lattice Energies, and Cation Distribution. *Am. Mineral.* **1983**, *68*, 181–194.

(9) McClure, D. S. The Distribution of Transition Metal Cations in Spinels. *J. Phys. Chem. Solids* **1957**, *3*, 311–317.

(10) Callen, H. B.; Harrison, S. E.; Kriessman, C. J. Cation Distributions in Ferrospinels. Theoretical. *Phys. Rev.* **1956**, *103*, 851–856.

(11) Navrotsky, A.; Kleppa, O. J. The Thermodynamics of Cation Distributions in Simple Spinels. *J. Inorg. Nucl. Chem.* **1967**, *29*, 2701–2714.

(12) Kim, J. H.; Jang, Y. J.; Kim, J. H.; Jang, J. W.; Choi, S. H.; Lee, J. S. Defective ZnFe$_2$O$_4$ Nanorods with Oxygen Vacancy for Photoelectrochemical Water Splitting. *Nanoscale* **2015**, *7*, 19144–19151.

(13) Hufnagel, A. G.; Peters, K.; Müller, A.; Scheu, C.; Fattakhova-Rohlfing, D.; Bein, T. Zinc Ferrite Photoanode Nanomorphologies with Favorable Kinetics for Water-Splitting. *Adv. Funct. Mater.* **2016**, *26*, 4435–4443.

(14) Xu, Y. F.; Rao, H. S.; Wang, X. D.; Chen, H. Y.; Kuang, D. Bin; Su, C. Y. In Situ Formation of Zinc Ferrite Modified Al-Doped ZnO Nanowire Arrays for Solar Water Splitting. *J. Mater. Chem. A* **2016**, *4*, 5124–5129.

(15) Peeters, D.; Taffa, D. H.; Kerrigan, M. M.; Ney, A.; Jöns, N.; Rogalla, D.; Cwik, S.; Becker, H. W.; Grafen, M.; Ostendorf, A.; et al. Photoactive Zinc Ferrites Fabricated via Conventional CVD Approach. *ACS Sustain. Chem. Eng.* **2017**, *5*, 2917–2926.

(16) Zhu, X.; Guijarro, N.; Liu, Y.; Schouwink, P.; Wells, R. A.; Le Formal, F.; Sun, S.; Gao, C.; Sivula, K. Spinel Structural Disorder Influences Solar-Water-Splitting Performance of ZnFe$_2$O$_4$ Nanorod Photoanodes. *Adv. Mater.* **2018**, *30*, 1801612.

(17) O'Neill, H. S. C. Temperature Dependence of the Cation Distribution in Zinc

Ferrite (ZnFe$_2$O$_4$) from Powder XRD Structural Refinements. *Eur. J. Miner.* **1992**, *4*, 571–580.

(18)   Pavese, A.; Levy, D.; Hoser, A. H. Cation Distribution in Synthetic Zinc Ferrite (Zn$_{0.97}$Fe$_{2.02}$O$_4$) from in Situ High-Temperature Neutron Powder Diffraction. *Am. Mineral.* **2000**, *85*, 1497–1502.

(19)   Bræstrup, F.; Hauback, B. C.; Hansen, K. K. Temperature Dependence of the Cation Distribution in ZnFe$_2$O$_4$ Measured with High Temperature Neutron Diffraction. *J. Solid State Chem.* **2008**, *181*, 2364–2369.

(20)   Nakashima, S.; Fujita, K.; Tanaka, K.; Hirao, K.; Yamamoto, T.; Tanaka, I. First-Principles XANES Simulations of Spinel Zinc Ferrite with a Disordered Cation Distribution. *Phys. Rev. B* **2007**, *75*, 174443.

(21)   Kamiyama, T.; Haneda, K.; Sato, T.; Ikeda, S.; Asano, H. Cation Distribution in ZnFe$_2$O$_4$ Fine Particles Studied by Neutron Powder Diffraction. *Solid State Commun.* **1992**, *81*, 563–566.

(22)   Akhtar, M. J.; Nadeem, M.; Javaid, S.; Atif, M. Cation Distribution in Nanocrystalline ZnFe$_2$O$_4$ Investigated Using X-Ray Absorption Fine Structure Spectroscopy. *J. Phys. Condens. Matter* **2009**, *21*, 405303.

(23)   Granone, L. I.; Ulpe, A. C.; Robben, L.; Klimke, S.; Jahns, M.; Renz, F.; Gesing, T. M.; Bredow, T.; Dillert, R.; Bahnemann, D. W. Effect of the Degree of Inversion on Optical Properties of Spinel ZnFe$_2$O$_4$. *Phys. Chem. Chem. Phys.* **2018**, *20*, 28267–28278.

(24)   Shanmugavani, A.; Kalai Selvan, R.; Layek, S.; Sanjeeviraja, C. Size Dependent Electrical and Magnetic Properties of ZnFe$_2$O$_4$ Nanoparticles Synthesized by the Combustion Method: Comparison between Aspartic Acid and Glycine as Fuels. *J. Magn. Magn. Mater.* **2014**, *354*, 363–371.

(25)   Singh, J. P.; Chen, C. L.; Dong, C. L.; Srivastava, R. C.; Agrawal, H. M.; Pong, W. F.; Asokan, K. Effect of Intermediate Annealing on the Structural, Electrical and Dielectric Properties of Zinc Ferrite: An XANES Investigation. *Sci. Adv. Mater.* **2013**, *5*, 171–181.

(26)   Ponpandian, N.; Narayanasamy, A. Influence of Grain Size and Structural Changes on the Electrical Properties of Nanocrystalline Zinc Ferrite. *J. Appl. Phys.* **2002**, *92*, 2770–2778.

(27)   Hodge, I. M.; Ingram, M. D.; West, A. R. Impedance and Modulus Spectroscopy

of Polycrystalline Solid Electrolytes. *J. Electroanal. Chem.* **1976**, *74*, 125–143.

(28) Song, H.; Jung, Y.; Lee, K.; Dao, L. H. Electrochemical Impedance Spectroscopy of Porous Electrodes: The Effect of Pore Size Distribution. *Electrochim. Acta* **1999**, *44*, 3513–3519.

(29) Bonanos, N.; Steele, B. C. H.; Butler, E. P. in *Impedance Spectroscopy Theory, Experiment, and Applications (*Macdonald, J. R.; Barsoukov, E.), John Wiley & Sons, **2005**, pp. 205-537.

(30) Lanfredi, S.; Rodrigues, A. C. M. Impedance Spectroscopy Study of the Electrical Conductivity and Dielectric Constant of Polycrystalline LiNbO₃. *J. Appl. Phys.* **1999**, *86*, 2215–2219.

(31) Mandal, S. K.; Singh, S.; Dey, P.; Roy, J. N.; Mandal, P. R.; Nath, T. K. Frequency and Temperature Dependence of Dielectric and Electrical Properties of TFe₂O₄ (T = Ni, Zn, Zn₀.₅Ni₀.₅) Ferrite Nanocrystals. *J. Alloys Compd.* **2016**, *656*, 887–896.

(32) Inaba, H. Impedance Measurement of Single-Crystalline and Polycrystalline Manganese-Zinc Ferrites with Various Non-Stoichiometries. *J. Mater. Sci.* **1997**, *32*, 1867–1872.

(33) Jiang, Y. P.; Li, R.; Tang, X. G.; Liu, Q. X.; Chen, D. G. Dielectric Relaxation Behavior in Co-Precipitation Derived Ferrite (Zn₁₋ₓNiₓ)Fe₂O₄ (0.2 ≤ x ≤ 0.5) Ceramics. *Mod. Phys. Lett. B* **2016**, *30*, 1550277.

(34) Venkatesh, D.; Ramesh, K. V.; Sastry, C. V. S. S. Effect of Sintering Temperature on Micro Structural and Impedance Spectroscopic Properties of Ni₀.₅Zn₀.₅Fe₂O₄ Nano Ferrite. *AIP Conf. Proc.* **2017**, *1859*, 020035.

(35) Chen, D. G.; Tang, X. G.; Liu, Q. X.; Jiang, Y. P.; Ma, C. B.; Li, R. Impedance Response and Dielectric Relaxation in Co-Precipitation Derived Ferrite (Ni,Zn)Fe₂O₄ Ceramics. *J. Appl. Phys.* **2013**, *113*, 214110.

(36) Mekap, A.; Das, P. R.; Choudhary, R. N. P. Dielectric, Magnetic and Electrical Properties of ZnFe₂O₄ Ceramics. *J. Mater. Sci. Mater. Electron.* **2013**, *24*, 4757–4763.

(37) Syue, M.-R.; Wei, F.-J.; Chou, C.-S.; Fu, C.-M. Magnetic, Dielectric, and Complex Impedance Properties of Nanocrystalline Mn-Zn Ferrites Prepared by Novel Combustion Method. *Thin Solid Films* **2011**, *519*, 8303–8306.

(38) Akhtar, M. J.; Younas, M. Structural and Transport Properties of

Nanocrystalline MnFe$_2$O$_4$ Synthesized by Co-Precipitation Method. *Solid State Sci.* **2012**, *14*, 1536–1542.

(39) Pradhan, D. K.; Misra, P.; Puli, V. S.; Sahoo, S.; Pradhan, D. K.; Katiyar, R. S. Studies on Structural, Dielectric, and Transport Properties of Ni$_{0.65}$Zn$_{0.35}$Fe$_2$O$_4$. *J. Appl. Phys.* **2014**, *115*, 243904.

(40) Lazarević, Z. Ž.; Milutinović, A. N.; Jovalekić, Č. D.; Ivanovski, V. N.; Daneu, N.; Madarević, I.; Romčević, N. Ž. Spectroscopy Investigation of Nanostructured Nickel-Zinc Ferrite Obtained by Mechanochemical Synthesis. *Mater. Res. Bull.* **2015**, *9*, 239–247.

(41) Lazarević, Z. Ž.; Jovalekić, Č.; Sekulić, D. L.; Milutinović, A.; Baloš, S.; Slankamenac, M.; Romčević, N. Ž. Structural, Electrical and Dielectric Properties of Spinel Nickel Ferrite Prepared by Soft Mechanochemical Synthesis. *Mater. Res. Bull.* **2013**, *48*, 4368–4378.

(42) Jorcin, J. B.; Orazem, M. E.; Pébère, N.; Tribollet, B. CPE Analysis by Local Electrochemical Impedance Spectroscopy. *Electrochim. Acta* **2006**, *51*, 1473–1479.

(43) Masoud, M.; Heitjans, P. Impedance Spectroscopy Study of Li Ion Dynamics in Single Crystal, Microcrystalline, Nanocrystalline, and Amorphous LiNbO$_3$. *Defect Diffus. Forum* **2005**, *237–240*, 1016–1021.

(44) Amade, R.; Heitjans, P.; Indris, S.; Finger, M.; Haeger, A.; Hesse, D. Defect Formation during High-Energy Ball Milling in TiO$_2$ and Its Relation to the Photocatalytic Activity. *J. Photochem. Photobiol. A Chem.* **2009**, *207*, 231–235.

(45) Shoar Abouzari, M. R.; Berkemeier, F.; Schmitz, G.; Wilmer, D. On the Physical Interpretation of Constant Phase Elements. *Solid State Ionics* **2009**, *180*, 922–927.

(46) Brug, G. J.; van den Eeden, A. L. G.; Sluyters-Rehbach, M.; Sluyters, J. H. The Analysis of Electrode Impedances Complicated by the Presence of a Constant Phase Element. *J. Electroanal. Chem.* **1984**, *176*, 275–295.

(47) Orazem, M. E.; Tribollet, B. in *Electrochemical Impedance Spectroscopy*, 2nd ed.; John Wiley & Sons, New Jersey, **2017**, pp. 395-419.

(48) Bondarenko, A. S.; Ragoisha, G. A. in *Progress in Chemometrics* Research (Ed.: Pomerantsev, A. L.), Nova Science Publishers, New York, **2005**, pp. 89-102.

(49) Irvine, J. T. S.; Sinclair, D. C.; West, A. R. Electroceramics: Characterization by

Impedance Spectroscopy. *Adv. Mater.* **1990**, *2*, 132–138.

(50)   Kolekar, Y. D.; Sanchez, L.; Rubio, E. J.; Ramana, C. V. Grain and Grain Boundary Effects on the Frequency and Temperature Dependent Dielectric Properties of Cobalt Ferrite-Hafnium Composites. *Solid State Commun.* **2014**, *184*, 34–39.

(51)   Sinclair, D. C.; Adams, T. B.; Morrison, F. D.; West, A. R. $CaCu_3Ti_4O_{12}$: One-Step Internal Barrier Layer Capacitor. *Appl. Phys. Lett.* **2002**, *80*, 2153–2155.

(52)   Fleig, J. The Grain Boundary Impedance of Random Microstructures: Numerical Simulations and Implications for the Analysis of Experimental Data. *Solid State Ionics* **2002**, *150*, 181–193.

(53)   Pradeep, A.; Priyadharsini, P.; Chandrasekaran, G. Structural, Magnetic and Electrical Properties of Nanocrystalline Zinc Ferrite. *J. Alloys Compd.* **2011**, *509*, 3917–3923.

(54)   Šepelák, V.; Bergmann, I.; Kipp, S.; Becker, K. D. Nanocrystalline Ferrites Prepared by Mechanical Activation and Mechanosynthesis. *Zeitschrift fur Anorg. und Allg. Chemie* **2005**, *631*, 993–1003.

(55)   Šepelák, V.; Düvel, A.; Wilkening, M.; Becker, K.-D.; Heitjans, P. Mechanochemical Reactions and Syntheses of Oxides. *Chem. Soc. Rev.* **2013**, *42*, 7507–7520.

(56)   Marcu, A.; Yanagida, T.; Nagashima, K.; Tanaka, H.; Kawai, T. Transport Properties of $ZnFe_2O_{4-\delta}$ Thin Films. *J. Appl. Phys.* **2007**, *102*, 023713.

(57)   Roy, M. K.; Haldar, B.; Verma, H. C. Characteristic Length Scales of Nanosize Zinc Ferrite. *Nanotechnology* **2006**, *17*, 232–237.

(58)   Vasanthi, V.; Shanmugavani, A.; Sanjeeviraja, C.; Kalai Selvan, R. Microwave Assisted Combustion Synthesis of $CdFe_2O_4$: Magnetic and Electrical Properties. *J. Magn. Magn. Mater.* **2012**, *324*, 2100–2107.

(59)   El Hiti, M. A. DC Conductivity for $Ni_xMg_{1-x}Fe_2O_4$ Ferrites. *Phase Transitions* **1995**, *54*, 117–122.

(60)   Haque, M. M.; Huq, M.; Hakim, M. A.; Rahman, M. A.; Akther, A. K. M. AC Electrical Conductivity of Ni – Mg Ferrites. *J. Phys. D. Appl. Phys.* **1996**, *29*, 501–505.

(61)   Yang, H.; Zhang, X.; Ao, W.; Qiu, G. Formation of $NiFe_2O_4$ Nanoparticles by Mechanochemical Reaction. *Mater. Res. Bull.* **2004**, *39*, 833–837.

(62) Gunjakar, J. L.; More, A. M.; Gurav, K. V.; Lokhande, C. D. Chemical Synthesis
      of Spinel Nickel Ferrite (NiFe$_2$O$_4$) Nano-Sheets. *Appl. Surf. Sci.* **2008**, *254*, 5844–
      5848.

(63) Chaumont, C.; Burgard, M.; Pasteur, U. L. Normal and Inverse Ferrite Spinels.
      A Set of Solid State Chemistry Related Experiments. *J. Chem. Educ.* **1979**, *56*,
      10–12.

(64) Rezlescu, N.; Rezlescu, E.; Tudorache, F.; Popa, P. D. Gas Sensing Properties of
      Porous Cu-, Cd- and Zn- Ferrites. *Rom. Reports Phys.* **2009**, *61*, 223–234.

(65) Sun, D.; Wang, M. X.; Zhang, Z. H.; Tao, H. L.; He, M.; Song, B.; Li, Q. Effects of
      Inverse Degree on Electronic Structure and Electron Energy-Loss Spectrum in
      Zinc Ferrites. *Solid State Commun.* **2015**, *223*, 12–15.

(66) Šepelák, V.; Tkáčová, K.; Boldyrev, V. V.; Wigmann, S.; Becker, K. D.
      Mechanically Induced Cation Redistribution in ZnFe$_2$O$_4$ and Its Thermal
      Stability. *Phys. B* **1997**, *234–236*, 617–619.

(67) Momma, K.; Izumi, F. VESTA 3 for Three-Dimensional Visualization of Crystal,
      Volumetric and Morphology Data. *J. Appl. Crystallogr.* **2011**, *44*, 1272–1276.

(68) Takanabe, K. Photocatalytic Water Splitting: Quantitative Approaches toward
      Photocatalyst by Design. *ACS Catal.* **2017**, *7*, 8006–8022.

(69) Sivula, K.; Le Formal, F.; Grätzel, M. Solar Water Splitting: Progress Using
      Hematite (α-Fe$_2$O$_3$) Photoelectrodes. *ChemSusChem* **2011**, *4*, 432–449.

Chapter 4

# Effect of the Degree of Inversion on the Photoelectrochemical Activity of Spinel ZnFe$_2$O$_4$

4.1 Foreword

This chapter comprises the manuscript *Effect of the Degree of Inversion on the Photoelectrochemical Activity of Spinel ZnFe$_2$O$_4$* by Luis I. Granone, Konstantin Nikitin, Alexei Emeline, Ralf Dillert, and Detlef W. Bahnemann, published in *Catalysts*, **2019**, 9, 434. In this chapter, the effect of the cation distribution on the electronic properties, as well as the photoelectrochemical activity of ZFO is studied. In the previous section, the large impact observed on the charge carrier transport properties as the degree of inversion increases was assumed to directly affect the photoelectrochemical activity of ZFO. In this chapter these assumptions are confirmed by measuring the photoelectrochemical activity of the ZFO samples having different cation distributions. Furthermore, the electronic properties of the different samples are investigated. Prof. Dr. Alexei Emeline and Konstantin Nikitin (Laboratory "Photoactive Nanocomposite Materials", Saint-Petersburg State University) contributed to this manuscript by performing the Kelvin Probe measurements.

4.2 Abstract

Physicochemical properties of spinel ZnFe$_2$O$_4$ (ZFO) are known to be strongly affected by the distribution of the cations within the oxygen lattice. In this work, the correlation between the degree of inversion, the electronic transitions, the work function, and the photoelectrochemical activity of ZFO was investigated. By room-temperature photoluminescence measurements, three electronic transitions at approximately 625, 547, and 464 nm (1.98, 2.27, and 2.67 eV, respectively) were observed for the samples with different cation distributions. The transitions at 625 and 547 nm were assigned to near-band-edge electron-hole recombination

processes involving O^{2-} $2p$ and Fe^{3+} $3d$ levels. The transition at 464 nm, which has a
longer lifetime, was assigned to the relaxation of the excited states produced after
electron excitations from O^{2-} $2p$ to Zn^{2+} $4s$ levels. Thus, under illumination with
wavelengths shorter than 464 nm, electron-hole pairs are produced in ZFO by two
apparently independent mechanisms. Furthermore, the charge carriers generated by
the O^{2-} $2p$ to Zn^{2+} $4s$ electronic transition at 464 nm were found to have a higher
incident photon-to-current efficiency than the ones generated by the O^{2-} $2p$ to Fe^{3+}
$3d$ electronic transition. As the degree of inversion of ZFO increases, the probability
of a transition involving the Zn^{2+} $4s$ levels increases and the probability of a transition
involving the Fe^{3+} $3d$ levels decreases. This effect contributes to the increase in the
photoelectrochemical efficiency observed for the ZFO photoanodes having a larger
cation distribution.
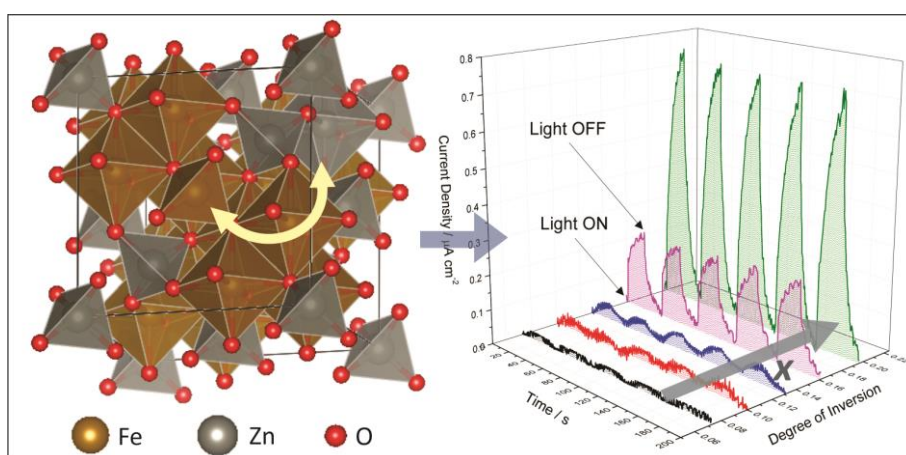
4.3 Introduction

During the last few years, there has been increasing interest in the study of
spinel ZnFe$_2$O$_4$ (ZFO) as a photoanode material for photoelectrochemical water
oxidation.[1-3] As new scientific investigations in this field are reported, differences
concerning the photoelectrochemical activity of ZFO photoanodes prepared by
different routes have become evident.[4-11] It is well known that ZFO exhibits a variable
structure where the distribution of Zn^{2+} and Fe^{3+} cations between octahedral and

tetrahedral sites within the crystal lattice depends on the synthetic conditions.[12-18] Therefore, the reason behind the broad variety of results found in the scientific literature for ZFO photoanodes might be related to the cation distribution. The parameter used to quantify the cation distribution is the degree of inversion, x, which is defined as $^T[Zn_{1-x}Fe_x]^O[Zn_xFe_{2-x}]O_4$ with $0 \leq x \leq 1$ (where the superscripts T and O denote the tetrahedral and octahedral sites, respectively). When $x = 0$ and $x = 1$, ZFO adopts the so-called normal ($^T[Zn]^O[Fe_2]O_4$) and inverse ($^T[Fe]^O[ZnFe]O_4$) structure, respectively. The degree of inversion of bulk ZFO can be controlled by the calcination of the samples at temperatures higher than 737 K and subsequent quenching.[12–15] Thus, bulk ZFO samples with x ranging from approximately 0.02 to 0.20 can be prepared. Pavese et $al.$[13] reported degrees of inversion up to $x \approx 0.34$ at 1600 K for bulk ZFO by in situ high-temperature neutron powder diffraction measurements. Nevertheless, as shown by O'Neill,[12] degrees of inversion higher than $x \approx 0.20$ cannot be experimentally accessed for bulk ZFO samples prepared by means of a solid-state reaction and subsequent quenching. Calcination temperatures higher than 1200 K are required to increase the degree of inversion above this upper limit and, under these conditions, the rate of re-ordering is too fast to quench the sample. For nanoparticulate ZFO, higher degrees of inversion are likely to be obtained,[16–18] and the synthesis of ZFO nanoparticles having an almost completely inverted structure ($x = 0.94$) has been reported.[19]

In a recent publication, Zhu et $al.$[8] reported that the cation distribution in partially reduced ZFO anodes affected the performance of light-induced water oxidation. The authors showed that partially reduced ZFO had a relatively poor crystallinity, but a high degree of inversion exhibited superior photogenerated charge carrier transport when compared to ZFO with a high crystallinity but a low degree of inversion. The research of Zhu et $al.$ pioneered the investigation of the effect of the cation distribution on the photoelectrochemical activity of ZFO. However, a study of the effect of the degree of inversion on the photoelectrochemical activity of pristine

ZFO samples exhibiting uniform particle size, crystallinity, and crystallite size is, to the best of our knowledge, missing.

Recently, we reported the preparation of ZFO by a solid-state reaction and its further processing into pellets with varying degrees of inversion.[14,20] The elemental analysis of the ZFO pellets revealed a Fe to Zn ratio of 2:1 within the limit of the experimental error, as expected for ZFO.[14] The absence of non-reacted α-Fe_2O_3 and ZnO as well as the absence of secondary iron oxide phases, were confirmed by XRD and Raman spectroscopy.[14] Mössbauer spectroscopy confirmed the absence of Fe^{2+} and, hence, of oxygen vacancies for all the ZFO pellets.[14] The crystallite size values deduced from the Rietveld refinements and the particle size distribution obtained from the SEM confirmed that the pellets exhibited similar crystallite and particle sizes independently of the degree of inversion.[14,20] Thus, the degree of inversion was found to be the only independent variable between the different ZFO pellets. These characteristics made it possible to investigate the impact of the degree of inversion on the photoelectrochemical activity of ZFO photoanodes unaffected by other variable parameters such as impurities, the number of oxygen vacancies, the particle size, the crystallite size, and the crystallinity.

In the present work, the photoelectrochemical activity of photoanodes made of pristine ZFO with degrees of inversion increasing from $x \approx 0.07$ to $x \approx 0.20$ is reported. Furthermore, the effect of the cation distribution on electronic properties such as the Fermi level and the electronic structure was investigated for the first time. The electronic structure was studied by means of time-averaged and transient room-temperature photoluminescence spectroscopy. It is well known that the photoluminescence spectrum of a material depends on its particle size, crystallinity, and the presence of point defects.[21,22] Therefore, the crystallinity and crystallite size homogeneity of the synthesized ZFO pellets is of utmost importance in order to access meaningful information concerning the effect of the degree of inversion on the photoluminescence properties. The nature of the observed transitions as well as their lifetime and the impact of the degree of inversion are discussed.

4.4 Results

ZFO pellets with degrees of inversion of $x \approx 0.07$ (ZFO_773), $x \approx 0.10$ (ZFO_873), $x \approx 0.13$ (ZFO_973), $x \approx 0.16$ (ZFO_1073), and $x \approx 0.20$ (ZFO_1173) were prepared by employing a spinel zinc ferrite synthesized by a solid-state reaction as reported previously.[14] In order to access information concerning the porosity of the ZFO pellets, N_2 and Ar physisorption isotherms were measured. Total pore volumes below 10 cm^3 g^{-1} were obtained for all pellets. These values were at the lower limit of quantification, suggesting that the samples did not exhibit a considerable porosity. This is an expected result for dense pellets pressed at high pressure. Other consequences of the low porosity were small BET surface areas below 10 m^2 g^{-1}. The pellets exhibited values ranging from 3.0 to 9.9 m^2 g^{-1} with an average of 5.3 m^2 g^{-1} and no systematic trend concerning the degree of inversion. Thus, independent of the degree of inversion, negligible total pore volumes and sizes were obtained for the different ZFO pellets. The photoelectrochemical activity of the photoanodes was evaluated by measuring the photocurrent for the methanol oxidation reaction. Fig. 4.1A shows the current density – voltage (j-V) curves measured under chopped solar simulated light for the ZFO photoanodes with increasing degrees of inversion. The light was turned on and off at 20 s intervals. Onset photocurrents for the methanol oxidation were observed at an anodic bias potential of around +0.9 V vs. RHE. At a bias potential of +1.2 V vs. RHE, the dark currents were still negligible and the photocurrents were high enough to allow a direct comparison between the different photoanodes. Fig. 4.1B shows the chopped light chronoamperometry measured at an applied bias of +1.2 V vs. RHE. It was observed that the photocurrent for the methanol oxidation increased as the degree of inversion rose from $x \approx 0.07$ to $x \approx 0.20$. The photoanodes with degrees of inversion of $x \approx 0.07$, $x \approx 0.10$, and $x \approx 0.13$ showed current densities below 0.05 μA cm^{-2}. There was a significant increase in the current density from 0.05 to 0.24 μA cm^{-2} as the degree of inversion increased from $x \approx 0.13$ to $x \approx 0.16$. The current density further increased up to 0.77 μA cm^{-2} as the degree of inversion increased from $x \approx 0.16$ to $x \approx 0.20$.
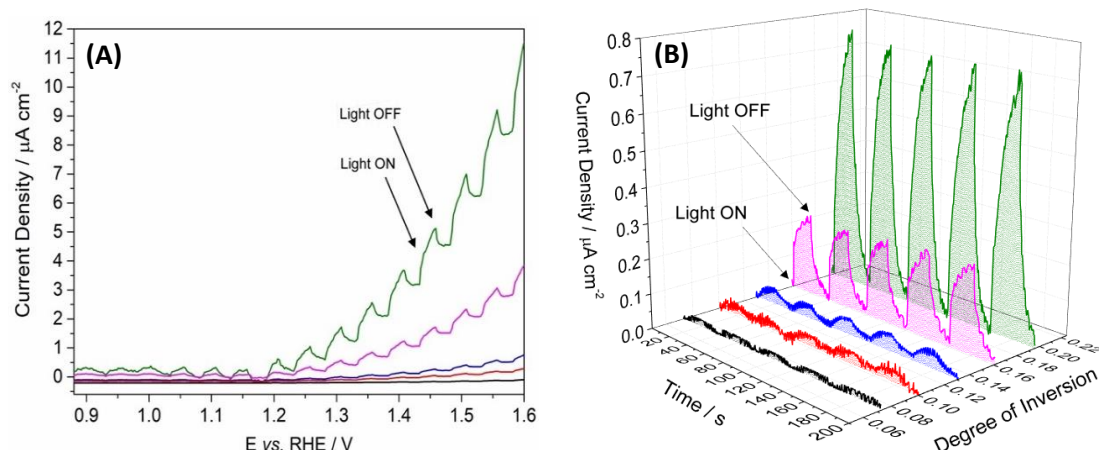
Fig. 4.1. (**A**) Current density – voltage curves for the photoanodes made from ZFO pellets with different degrees of inversion. The measurements were performed in a 50% v/v methanol aqueous solution containing 0.1 mol L^{-1} KNO$_3$ under chopped solar simulator irradiation (intensity output of 680 W m^{-2}). The light was turned on and off at 20 second intervals. (**B**) Chopped light chronoamperometry for the ZFO photoanodes measured with an externally applied bias of +1.2 V vs. RHE. x = 0.074 (ZFO_773); x = 0.104 (ZFO_873); x = 0.134 (ZFO_973); x = 0.159 (ZFO_1073); and x = 0.203 (ZFO_1173).

Fig. 4.2 shows the result of an incident photon-to-current efficiency (IPCE) measurement performed with the ZFO photoanode with a degree of inversion of $x \approx$ 0.20 (ZFO_1173). This photoanode showed the highest photocurrent density for the methanol oxidation (0.77 µA cm^{-2}, Fig. 4.1B). Considering the optical properties of the ZFO_1173 pellet reported previously,[14] the absorbed photon-to-current efficiency (APCE) was calculated. It can be observed from Fig. 4.2 that the APCE and, therefore, the ratio between the number of photogenerated holes reacting with methanol and the number of absorbed photons increased as the wavelength of the incident light became shorter. Thus, the photoanode converts the incident light into an electrical current more efficiently as the energy of the photons emitted by the excitation source increases.
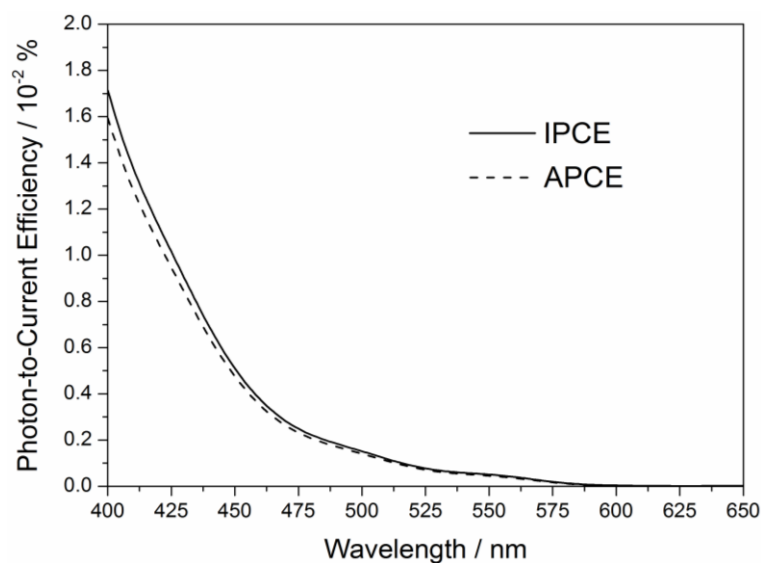
Fig. 4.2. IPCE and APCE of the ZFO photoanode with $x \approx 0.20$ measured under an externally applied bias of +1.2 V vs. RHE in a 50% v/v methanol aqueous solution containing 0.1 mol L^{-1} KNO$_3$. A monochromator was used for fine-tuning the wavelengths of the analyzing light to a final resolution of 1 nm.

Fig. 4.3 shows the work function measured by the Kelvin probe technique for the ZFO pellet samples with different degrees of inversion. It was observed that the work function exhibited values ranging from 5.28 to 5.47 eV. Considering the experimental uncertainty (± 0.13 eV), no significant changes in the Fermi level were observed as the degree of inversion of the ZFO pellets increased.
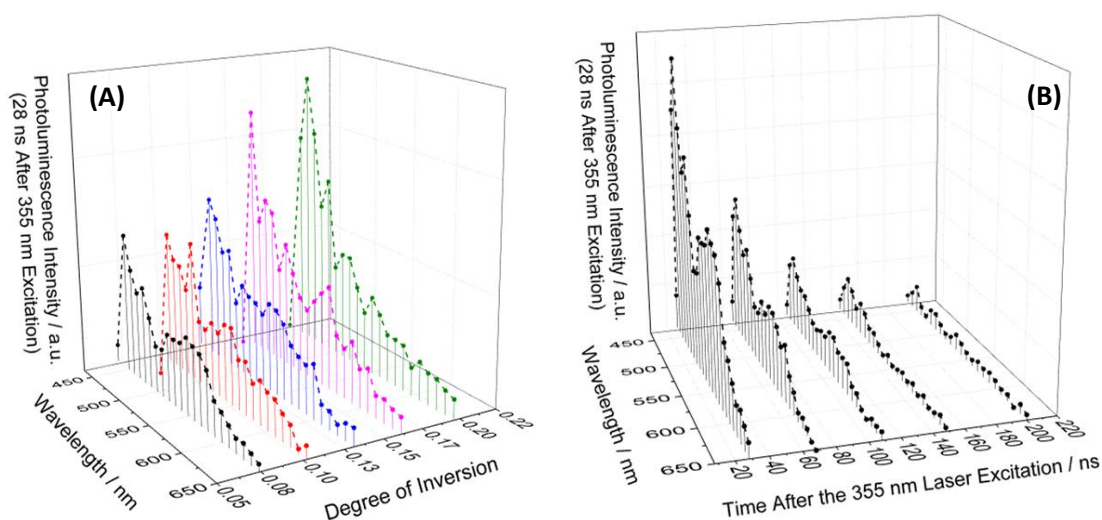
Time-averaged room-temperature photoluminescence measurements were carried out to investigate the effect of the degree of inversion on the electronic structure of ZFO. It becomes obvious from Fig. 4.4 that all pellets exhibited three emission signals at approximately 464, 547, and 625 nm. The relative fluorescence quantum yield of the photoluminescence was determined by using quinine hemisulfate as a standard. Fluorescence quantum yields of 0.05% for the ZFO pellets with degrees of inversion of $x \approx 0.07$, $x \approx 0.10$, and $x \approx 0.13$, 0.04% for the pellet with $x \approx 0.15$, and 0.03% for the pellets with $x \approx 0.20$ were obtained.
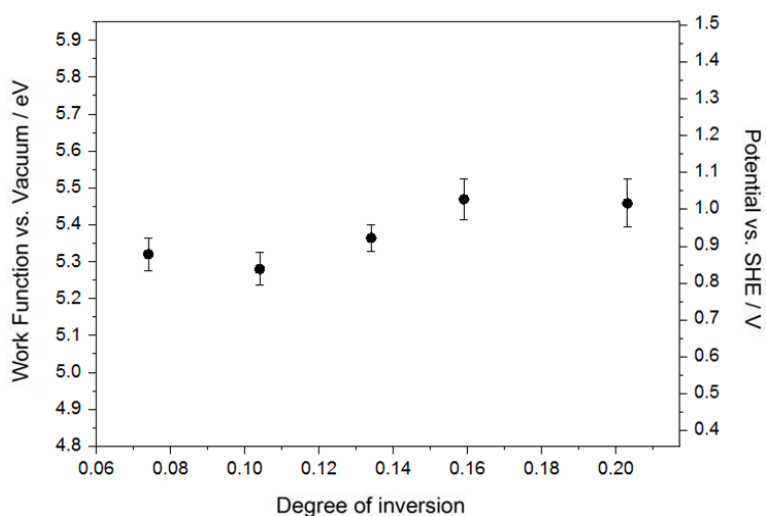
Fig. 4.3. Work function of the ZFO pellet samples with degrees of inversion ranging from $x \approx 0.07$ to $x \approx 0.20$. The values were measured using a scanning Kelvin probe system. Before the measurement, the pellets were calcined at 673 K for 12 h to remove adsorbed water.
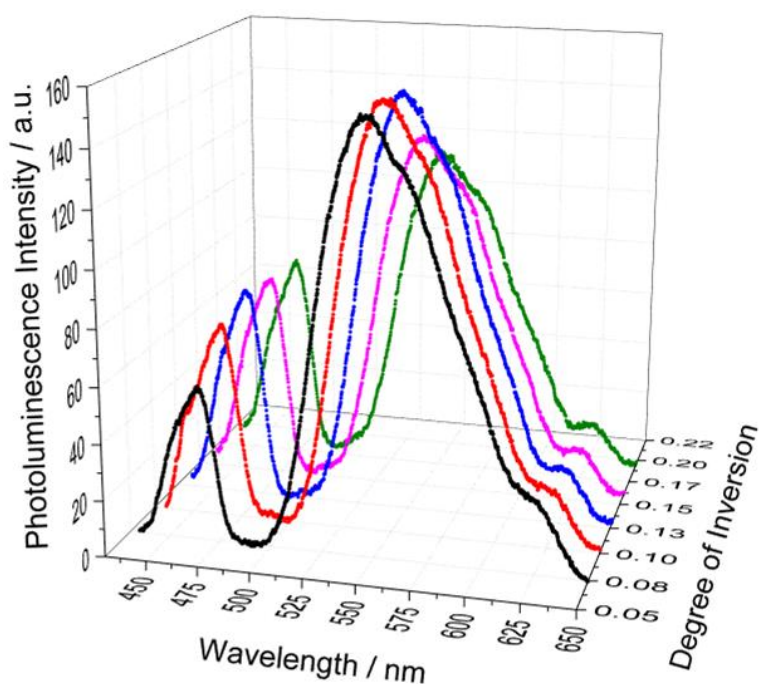
Fig. 4.4. Time-averaged room-temperature photoluminescence of the ZFO pellets as a function of the degree of inversion. An excitation wavelength of 355 nm with an emission slit width of 10 nm was used for the measurement.

Fig. 4.5. (**A**) Transient room-temperature photoluminescence spectra of the ZFO pellets as a function of the degree of inversion. The third harmonic (355 nm) of a Brilliant Nd:YAG laser with a pulse duration of 6 ns was used as the excitation source. The spectra were measured 28 ns after the excitation. x = 0.074 (ZFO_773); x = 0.104 (ZFO_873); x = 0.134 (ZFO_973); x = 0.159 (ZFO_1073); and x = 0.203 (ZFO_1173). (**B**) Transient room-temperature photoluminescence spectra of the ZFO pellet with x = 0.074 (ZFO_773) measured at different points in time after the 355 nm laser excitation.

Transient room-temperature photoluminescence measurements were conducted to study the lifetime of the electronic transitions. Fig. 4.5A shows the photoluminescence spectra of the ZFO pellets with different degrees of inversion measured at 28 ns after the 355 nm laser excitation. Since 10 nm steps were used to record the transient signals, the spectral resolution was lower in comparison to the time-averaged measurements. Thus, the emission observed at approximately 625 nm in the time-averaged photoluminescence measurements (Fig. 4.4) was not detected in the transient measurements. However, the emissions centered at 547 and 464 nm were clearly observed. The emission centered at 464 nm showed a higher intensity than the emission centered at 547 nm. Fig. 4.5B shows the room-temperature photoluminescence spectra of the ZFO pellet with a degree of inversion of x ≈ 0.07 (ZFO_773) measured at different times after the laser excitation. The emission signal centered at 464 nm was weakly observed at 208 ns after the excitation, while the

emission signal centered at 547 nm was no longer observed at 148 ns after the

excitation

4.5 Discussion

A series of ZFO photoanodes with different cation distributions between the

tetrahedral and octahedral sites of the oxygen lattice were investigated to study the

impact of the degree of inversion on the photoelectrochemical activity of ZFO. Due

to the high-temperature calcination steps carried out during the preparation of the

samples, large crystallite sizes of approximately 300 nm were obtained.[14] Large

crystallite sizes imply large diffusion lengths for the photogenerated charge

carriers.[23,24] Consequently, the charge carrier recombination rate increases and the

photoelectrochemical efficiency of the material decreases.[25] Furthermore, low active

surface areas are expected as the crystallite size increases.[23,24] Therefore, the large

crystallite size of the ZFO photoanodes were responsible for the low photocurrent

values obtained for the photoelectrochemical methanol oxidation (Fig. 4.1). The large

thickness of the films (approximately 750 µm) also had a negative impact on the

photoelectrochemical activity for the same reasons above-mentioned. Higher

photocurrent densities are reported in the literature for ZFO photoelectrodes.[4,6,26,27]

In fact, the current benchmark in the performance of a partially reduced ZFO

photoanode for solar water oxidation is 1.0 mA cm^{-2} at 1.23 V.[8] However, the aim of

this work was to understand the impact of the degree of inversion on both the

electronic properties and the photoelectrochemical activity of ZFO. The large particle

size and thickness of the prepared ZFO electrodes as well as the absence of oxygen

vacancies were the main reasons behind the observed low photocurrents. These

drawbacks cannot be avoided when the synthesis of pristine ZFO samples in which

the degree of inversion is the only independent variable is intended. However,

although the measured photocurrents were below 1.0 µA cm^{-2}, an impact of the

degree of inversion on the current density was clearly observed. It becomes obvious

from Fig. 4.1 that an increase of the cation distribution results in an increase in the photoelectrochemical activity of ZFO. The electrical conductivity of the pellets used in the present work was reported in a previous study.[20] An increase in the conductivity from 9.28×10^{-9} to 1.82×10^{-5} S cm^{-1} was observed as the degree of inversion increased from $x \approx 0.07$ to $x \approx 0.20$.[20] Interestingly, a significant increase of two orders of magnitude was observed in the conductivity by increasing the degree of inversion from $x \approx 0.13$ to $x \approx 0.16$. This increase in the conductivity agreed with the large increase in the photocurrent from 0.05 to 0.24 µA cm^{-2} that was observed for methanol oxidation as the degree of inversion increased from $x \approx 0.13$ to $x \approx 0.16$ (Fig. 4.1B). It becomes evident from the preceding discussion that the increase in the electrical conductivity of the pellets with a higher degree of inversion is closely related to the improvement of the photoelectrochemical activity. However, the interrelation between the photoelectrochemical activity and the degree of inversion might also be related to other physicochemical properties of ZFO. Therefore, the impact of the cation distribution on the work function and the electronic transitions of ZFO was investigated.

As mentioned in the previous section, no significant changes in the work function were observed as the degree of inversion of the ZFO pellets increased. In a semiconductor, the work function represents the minimum energy required to remove an electron from the Fermi level into the free space.[28] The work function values obtained for the ZFO pellets corresponded, considering the IUPAC recommended value of −4.44 V for the absolute electrode potential of the hydrogen electrode,[29] to Fermi levels around +0.94 V vs. SHE. Sun *et al.*[5] reported work function values ranging from 5.46 to 5.55 eV (+1.02 and +1.11 V vs. SHE) for mesoporous ZFO nanoparticles obtained via an evaporation-induced self-assembly method and calcined at different temperatures. The results were in good agreement with the values obtained in the present work. The work function of a semiconductor strongly depends on its doping level.[30] As well as for many n-type metal oxide semiconductors,[31] the mechanism for n-type doping of ZFO is the formation of

oxygen vacancies,[32] which results in the reduction of Fe^{3+} to Fe^{2+}.[33] As no Fe^{2+} was
detected by Mössbauer spectroscopy for the ZFO pellets used in this work,[14] a low
donor density was expected. The high work function values obtained and the large
anodic potential necessary for the methanol photoelectrochemical oxidation were
the consequences of the low donor density. Furthermore, as similar work functions
were observed for the different pellets, it was concluded that their donor densities
were in the same order of magnitude and did not depend on the degree of inversion.
For highly doped ZFO samples, work function values between 4.23 and 4.97 eV (−0.21
and +0.53 V vs. SHE) have been reported in the literature.[27,34–36]

The optical band gap and the nature of the optical transitions of the pellets
used for the present work were determined by measuring the diffuse reflectance and
applying the derivation of absorption spectrum fitting (DASF) method, as was shown
in a previous report.[14] Independent of the degree of inversion, the pellets exhibited
an indirect band gap transition at approximately 614 nm (2.02 eV), and a direct band
gap transition at approximately 532 nm (2.33 eV).[14] These values were in good
agreement with the 1.9 and 2.3 eV reported by Guijarro *et al.*[27] for the indirect and
direct band gap, respectively. From density functional theory calculations, Yao *et al.*[37]
showed that the valence band of ZFO consisted of O^{2-} 2*s*, Zn^{2+} 3*d*, Fe^{3+} 3*d*, and O^{2-} 2*p*
states. However, the valence band edge consisted of Fe^{3+} 3*d* and mainly O^{2-} 2*p*
states.[37] The conduction band edge consisted of O^{2-} 2*p* and mainly Fe^{3+} 3*d* states.[37]
At higher energies, the contribution from the Zn^{2+} 4*s* states was observed in the
density of states. Lv *et al.*[38] claimed that the energy band structures of ZFO were
defined by considering the O^{2-} 2*p* levels as the valence band edge and the Fe^{3+} 3*d*
levels as the conduction band edge. The emissions observed in Fig. 4.4 at
approximately 547 and 625 nm were in reasonable agreement with the direct and
indirect band gap transitions at 532 and 614 nm, respectively.[14] Thus, these bands
were ascribed to near-band-edge emissions due to the electron relaxation from Fe^{3+}
3*d* levels located in the conduction band edge to O^{2-} 2*p* levels in the valence band
edge.[39,40] The emission centered at 464 nm might be related to transitions involving

the Zn^{2+} cations.[41,42] It is well known for Fe-doped ZnO that the near-band-edge emission of ZnO centered at approximately 379 nm becomes red-shifted as the amount of Fe increases.[42,43] If the amount of Fe is high enough and spinel ZFO is formed as a secondary phase, a new emission centered at 464 nm is observed.[42] Therefore, the transition observed at approximately 464 nm could be ascribed to the electron relaxation from Zn^{2+} 4s levels within the conduction band to O^{2-} 2p in the valence band edge. This assignment agrees with the density of states presented by Yao *et al.*[37] Regardless of the nature of the electronic transitions, it is important to stress that the conduction band of ZFO does not exhibit a continuous density of empty electronic energetic states. Contradicting the semiconductor band theory,[44] the conduction band of photoexcited electrons were delocalized in confined densities of states involving either Fe^{3+} 3d levels or Zn^{2+} 4s levels. Whether the photoexcited electron is delocalized in Fe^{3+} 3d levels or Zn^{2+} 4s levels depends on the energy of the excitation source. A scheme of the electronic excitation mechanism of ZFO is shown in Fig. 4.6.
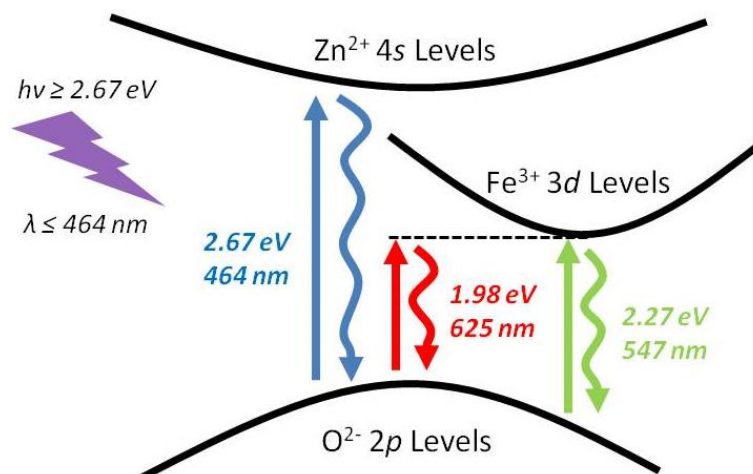
Fig. 4.6. Scheme of the electronic transitions observed for ZFO when photons with wavelengths shorter than 464 nm (energy higher than 2.67 eV) are used for the excitation.

The influence of the O^{2-} 2p to Fe^{3+} 3d (indirect and direct) and the O^{2-} 2p to Zn^{2+} 4s electronic transitions on the photoelectrochemical efficiency of ZFO was deduced from the APCE measurement. According to Fig. 4.2, when the ZFO photoanode is irradiated with light at wavelengths longer than 600 nm, the APCE is

approximately zero. Thus, the methanol oxidation efficiency of the charge carriers generated via the indirect O^{2-} $2p$ to Fe^{3+} $3d$ transition (625 nm) is negligible. As also reported by Guijarro et al.,[27] the indirect transition of ZFO does not effectively drive photoelectrochemical processes. The APCE increases as wavelengths ranging from 475 to 600 nm are used for the excitation of the photoanode. Under these irradiation conditions, the direct O^{2-} $2p$ to Fe^{3+} $3d$ transition occurs and the generated charge carriers can convert the incident light into an electrical current. Interestingly, a significant increase in the APCE values can be observed when the photoanode is irradiated with light at wavelengths shorter than 475 nm. This phenomenon could be attributed to two reasons. One is the increase in the absorptivity of the material as is observed from the diffuse reflectance measurements of the ZFO pellets reported elsewhere.[14] The second reason is the contribution of the charge carriers generated by the electronic transition from O^{2-} $2p$ to Zn^{2+} $4s$ levels (464 nm). The absorption coefficient of ZFO has approximately the same magnitude for wavelengths ranging from 400 to 500 nm.[45,46] Hence, the significant increase in the APCE should be observed at wavelengths longer than 475 nm if the larger light absorption of the material is responsible for this effect. Therefore, the increase in the APCE values at wavelengths shorter than 475 nm must be mainly due to the contribution to the methanol photooxidation of the charge carriers generated via the O^{2-} $2p$ to Zn^{2+} $4s$ electronic transition (464 nm).

The data presented in Fig. 4.4 revealed that the degree of inversion affected the relative intensity of the room-temperature photoluminescence bands of ZFO. As the cation disorder increased, the intensity of the near-band-edge emission centered at 547 nm decreased, and the intensity of the emission centered at 464 nm increased. These emission bands were the result of electron-hole recombination processes and, thus, it is reasonable to assume that the observed increase or decrease in the emission intensity is due to an increase or decrease, respectively, in the number of generated electron-hole pairs. Therefore, as Zn^{2+} cations located in tetrahedral sites are interchanged by Fe^{3+} cations from octahedral sites, the probability of the

electronic transition at 464 nm (from O^{2-} 2p to Zn^{2+} 4s levels) increases and the probability of the near-band-edge electronic transitions (from O^{2-} 2p to Fe^{3+} 3d levels) decreases. From the time-averaged photoluminescence measurements, it was observed that the intensity of the emission centered at 547 nm was higher than that of the emission centered at 464 nm (Fig. 4.4). However, transient photoluminescence measurements showed a higher intensity for the emission centered at 464 nm (Fig. 4.5A). This can be explained by a faster decay of the emission centered at 547 nm. In fact, the signal centered at 547 nm was no longer observed at 148 ns after the excitation while the signal centered at 464 nm (due to the relaxation of the O^{2-} 2p to Zn^{2+} 4s electron excitation) was observed even 208 ns after the excitation (Fig. 4.5B).

As discussed above, the electron-hole pairs generated by the electronic transitions observed at 547 and 464 nm are involved in the photoelectrochemical process occurring at the ZFO electrodes. It was shown that the transition centered at 464 nm had a higher efficiency for photoelectrochemical methanol oxidation than the transition centered at 547 nm (Fig. 4.2). However, the valence band holes generated via both transitions had the same redox potential and, therefore, the same oxidizing activity. The higher efficiency of the transition centered at 464 nm was due to the longer lifetime of the generated charge carriers (Fig. 4.5B). As the degree of inversion of the ZFO pellets increased, both, the amount of O^{2-} 2p to Zn^{2+} 4s electronic transitions and the photoelectrochemical activity increased.

4.6 Materials and Methods

Polycrystalline ZFO samples with degrees of inversion increasing from $x \approx 0.07$ to $x \approx 0.20$ were synthesized by means of a solid-state reaction as reported previously.[14] Briefly, stoichiometric amounts of ZnO (60 mmoles, Sigma Aldrich, Taufkirchen, Germany, ≥ 99.0%) and α-Fe$_2$O$_3$ (60 mmoles, Sigma Aldrich, Taufkirchen, Germany, ≥99.0%) powders were ground in an agate mortar. The mixture was calcined in air at 1073 K for 12 h, cooled down to room temperature, and ground

once again. Aliquots of 0.500 g were pressed into 13 mm diameter pellets applying a pressure of 55 MPa. The pellets were calcined at 1273 K for 2 h, cooled down to 1073 K and kept at this temperature for 12 h, then cooled down to 773 K and kept at this temperature for 50 h, and finally quenched in cold water. Some of the pellets (referred as ZFO_773) were separated and the rest were divided into four sets of pellets. These pellets were heated up with a rate of 300 K h^{-1} and calcined at 873, 973, 1073, and 1173 K for 25, 20, 12, and 10 h, respectively. As reported by O'Neill,[12] these calcination times were sufficiently long for the ZFO pellets to reach a steady-state value of the degree of inversion. After this period of time, the calcined pellets were immediately quenched in cold water. These pellets are referred as ZFO_873, ZFO_973, ZFO_1073, and ZFO_1173. The ZFO pellets were sanded with Al$_2$O$_3$ sandpaper (KK114F, grit size P320, VSM Abrasives, Hannover, Germany) to a final thickness of 0.75 mm ± 0.02 mm.

Molecular nitrogen physisorption isotherms were measured at 77 K on a Quantachrome Autosorb-3MP instrument and argon physisorption isotherms were measured at 87 K on a Quantachrome Autosorb-1 instrument (3P Instruments GmbH & Co. KG, Odelzhausen, Germany). The pellets were outgassed in vacuum at 423 K for 24 h prior to the sorption measurements. Surface areas were estimated by applying the Brunauer–Emmett–Teller (BET) equation[47] and the total pore volumes were estimated by the single-point method at p/p_0 = 0.95.

Electrochemical and photoelectrochemical measurements were performed by employing a ZENNIUM Electrochemical Workstation (Zahner Scientific Instruments, Kronach, Germany) equipped with a three-electrode electrochemical cell with a Pt counter electrode and an Ag/AgCl/NaCl (3 mol kg^{-1}) reference electrode. ZFO working electrodes were prepared by attaching a copper wire with silver paint (Ferro GmbH, Frankfurt am Main, Germany) and conductive epoxy (Chemtronics, Kennesaw, GA, USA) to one face of the pellet sample. Photoelectrochemical measurements were performed in a 50% v/v methanol aqueous solution containing 0.1 mol L^{-1} KNO$_3$. A solar simulator (LOT-Quantum Design GmbH, Darmstadt,

Germany) consisting of a 300 W xenon-arc lamp provided with an AM 1.5-global filter was used as the irradiation source. An intensity output of 680 W m^{-2} at the position of the working electrode was measured using a SpectraRad Xpress spectral irradiance meter (B&W Tek, Newark, DE, USA). For the IPCE measurements, a TLS03 tunable light source (Zahner Scientific Instruments, Kronach, Germany) consisting of an array of monochromatic LEDs with emission wavelengths ranging from 400 to 650 nm was used. A monochromator was employed for fine tuning the wavelengths to a final resolution of 1 nm.

A scheme of the set-up used for the transient photoluminescence spectroscopy is shown in Fig. 4.7. The third harmonic (355 nm) of a Brilliant Nd:YAG laser (Quantel, Lannion, France) with a pulse duration of 6 ns was used as the excitation source. A laser intensity of 3.0 mJ per pulse was selected for the measurements. The intensity of the laser was measured using a Maestro laser power meter (Gentec-EO, Québec, Canada). The angle of the laser beam path was adjusted by rotating a Pellin-Broca prism beam steering module. The illumination area of the laser beam was approximately 0.5 cm^2. The light emitted by the pellets after the laser excitation was collected by a Spectrosil lens and directed toward the monochromator by a folding mirror. The monochromator was connected with a PMT R928 photomultiplier detector (Hamamatsu Photonics, Hamamatsu, Japan). To avoid the overloading of the photomultiplier, a 370 nm cut off filter was introduced in front of the monochromator entrance. For the transient photoluminescence measurements, a constant voltage of 700 V was applied to the photomultiplier.
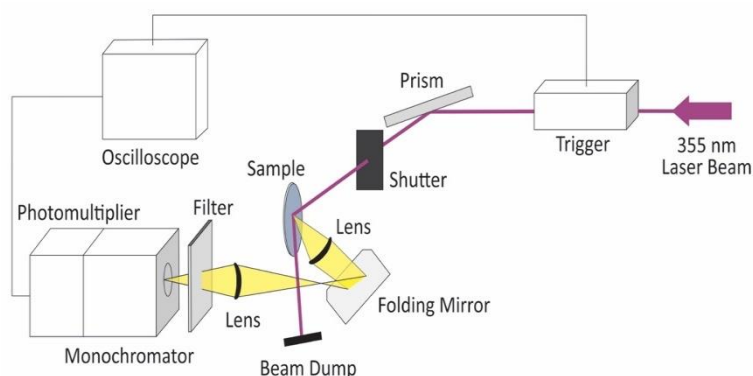
Fig. 4.7. Scheme of the diffuse reflectance setup used for the transient photoluminescence measurements. The 355 nm laser excitation is shown in violet and the radiation emitted by the ZFO pellet is represented in yellow.

Time-averaged photoluminescence measurements were performed in an F-7100 fluorescence spectrophotometer (Hitachi, Tokyo, Japan). A wavelength of 355 nm was selected as the excitation source and the photoluminescence spectra were measured from 440 to 650 nm with a 240 nm min^{-1} scan rate. Excitation and emission slit widths of 10 nm were used. The relative fluorescence quantum yield was determined by employing a reported standard method.[48–50] Briefly, a 5×10^{-3} mol L^{-1} solution of quinine hemisulfate monohydrate ($C_{20}H_{24}N_2O_2 \cdot 0.5H_2SO_4 \cdot H_2O$, Sigma Aldrich, Taufkirchen, Germany, ≥ 98.0%) in 1 N H$_2$SO$_4$, with an absolute quantum yield efficiency of 0.51 at 25 °C,[48] was used to determine the relative photoluminescence quantum yield of the ZFO pellets. For the time-averaged and the transient photoluminescence measurements, suspensions of the ZFO pellets were prepared. ZFO pellets were ground in an agate mortar and dispersed in deionized water by a one-hour ultrasound treatment (340 W L^{-1}). A concentration of 2.5 g L^{-1} was used for the measurements.

Work function measurements were performed with a scanning Kelvin probe system SKP5050 (KP Technology, Wick, Scotland) versus a gold reference probe electrode (probe area of 2 mm^2). The probe oscillation frequency was 74 Hz, and the backing potential was 7000 mV. Work function values were obtained by averaging 1000 data points for two different sites of each pellet. Prior to the measurements,

the pellets were heated at 673 K for 12 h to remove adsorbed water. The cation diffusion process in ZFO is kinetically hindered at temperatures lower than 773 K.[12] Thus, the degree of inversion of the pellets did not change during the heat treatment.

4.7 Conclusions

The effect of the degree of inversion on the photoelectrochemical activity of ZFO was investigated. As the cation distribution changed from $x \approx 0.07$ to $x \approx 0.20$, the photoelectrochemical activity of ZFO increased. In order to study the correlation between this phenomenon and the electronic properties of the material, the work function as well as the time-averaged and transient photoluminescence of the different ZFO samples were studied. No significant effect of the degree of inversion on the Fermi level was observed. Regarding the photoluminescence results, the characteristic near-band-edge emissions (547 and 625 nm for the direct and indirect transition, respectively) due to the electron-hole recombination involving Fe^{3+} $3d$ and O^{2-} $2p$ levels were observed. Furthermore, an emission of energy higher than the band gap was also detected. This emission was assigned to the relaxation of the excited state produced after the electronic transition from O^{2-} $2p$ to Zn^{2+} $4s$ levels (464 nm). Interestingly, the lifetime of the latter emission was observed to be longer than the lifetime of the near-band-edge emission. After excitation with photons with wavelengths shorter than 464 nm (blue and violet region of the visible light spectrum), electron-hole pairs were produced in ZFO by two apparently independent mechanisms (Fig. 4.6). One pathway was the excitation of electrons from O^{2-} $2p$ levels at the valence band maximum to Fe^{3+} $3d$ levels at the conduction band minimum. The other was the excitation of electrons from O^{2-} $2p$ levels at the valence band maximum to Zn^{2+} $4s$ levels located within the conduction band. The charge carriers generated by the latter mechanism showed a longer lifetime and, consequently, a higher efficiency for the photoelectrochemical methanol oxidation. As the degree of

inversion of ZFO increased, the transition involving the Zn^{2+} 4s levels was favored, thus contributing to the observed increase in the photoelectrochemical activity.

4.8 Acknowledgements

4.9 References

(1)   Dillert, R.; Taffa, D. H.; Wark, M.; Bredow, T.; Bahnemann, D. W. Research Update: Photoelectrochemical Water Splitting and Photocatalytic Hydrogen Production Using Ferrites (MFe$_2$O$_4$) under Visible Light Irradiation. *APL Mater.* **2015**, *3*, 104001.

(2)   Taffa, D. H.; Dillert, R.; Ulpe, A. C.; Bauerfeind, K. C. L.; Bredow, T.; Bahnemann, D. W.; Wark, M. Photoelectrochemical and Theoretical Investigations of Spinel Type Ferrites (M$_x$Fe$_{3-x}$O$_4$) for Water Splitting: A Mini-Review. *J. Photonics Energy* **2016**, *7*, 012009.

(3)   Chandrasekaran, S.; Bowen, C.; Zhang, P.; Li, Z.; Yuan, Q.; Ren, X.; Deng, L. Spinel Photocatalysts for Environmental Remediation, Hydrogen Generation, CO$_2$ Reduction and Photoelectrochemical Water Splitting. *J. Mater. Chem. A* **2018**, *6*, 11078–11104.

(4)   Kim, J. H.; Jang, Y. J.; Kim, J. H.; Jang, J. W.; Choi, S. H.; Lee, J. S. Defective ZnFe$_2$O$_4$ Nanorods with Oxygen Vacancy for Photoelectrochemical Water Splitting. *Nanoscale* **2015**, *7*, 19144–19151.

(5)   Sun, M.; Chen, Y.; Tian, G.; Wu, A.; Yan, H.; Fu, H. Stable Mesoporous ZnFe$_2$O$_4$ as an Efficient Electrocatalyst for Hydrogen Evolution Reaction. *Electrochim. Acta* **2016**, *190*, 186–192.

(6)   Hufnagel, A. G.; Peters, K.; Müller, A.; Scheu, C.; Fattakhova-Rohlfing, D.; Bein,

T. Zinc Ferrite Photoanode Nanomorphologies with Favorable Kinetics for Water-Splitting. *Adv. Funct. Mater.* **2016**, *26*, 4435–4443.

(7)   Peeters, D.; Taffa, D. H.; Kerrigan, M. M.; Ney, A.; Jöns, N.; Rogalla, D.; Cwik, S.; Becker, H. W.; Grafen, M.; Ostendorf, A.; et al. Photoactive Zinc Ferrites Fabricated via Conventional CVD Approach. *ACS Sustain. Chem. Eng.* **2017**, *5*, 2917–2926.

(8)   Zhu, X.; Guijarro, N.; Liu, Y.; Schouwink, P.; Wells, R. A.; Le Formal, F.; Sun, S.; Gao, C.; Sivula, K. Spinel Structural Disorder Influences Solar-Water-Splitting Performance of ZnFe$_2$O$_4$ Nanorod Photoanodes. *Adv. Mater.* **2018**, *30*, 1801612.

(9)   Kirchberg, K.; Wang, S.; Wang, L.; Marschall, R. Mesoporous ZnFe$_2$O$_4$ Photoanodes with Template-tailored Mesopores and Temperature-Dependent Photocurrents. *ChemPhysChem* **2018**, *19*, 2313–2320.

(10)   Kim, J.H.; Jang, Y.J.; Choi, S.H.; Lee, B.J.; Kim, J.H.; Park, Y. Bin; Nam, C.M.; Kim, H.G.; Lee, J.S. A Multitude of Modifications Strategy of ZnFe$_2$O$_4$ Nanorod Photoanodes for Enhanced Photoelectrochemical Water Splitting Activity. *J. Mater. Chem. A* **2018**, *6*, 12693–12700.

(11)   Guo, Y.; Zhang, N.; Wang, X.; Qian, Q.; Zhang, S.; Li, Z.; Zou, Z. A Facile Spray Pyrolysis Method to Prepare Ti-Doped ZnFe$_2$O$_4$ for Boosting Photoelectrochemical Water Splitting. *J. Mater. Chem. A* **2017**, *5*, 7571–7577.

(12)   O'Neill, H. S. C. Temperature Dependence of the Cation Distribution in Zinc Ferrite (ZnFe$_2$O$_4$) from Powder XRD Structural Refinements. *Eur. J. Miner.* **1992**, *4*, 571–580.

(13)   Pavese, A.; Levy, D.; Hoser, A. H. Cation Distribution in Synthetic Zinc Ferrite (Zn$_{0.97}$Fe$_{2.02}$O$_4$) from in Situ High-Temperature Neutron Powder Diffraction. *Am. Mineral.* **2000**, *85*, 1497–1502.

(14)   Granone, L. I.; Ulpe, A. C.; Robben, L.; Klimke, S.; Jahns, M.; Renz, F.; Gesing, T. M.; Bredow, T.; Dillert, R.; Bahnemann, D. W. Effect of the Degree of Inversion on Optical Properties of Spinel ZnFe$_2$O$_4$. *Phys. Chem. Chem. Phys.* **2018**, *20*, 28267–28278.

(15)   Bræstrup, F.; Hauback, B. C.; Hansen, K. K. Temperature Dependence of the Cation Distribution in ZnFe$_2$O$_4$ Measured with High Temperature Neutron Diffraction. *J. Solid State Chem.* **2008**, *181*, 2364–2369.

(16)   Akhtar, M. J.; Nadeem, M.; Javaid, S.; Atif, M. Cation Distribution in Nanocrystalline $ZnFe_2O_4$ Investigated Using X-Ray Absorption Fine Structure Spectroscopy. *J. Phys. Condens. Matter* **2009**, *21*, 405303.

(17)   Kumar, G. S. Y.; Naik, H. S. B.; Roy, A. S.; Harish, K. N.; Viswanath, R. Synthesis, Optical and Electrical Properties of $ZnFe_2O_4$ Nanocomposites. *Nanomater. Nanotechnol.* **2012**, *2*, 19:2012.

(18)   Nakashima, S.; Fujita, K.; Tanaka, K.; Hirao, K.; Yamamoto, T.; Tanaka, I. First-Principles XANES Simulations of Spinel Zinc Ferrite with a Disordered Cation Distribution. *Phys. Rev. B* **2007**, *75*, 174443.

(19)   Šepelák, V.; Tkáčová, K.; Boldyrev, V. V.; Wigmann, S.; Becker, K. D. Mechanically Induced Cation Redistribution in $ZnFe_2O_4$ and Its Thermal Stability. *Phys. B* **1997**, *234–236*, 617–619.

(20)   Granone, L.I.; Dillert, R.; Heitjans, P.; Bahnemann, D.W. Effect of the Degree of Inversion on the Electrical Conductivity of Spinel $ZnFe_2O_4$. *ChemistrySelect* **2019**, *4*, 1232–1239.

(21)   Mitra, J.; Ghosh, M.; Bordia, R.K.; Sharma, A. Photoluminescent Electrospun Submicron Fibers of Hybrid Organosiloxane and Derived Silica. *RSC Adv.* **2013**, *3*, 7591–7600.

(22)   Vinosha, P.A.; Mely, L.A.; Jeronsia, J.E.; Krishnan, S.; Das, S.J. Synthesis and Properties of Spinel $ZnFe_2O_4$ Nanoparticles by Facile Co-precipitation Route. *Optik (Stuttg).* **2017**, *134*, 99–108.

(23)   Kočí, K.; Obalová, L.; Matějová, L.; Plachá, D.; Lacný, Z.; Jirkovský, J.; Šolcová, O. Effect of TiO_2 Particle Size on the Photocatalytic Reduction of CO_2. *Appl. Catal. B Environ.* **2009**, *89*, 494–502.

(24)   Dodd, A.C.; McKinley, A.J.; Saunders, M.; Tsuzuki, T. Effect of Particle Size on the Photocatalytic Activity of Nanoparticulate Zinc Oxide. *J. Nanoparticle Res.* **2006**, *8*, 43–51.

(25)   Sivula, K.; Le Formal, F.; Grätzel, M. Solar Water Splitting: Progress Using Hematite (α-Fe_2O_3) Photoelectrodes. *ChemSusChem* **2011**, *4*, 432–449.

(26)   Kim, J.H.; Kim, J.H.; Jang, J.W.; Kim, J.Y.; Choi, S.H.; Magesh, G.; Lee, J.; Lee, J.S. Awakening Solar Water-splitting Activity of $ZnFe_2O_4$ Nanorods by Hybrid Microwave Annealing. *Adv. Energy Mater.* **2015**, *5*, 1401933.

(27)   Guijarro, N.; Bornoz, P.; Prévot, M.S.; Yu, X.; Zhu, X.; Johnson, M.;

Jeanbourquin, X.A.; Le Formal, F.; Sivula, K. Evaluating Spinel Ferrites MFe$_2$O$_4$ (M = Cu, Mg, Zn) as Photoanodes for Solar Water Oxidation: Prospects and Limitations. *Sustain. Energy Fuels* **2018**, *2*, 103–117.

(28)   Kahn, A. Fermi Level, Work Function and Vacuum Level. *Mater. Horizons* **2016**, *3*, 7–10.

(29)   Trasatti, S. The Absolute Electrode Potential: An Explanatory Note. *Pure Appl. Chem.* **1986**, *58*, 955.

(30)   Matsumoto, Y. Energy Positions of Oxide Semiconductors and Photocatalysis with Iron Complex Oxides. *J. Solid State Chem.* **1996**, *126*, 227–234.

(31)   Raebiger, H.; Lany, S.; Zunger, A. Origins of the p-Type Nature and Cation Deficiency in Cu$_2$O and Related Materials. *Phys. Rev. B* **2007**, *76*, 45209.

(32)   Nunome, T.; Irie, H.; Sakamoto, N.; Sakurai, O.; Shinozaki, K.; Suzuki, H.; Wakiya, N. Magnetic and Photocatalytic Properties of n- and p-Type ZnFe$_2$O$_4$ Particles Synthesized Using Ultrasonic Spray Pyrolysis. *J. Ceram. Soc. Japan* **2013**, *121*, 26–30.

(33)   Šutka, A.; Pärna, R.; Kleperis, J.; Käämbre, T.; Pavlovska, I.; Korsaks, V.; Malnieks, K.; Grinberga, L.; Kisand, V. Photocatalytic Activity of Non-Stoichiometric ZnFe$_2$O$_4$ Under Visible Light Irradiation. *Phys. Scr.* **2014**, *89*, 44011.

(34)   Zheng, X.-L.; Dinh, C. T.; Pelayo García de Arquer, F.; Zhang, B.; Liu, M.; Voznyy, O.; Li, Y.-Y.; Knight, G.; Hoogland, S.; Lu, Z.-H.; et al. ZnFe$_2$O$_4$ Leaves Grown on TiO$_2$ Trees Enhance Photoelectrochemical Water Splitting. *Small* **2016**, *12*, 3181–3188.

(35)   Liu, X.; Zheng, H.; Li, Y.; Zhang, W. Factors on the Separation of Photogenerated Charges and the Charge Dynamics in Oxide/ZnFe$_2$O$_4$ Composites. *J. Mater. Chem. C* **2013**, *1*, 329–337.

(36)   Nada, A. A.; Nasr, M.; Viter, R.; Miele, P.; Roualdes, S.; Bechelany, M. Mesoporous ZnFe$_2$O$_4$@TiO$_2$ Nanofibers Prepared by Electrospinning Coupled to PECVD as Highly Performing Photocatalytic Materials. *J. Phys. Chem. C* **2017**, *121*, 24669–24677.

(37)   Yao, J.; Li, X.; Li, Y.; Le, S. Density Functional Theory Investigations on the Structure and Electronic Properties of Normal Spinel ZnFe$_2$O$_4$. *Integr. Ferroelectr.* **2013**, *145*, 17–23.

(38)   Lv, H.; Ma, L.; Zeng, P.; Ke, D.; Peng, T. Synthesis of Floriated ZnFe$_2$O$_4$ with
        Porous Nanorod Structures and Its Photocatalytic Hydrogen Production under
        Visible Light. *J. Mater. Chem.* **2010**, *20*, 3665–3672.

(39)   Lemine, O. M.; Bououdina, M.; Sajieddine, M.; Al-Saie, A. M.; Shafi, M.; Khatab,
        A.; Al-Hilali, M.; Henini, M. Synthesis, Structural, Magnetic and Optical
        Properties of Nanocrystalline ZnFe$_2$O$_4$. *Phys. B Condens. Matter* **2011**, *406*,
        1989–1994.

(40)   Zhu, X.; Zhang, F.; Wang, M.; Ding, J.; Sun, S.; Bao, J.; Gao, C. Facile Synthesis,
        Structure and Visible Light Photocatalytic Activity of Recyclable ZnFe$_2$O$_4$/TiO$_2$.
        Appl. Surf. Sci. **2014**, *319*, 83–89.

(41)   Fang, Z.; Wang, Y.; Xu, D.; Tan, Y.; Liu, X. Blue Luminescent Center in ZnO Films
        Deposited on Silicon Substrates. *Opt. Mater.* **2004**, *26*, 239–242.

(42)   Srivastava, A. K.; Deepa, M.; Bahadur, N.; Goyat, M. S. Influence of Fe Doping
        on Nanostructures and Photoluminescence of Sol-Gel Derived ZnO. *Mater.
        Chem. Phys.* **2009**, *114*, 194–198.

(43)   Chen, A. J.; Wu, X. M.; Sha, Z. D.; Zhuge, L. J.; Meng, Y. D. Structure and
        Photoluminescence Properties of Fe-Doped ZnO Thin Films. *J. Phys. D. Appl.
        Phys.* **2006**, *39*, 4762–4765.

(44)   Kittel, C. *Introduction to Solid State Physics*, VIII.; John Wiley & Sons: New York,
        2005.

(45)   Sun, S.; Yang, X.; Zhang, Y.; Zhang, F.; Ding, J.; Bao, J.; Gao, C. Enhanced
        Photocatalytic Activity of Sponge-Like ZnFe$_2$O$_4$ Synthesized by Solution
        Combustion Method. *Prog. Nat. Sci. Mater. Int.* **2012**, *22*, 639–643.

(46)   Xie, T.; Xu, L.; Liu, C.; Wang, Y. Magnetic Composite ZnFe$_2$O$_4$/SrFe$_{12}$O$_{19}$:
        Preparation, Characterization, and Photocatalytic Activity under Visible Light.
        Appl. Surf. Sci. **2013**, *273*, 684–691.

(47)   Brunauer, S.; Emmett, P.H.; Teller, E. Adsorption of Gases in Multimolecular
        Layers. *J. Am. Chem. Soc.* **1938**, *60*, 309–319.

(48)   Melhuish, W.H. Quantum Efficiencies of Fluorescence of Organic Substances:
        Effect of Solvent and Concentration of the Fluorescent Solute. *J. Phys. Chem.*
        1961, *65*, 229–235.

(49)   Fletcher, A.N. Quinine Sulfate as a Fluorescence Quantum Yield Standard.
        Photochem. Photobiol. **1969**, *9*, 439–444.

(50)   Würth, C.; Grabolle, M.; Pauli, J.; Spieles, M.; Resch-Genger, U. Relative and Absolute Determination of Fluorescence Quantum Yields of Transparent Samples. *Nat. Protoc.* **2013**, *8*, 1535–1550.

Chapter 5

Summarizing Discussion and Conclusions

This thesis aimed to understand how the degree of inversion impacts on the optical properties as well as on the charge carrier transport and the electronic properties of the spinel zinc ferrite ($ZnFe_2O_4$, ZFO). Fundamental research regarding these issues was scarce and, therefore, the impact of the cation distribution on the photoelectrochemical activity of ZFO was poorly understood. The only report concerning the effect of the degree of inversion on the photoelectrochemical activity of ZFO has recently been presented by Zhu *et al*.[1] The authors showed that ZFO photoanodes with a relatively poor crystallinity but a higher degree of inversion exhibit a higher photoelectrochemical activity than samples with higher crystallinity and lower degree of inversion. This result was ascribed to the superior photogenerated charge separation efficiency and the improved majority charge carrier transport of the samples having a higher degree of inversion. However, properties such as the crystallinity or the concentration of surface defects were rather heterogeneous within the samples. In fact, the authors reported that the ZFO sample with the highest degree of inversion and the lowest crystallinity, which was prepared at a low temperature, did not show the highest photoelectrochemical activity as was expected. This result was attributed to a high concentration of surface defects acting as recombination centers. The authors suggested that the surface defects are repaired by the heat treatment and, therefore, were not present in the rest of the samples prepared at higher temperatures.

In the scientific literature, a large dispersion exists between the photoelectrochemical efficiencies reported for ZFO samples prepared by different techniques (Fig. 5.1). Furthermore, the structural characterization of the reported ZFO photoanodes is usually insufficient because the cation distribution is not determined. Therefore, understanding the effect of the degree of inversion on the photoelectrochemical activity of ZFO was required to confirm whether the

dispersion in the reported data might be explained by considering differences in the cation distribution between the samples or not. In addition, the recently established benchmark for the water oxidation photocurrent under simulated solar irradiation using a ZFO photoanode has been reported to be one order of magnitude smaller than the predicted theoretical maximum value of about 11 mA cm^{-2}.[1] Thus, by studying the impact of the degree of inversion on the photoelectrochemical activity of ZFO, some mechanistic aspects explaining the reported low efficiencies have been elucidated herein.
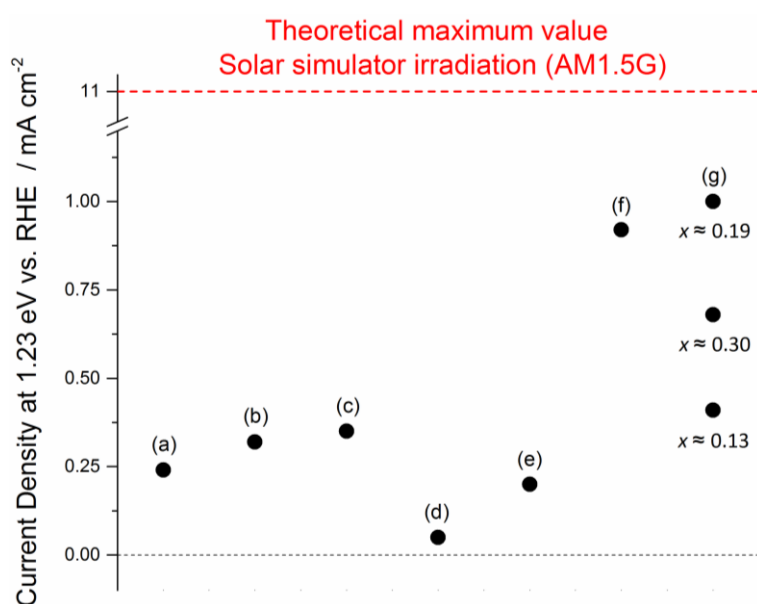
Fig. 5.1. Current densities reported in the literature during the past four years for the water oxidation reaction on ZFO photoanodes. The current densities were measured with an applied external bias of 1.23 V vs. RHE under simulated solar irradiation (1000 W m^{-2}). The red dashed line indicates the maximum theoretical photocurrent of about 11 mA cm^{-2} predicted for ZFO. The spots (a) to (f) correspond to Ref. 2 to 7, respectively. The different spots in (g) correspond to current densities for ZFO photoanodes with different degree of inversion (Ref. 1). This figure is a reprint of Fig. 1.3 from page 8 in Chapter 1.

In order to reveal the intrinsic effect of the degree of inversion on the photoelectrochemical activity of ZFO, a systematic study of samples in which the cation distribution is the only variable was necessary. To carry out this investigation, pristine ZFO samples having different degrees of inversion ranging from $x \approx 0.07$ to

$x \approx 0.20$ were synthesized. The highly pure ZFO samples exhibited, within the limit of the experimental determination, equal particle size, crystallite size, and crystallinity, as was confirmed by XRD plus Rietveld refinement, Mössbauer spectroscopy, Raman spectroscopy, scanning electron microscopy, and elemental analysis. Furthermore, oxygen vacancies were not detected. Thus, the degree of inversion was identified to be the only independent variable between the different ZFO samples. This is an important issue because the particle and crystallite size, as well as the number of oxygen vacancies, are known to have considerable impact on the photoelectrochemical properties of iron-containing semiconductors.[8,9] Therefore, no contributions arising from differences in the particle or crystallite size or in the oxygen vacancies density that might overlay the intrinsic effect of the degree of inversion were expected.

As was mentioned in Chapter 1 (*cf.* page 9), a photoelectrochemical process depends on the synergetic interaction between six major events, *i.e.*, the photon absorption, the exciton separation, the charge carrier diffusion, the charge carrier transport, the catalytic efficiency, and the mass transfer of reactants and products.[10] Due to the photon absorption, electrons are excited to the conduction band creating vacancies (holes) in the valence band of the semiconductor. The thus formed electron-hole pairs, also called excitons, are then separated and electrons and holes migrate independently from each other. Both, charge carrier diffusion and transport are responsible for the charge carrier transfer within the semiconductor. In a photoanode, electrons are transferred through the bulk of the material into the back electric contact and holes are transferred to the semiconductor-electrolyte interface. The electrical field produced by the bending of the conduction and valence bands is largely responsible for the separation and the migration of electrons and holes. Once at the interface, the holes can oxidize the species present in the surrounding electrolyte. The efficiency of the latter process depends on both, the probability of the surface charge transfer (catalytic efficiency) and the diffusion of the reactants and products (mass transfer). These steps are

shown in Fig. 5.2A for a schematic ZFO photoanode. As reported throughout the thesis, the degree of inversion was found to have a large effect on the photon absorption, the exciton separation, and the charge carrier transport properties of ZFO, consequently affecting its photoelectrochemical activity (Fig. 5.2B).


(A)

ZnFe$_2$O$_4$ Photoanode e$^-$

1. Photon Absorption
2. Exciton Separation
3-4. Charge Carrier Diffusion/Transport
5. Catalytic Efficiency
6. Mass Transfer

Zn^{2+} 4s Orbitals

Fe^{3+} 3d Orbitals

O^{2-} 2p Orbitals

Oxidation D → D$^+$

(B)

x ≈ 0.20

Effect of the Degree of Inversion

• No Change in the Band Gap Energy

• Increase in the Probability of the O^{2-} 2p to Zn^{2+} 4s Transition

• Decrease in the Probability of the O^{2-} 2p to Fe^{3+} 3d Transition

• Three Orders of Magnitude Increase in the Electrical Conductivity

x ≈ 0.07

Five Times Higher Activity for the PEC Methanol Oxidation Reaction

Fig. 5.2. **(A)** Scheme of a ZFO photoanode showing the six major events involved in a photoelectrochemical process, *i.e.*, photon absorption, exciton separation, charge carrier diffusion, charge carrier transport, catalytic efficiency, and mass transfer of reactants and products. The charge carrier diffusion and charge carrier transport processes commonly take place simultaneously.[10] **(B)** Summary of the main effects of the degree of inversion on the physicochemical properties and photoelectrochemical (PEC) activity of ZFO observed in the present work.

The effect of the degree of inversion on the photon absorption properties was studied by room-temperature time averaged UV-Vis-NIR diffuse reflectance and photoluminescence spectroscopy, as well as by transient photoluminescence spectroscopy. From the UV-Vis-NIR diffuse reflectance measurements, it was deduced that the band gap energies of ZFO are independent of the cation distribution. An indirect band gap transition at 614 nm (≈ 2.0 eV) as well as a direct band gap transition at 532 nm (≈ 2.3 eV) and a third transition at 450 mn (≈ 2.7 eV) were observed for all the samples. In addition, broad signals due to electronic ligand

field transitions originating from octahedrally coordinated Fe^{3+} cations were observed at 1200 and at 795 nm. According to the ligand field theory, additional *d-d* transitions for octahedrally coordinated Fe^{3+} cations were predicted at 494, 448, 407, and 328 nm. These signals are not easily recognized in the UV-Vis-NIR diffuse reflectance measurements (Fig. 5.3) because they overlap with the band gap transitions previously mentioned. The degree of inversion was found to have an effect on the probability of the electronic ligand field transitions of the Fe^{3+} cations. As a consequence, a darkening of the ZFO samples due to a higher visible light absorptivity was observed as the degree of inversion was increased. It is important to stress that the increase in the visible light absorptivity is purely related to changes in the ligand field transitions and not to a band gap narrowing. From the room-temperature photoluminescence measurements, three emission signals at 625 nm ($\approx$ 2.0 eV), 547 nm ($\approx$ 2.3 eV), and 464 nm ($\approx$ 2.7 eV) were observed independently of the cation distribution of the ZFO samples. The energy of these emissions is in good agreement with the band gap transitions deduced by the UV-Vis-NIR diffuse reflectance measurements. The existence of two different band gap transitions might be attributed to a discontinuity in the density of empty electronic energetic states forming the conduction band of ZFO. Thus, within the conduction band the photoexcited electrons might be delocalized in confined and independent states involving either Fe^{3+} $3d$ levels or Zn^{2+} $4s$ levels (Fig. 5.4). Therefore, the transitions observed at approximately 2.0, 2.3, and 2.7 eV are ascribed to indirect O^{2-} $2p$ to Fe^{3+} $3d$, direct O^{2-} $2p$ to Fe^{3+} $3d$, and O^{2-} $2p$ to Zn^{2+} $4s$ electronic transitions, respectively. As the degree of inversion increases, the probability of the O^{2-} $2p$ to Zn^{2+} $4s$ electronic transition increases and the probability of the O^{2-} $2p$ to Fe^{3+} $3d$ transition decreases. Incident photon-to-current efficiency measurements revealed that the charge carriers generated *via* the O^{2-} $2p$ to Zn^{2+} $4s$ transition are more efficient towards the methanol oxidation reaction than the ones generated *via* the O^{2-} $2p$ to Fe^{3+} $3d$ transition. In other words, as the cation distribution increases, the light harvested by the material is utilized in a more efficient way to generate a photoelectrochemical oxidation reaction. It is important to stress that the valence

band holes generated *via* both, the O^{2-} $2p$ to Zn^{2+} $4s$ and O^{2-} $2p$ to Fe^{3+} $3d$ transitions have the same redox potential and, therefore, the same oxidizing activity. The higher efficiency of the O^{2-} $2p$ to Zn^{2+} $4s$ transition is due to the longer lifetime observed by transient photoluminescence spectroscopy for the thus formed electron-hole pairs. A larger lifetime implicates a higher probability for the electron-hole separation event to occur and, thus, a decrease in the electron-hole recombination rate, which results in a higher photoelectrochemical activity. The contributions from the *d-d* transitions and from the indirect O^{2-} $2p$ to Fe^{3+} $3d$ band gap transitions to the incident photon-to-current efficiency were found to be negligible. Thus, the charge carriers generated *via* this processes do not participate in the photoelectrochemical process and, hence, do not contribute to the efficiency of the material. As obvious from the results shown in Fig. 5.3, the fate of a significant fraction of the absorbed photons is the generation of these futile (from a photoelectrochemical point of view) transitions.
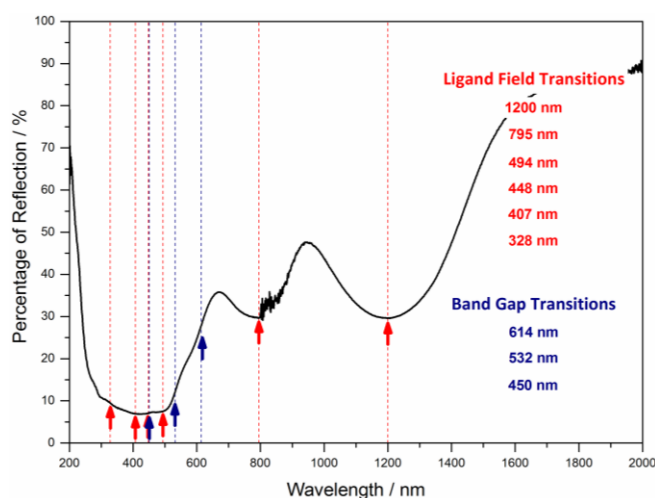
Fig. 5.3. UV-Vis-NIR diffuse reflectance spectra of the ZFO sample having a degree of inversion of *x* = 0.07. The red arrows at 1200, 795, 494, 448, 407, and 328 nm indicate the position of the ligand field transitions involving octahedrally coordinated Fe^{3+} cations. The blue arrows indicate the position of the band gap transitions. The transitions at 614, 532, and 464 nm correspond to the indirect O^{2-} $2p$ to Fe^{3+} $3d$, direct O^{2-} $2p$ to Fe^{3+} $3d$, and O^{2-} $2p$ to Zn^{2+} $4s$ electronic transitions, respectively. Only the band gap transitions at 532 and 464 nm contribute to the photoelectrochemical activity of the material. Similar results concerning the transition wavelengths were observed for the samples having higher degrees of inversion.
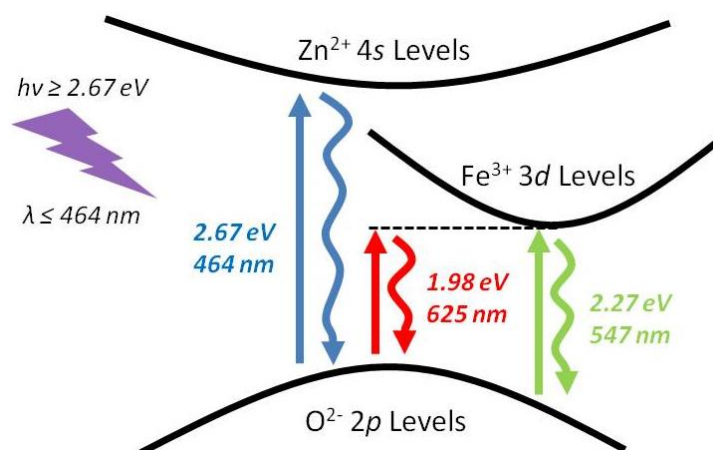
Fig. 5.4. Scheme of the electronic transitions observed for ZFO when photons having wavelengths shorter than 464 nm (energy higher than 2.67 eV) are used for the excitation. Reprinted from Ref. 11.

The impact of the cation distribution on the exciton separation and the charge carrier transport properties were also investigated. The conductivity of ZFO was found to increase from $\approx 10^{-7}$ to 10^{-5} S cm^{-1} and the activation energy of the conduction process decreases from ≈ 0.45 to 0.20 eV by increasing the degree of inversion from 0.13 to 0.16. The charge carrier mobility and the conductivity are found to be directly proportional.[12] Thus, an increase of two orders of magnitude in the conductivity results in an increase in the charge carrier mobility of the same magnitude. Furthermore, the charge carrier mobility depends exponentially on the activation energy of the conducting process.[13] Therefore, a reduction of the activation energy by a factor of 2 generates an increase in the charge carrier mobility by a factor of $e^2 \approx 7.4$. It is well-known that as the charge carrier mobility of a semiconductor increases, the photogenerated charge separation is favored and the electron-hole recombination rates are reduced.[14] Bohn et $al.$[15] reported an increase in the photoelectrochemical water oxidation activity of α-Fe$_2$O$_3$ of three orders of magnitude as a result of an increase in the electrical conductivity from 10^{-11} to 10^{-8} S cm^{-1} via Sn doping. Analogous results were reported for other doped semiconductors (Table 5.1). The large increase of two orders of magnitude observed as a consequence of a small change in the degree of inversion reveals the great impact of the cation distribution on the properties of the material. The fact

that the conductivity of ZFO is enhanced only by structural changes, such as an increase in the degree of inversion, without changing the elemental composition is an advantage in comparison to other semiconductors, which are usually doped with other elements to increase their conductivity. Although doping is a well-established technique, it is not straightforward to perform because detrimental rather than positive effects might be observed in the photoelectrochemical activity when the doping ratio is not optimal.[16–18] A positive effect of doping, in addition to the increase in the conductivity, is that dopants might act as trapping centers for the charge carriers, thus reducing the recombination rates.[18] However, doping can reduce the oxidation and reduction potentials of the charge carriers and the dopants might also act as recombination centers, thus increasing the recombination rates.[19,20]

Table 5.1. Effect of elemental doping on the electrical conductivity (σ) and the photoelectrochemical (PEC) activity of some semiconductors commonly used as photoanode materials for photoelectrochemical water oxidation.

Semiconductor	Dopant	σ_{Doped} / $\sigma_{Pristine}$	[PEC activity]$_{Doped}$ / [PEC activity]$_{Pristine}$	Reference
α-Fe$_2$O$_3$	Sn	10^3	10^3 [1]	15
ZFO	Ti	3.40	8.75 [1]	21
BiVO$_4$	Mo	10	2 [2]	22
WO$_3$	Al	1.4	1.3 [3]	23

[1] Photocurrent density at 1.23 V vs. RHE in 1 mol L^{-1} NaOH under simulated solar irradiation (AM1.5G filter, 1000 W m^{-2}). [2] Photocurrent density at 1.23 V vs. RHE in 0.2 mol L^{-1} Na$_2$SO$_4$ and 0.1 mol L^{-1} PO$_4^{3-}$ buffer solution (pH 6.6) under simulated solar irradiation (AM1.5G filter, 1000 W m^{-2}). [3] Photocurrent density at 1.2 vs. Ag/AgCl in 0.5 mol L^{-1} H$_2$SO$_4$ under Xe lamp irradiation (1000 W m^{-2}, 400 nm cutoff filter).

The degree of inversion clearly has a large impact on the photon absorption, the exciton separation, and the charge carriers transport properties of ZFO (Fig. 5.2B). As a consequence, the cation distribution also affects the photoelectrochemical activity of the ZFO photoanodes. The current densities

obtained for the methanol oxidation reaction under simulated solar irradiation are presented in Fig. 5.5 as a function of the degree of inversion. The photoelectrochemical activity increases as the cation distribution increases. There is apparently an onset value for the degree of inversion between 0.13 and 0.16 after which the measured current densities increase at a significantly higher rate (black dashed line, Fig. 5.5). The conductivity of the samples was found to exhibit a similar behavior and, by increasing the degree of inversion from 0.13 to 0.16, an increase of two orders of magnitude was observed. Therefore, the enhanced photoelectrochemical activity of the samples having higher degrees of inversion can mainly be ascribed to their improved charge carrier transport properties. In addition, as previously mentioned, an increase in the cation distribution generates an increase in the probability of the more efficient O^{2-} $2p$ to Zn^{2+} $4s$ band gap transition. However, the observed difference concerning the probability of the electronic transitions is not as significant as the differences in the conductivity. The relative photoluminescence quantum yield related to the O^{2-} $2p$ to Zn^{2+} $4s$ transition only increases from $5.4 \cdot 10^{-3}$ % to $6.4 \cdot 10^{-3}$ % ($\approx$ 20 % increase) as the degree of inversion increases from 0.07 to 0.20. Therefore, a contribution, but to a lesser extent, is expected from the increase in the probability of the O^{2-} $2p$ to Zn^{2+} $4s$ band gap transition.

It becomes evident from the experimental results presented in this thesis that the degree of inversion directly impacts the photoelectrochemical activity of ZFO. Additionally, it is well-known that the cation distribution of nanoparticulate ZFO samples could exhibit values ranging from $x \approx 0$ (nearly normal structure) to $x \approx 1$ (nearly inverse structure) depending on the synthetic conditions. Therefore, it is readily assumed that different degrees of inversion between the ZFO photoanodes reported in the literature (Fig. 5.1) might be the major reason explaining the large dispersion observed for their photoelectrochemical activities.
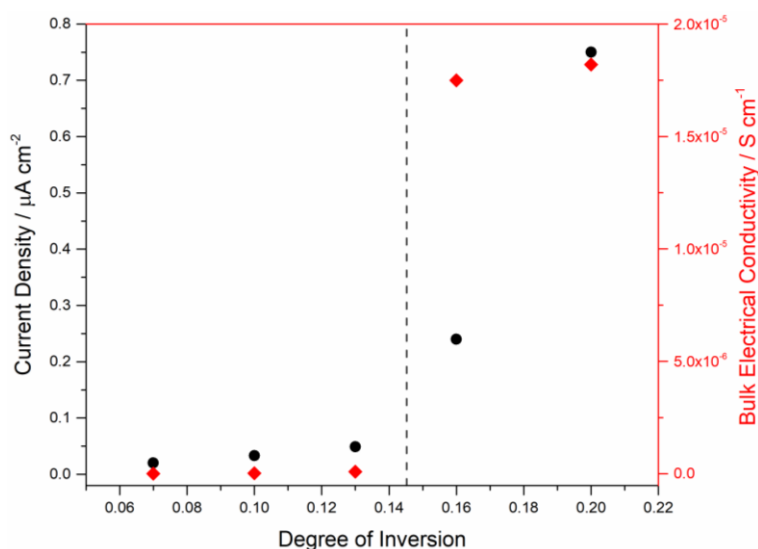
Fig. 5.5. Current densities obtained for the photoelectrochemical methanol oxidation reaction under simulated solar irradiation (black spots) and bulk electrical conductivity (red diamonds) of ZFO as a function of the degree of inversion. The grey dashed line indicates an onset value of the cation distribution between x ≈ 0.13 and x ≈ 0.16 after which the electrical conductivity and the photoelectrochemical activity of ZFO increase significantly.

Furthermore, general conclusions regarding the poor photoelectrochemical performance of ZFO photoanodes arise from the results presented in the present work. Independent of the cation distribution, ligand field transitions contribute to the visible light absorptivity of ZFO (Fig. 5.3). The theoretical maximum efficiency of 11 mA cm^{-2} for the water oxidation reaction on ZFO photoanodes is calculated assuming that photons with energy higher or equal than the direct band gap are completely absorbed by the material, and all the photogenerated holes participate in the interfacial charge transfer reaction. However, in practice, the fate of the absorbed photons is not only the generation of electron-hole pairs. Futile *d-d* electronic ligand field transitions originating from octahedrally and tetrahedrally coordinated Fe^{3+} cations are also generated. In fact, all of the well-known photoelectrochemically highly active semiconductors, such as TiO_2,[24] WO_3,[25] $BiVO_4$,[26] or Cu_2O,[27] to mention only a few, have completely empty or fully occupied *d* levels in the outer electron shell. Therefore, these materials do not exhibit *d-d* ligand field transitions. The Fe^{3+} *d-d* transitions observed for ZFO are assumed to be

a major reason for the difference of one order of magnitude between the reported benchmark and the theoretical efficiency.

The low relative quantum efficiencies (between 0.03 % and 0.05 %) obtained for the ZFO samples suggest that, as well as α-Fe_2O_3, charge carriers generated by the light excitation decay to the ground state by high efficient nonradiative processes.[28] This might be attributed to a high density of trap states or a strong coupling between trap states.[28]

Concerning the events involved in the photoelectrochemical activity of ZFO shown in Fig. 5.2A, the effect of the cation distribution on the catalytic efficiency for the water oxidation reaction and on the mass transfer of reactants and products is still unknown. Photoelectrochemical processes are heterogeneous catalytic reactions occurring at the semiconductor-electrolyte interface (Fig. 5.6A). Therefore, the photoelectrochemical activity depends on the ability of the surface atoms to interact with molecules or ions being present in the surrounding electrolyte *via* the formation or the breaking of specific chemical bonds.[29] The dynamics of the charge carriers and the interfacial charge transfer processes depend on the surface properties as well.[30–33] However, no reports concerning the effect of the degree of inversion on the surface chemistry of ZFO are found in the scientific literature. Thus, an impact of the surface chemistry on the photoelectrochemical activity of the ZFO samples having different cation distribution cannot be discarded. Certainly, this issue must be addressed in the future in order to access a complete insight concerning the effect of the degree of inversion on the physicochemical properties directly related to the photoelectrochemical activity of ZFO.

Water oxidation catalysts (WOCs), specially nickel-iron oxides, have been reported to greatly improve the performance of ZFO photoanodes.[1] Although the role of WOCs is not yet fully understood, it seems to depend on two major processes.[14] The first one is the reduction of the electron-hole surface

recombination by preventing back-electron transfer or by chemically passivating surface traps. The second one is the reduction of the overpotential for the water oxidation reaction. Through these two processes, WOCs promotes the hole injection into the surrounding electrolyte and improve the catalytic water oxidation activity (Fig. 5.6B).[7] The low photoelectrochemical efficiencies of ZFO observed here and reported in the literature suggest that the water oxidation reaction is poorly catalyzed by the ZFO surface.[1–7] Therefore, WOCs have to be deposited on ZFO photoanodes in order to enhance their photoelectrochemical activities.
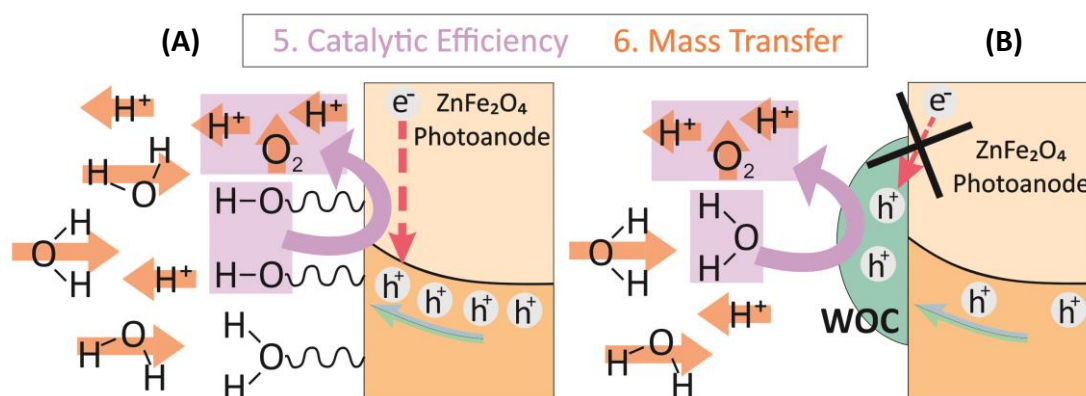
Fig. 5.6. **(A)** Simplified scheme of the processes occurring at the electrolyte-ZFO interface during the photocatalytic water oxidation reaction. The efficiency of the process depends at least on two events. One is the probability of the surface charge transfer, i.e., the electron injection from adsorbed H_2O or OH^- species (catalytic efficiency) into the photogenerated holes in the valence band of ZFO. The second is the diffusion of the reactants (H_2O) towards the ZFO surface and the diffusion of the products (O_2 and H^+) in the opposite direction (mass transfer). **(B)** The deposition of a water oxidation catalyst (WOC) on the surface of ZFO improves the photoelectrochemical efficiency by reducing both, the electron-hole surface recombination rate and the overpotential for the water oxidation reaction.

During the last four years, ZFO was extensively investigated in order to develop photoanodes having the advantageous features of α-Fe_2O_3 but without its main limitations. However, the current benchmark efficiency of ZFO, reported for a nanorod array photoanode having a nickel-iron oxide overlayer,[1] is four times lower than that of α-Fe_2O_3, which has been reported for a single-crystalline wormlike photoanode modified by platinum doping.[34] The results presented in this work are a

step forward to understand some factors limiting the efficiency of ZFO photoanodes and to provide a fundamental insight regarding the effect of the degree of inversion on the physicochemical properties of ZFO which are directly related to its photoelectrochemical activity. Furthermore, this thesis leaves the message that a scientific report concerning the photoelectrochemical activity of a ZFO photoanode is meaningful only when the results are presented together with the respective degree of inversion of each sample.

References

(1)   Zhu, X.; Guijarro, N.; Liu, Y.; Schouwink, P.; Wells, R. A.; Le Formal, F.; Sun, S.; Gao, C.; Sivula, K. Spinel Structural Disorder Influences Solar-Water-Splitting Performance of $ZnFe_2O_4$ Nanorod Photoanodes. *Adv. Mater.* **2018**, *30*, 1801612.

(2)   Kim, J. H.; Kim, J. H.; Jang, J. W.; Kim, J. Y.; Choi, S. H.; Magesh, G.; Lee, J.; Lee, J. S. Awakening Solar Water-Splitting Activity of $ZnFe_2O_4$ Nanorods by Hybrid Microwave Annealing. *Adv. Energy Mater.* **2015**, *5*, 1401933.

(3)   Kim, J. H.; Jang, Y. J.; Kim, J. H.; Jang, J. W.; Choi, S. H.; Lee, J. S. Defective $ZnFe_2O_4$ Nanorods with Oxygen Vacancy for Photoelectrochemical Water Splitting. *Nanoscale* **2015**, *7*, 19144–19151.

(4)   Hufnagel, A. G.; Peters, K.; Müller, A.; Scheu, C.; Fattakhova-Rohlfing, D.; Bein, T. Zinc Ferrite Photoanode Nanomorphologies with Favorable Kinetics for Water-Splitting. *Adv. Funct. Mater.* **2016**, *26*, 4435–4443.

(5)   Peeters, D.; Taffa, D. H.; Kerrigan, M. M.; Ney, A.; Jöns, N.; Rogalla, D.; Cwik, S.; Becker, H. W.; Grafen, M.; Ostendorf, A.; et al. Photoactive Zinc Ferrites Fabricated via Conventional CVD Approach. *ACS Sustain. Chem. Eng.* **2017**, *5*, 2917–2926.

(6)   Guijarro, N.; Bornoz, P.; Prévot, M. S.; Yu, X.; Zhu, X.; Johnson, M.; Jeanbourquin, X. A.; Le Formal, F.; Sivula, K. Evaluating Spinel Ferrites MFe_2O_4 (M = Cu, Mg, Zn) as Photoanodes for Solar Water Oxidation: Prospects and Limitations. *Sustain. Energy Fuels* **2018**, *2*, 103–117.

(7)   Kim, J. H.; Jang, Y. J.; Choi, S. H.; Lee, B. J.; Kim, J. H.; Park, Y. Bin; Nam, C. M.; Kim, H. G.; Lee, J. S. A Multitude of Modifications Strategy of $ZnFe_2O_4$ Nanorod Photoanodes for Enhanced Photoelectrochemical Water Splitting Activity. *J. Mater. Chem. A* **2018**, *6*, 12693–12700.

(8)   Cesar, I.; Sivula, K.; Kay, A.; Zboril, R.; Grätzel, M. Influence of Feature Size, Film Thickness, and Silicon Doping on the Performance of Nanostructured Hematite Photoanodes for Solar Water Splitting. *J. Phys. Chem. C* **2009**, *113*, 772–782.

(9)   Yang, T.-Y.; Kang, H.-Y.; Sim, U.; Lee, Y.-J.; Lee, J.-H.; Koo, B.; Nam, K. T.; Joo, Y.-C. A New Hematite Photoanode Doping Strategy for Solar Water Splitting:

Oxygen Vacancy Generation. *Phys. Chem. Chem. Phys.* **2013**, *15*, 2117–2124.

(10)   Takanabe, K. Photocatalytic Water Splitting: Quantitative Approaches toward Photocatalyst by Design. *ACS Catal.* **2017**, *7*, 8006–8022.

(11)   Granone, L. I.; Nikitin, K. V.; Emeline, A. V.; Dillert, R.; Bahnemann, D. W. Effect of the Degree of Inversion on the Photoelectrochemical Activity of Spinel ZnFe$_2$O$_4$. *Catalysts* **2019**, 9, 434.

(12)   Li, S.; Cai, J.; Liu, Y.; Gao, M.; Cao, F.; Qin, G. Tuning Orientation of Doped Hematite Photoanodes for Enhanced Photoelectrochemical Water Oxidation. *Sol. Energy Mater. Sol. Cells* **2018**, 179, 328-333.

(13)   Chatman, S.; Pearce, C. I.; Rosso, K. M. Charge Transport at Ti-Doped Hematite (001)/Aqueous Interfaces. *Chem. Mater.* **2015**, *27*, 1665–1673.

(14)   Sivula, K.; van de Krol, R. Semiconducting Materials for Photoelectrochemical Energy Conversion. *Nat. Rev. Mater.* **2016**, *1*, 15010.

(15)   Bohn, C. D.; Agrawal, A. K.; Walter, E. C.; Vaudin, M. D.; Herzing, A. A.; Haney, P. M.; Talin, A. A.; Szalai, V. A. Effect of Tin Doping on α-Fe$_2$O$_3$ Photoanodes for Water Splitting. *J. Phys. Chem. C* **2012**, *116*, 15290–15296.

(16)   Bloh, J. Z.; Dillert, R.; Bahnemann, D. W. Designing Optimal Metal-Doped Photocatalysts: Correlation between Photocatalytic Activity, Doping Ratio, and Particle Size. *J. Phys. Chem. C* **2012**, *116*, 25558–25562.

(17)   Bloh, J. Z.; Dillert, R.; Bahnemann, D. W. Zinc Oxide Photocatalysis: Influence of Iron and Titanium Doping and Origin of the Optimal Doping Ratio. *ChemCatChem* **2013**, *5*, 774–778.

(18)   Bloh, J. Z. Refined Model for the Optimal Metal Content in Semiconductor Photocatalysts. *J. Phys. Chem. C* **2017**, *121*, 844–851.

(19)   Marschall, R. Semiconductor Composites: Strategies for Enhancing Charge Carrier Separation to Improve Photocatalytic Activity. *Adv. Funct. Mater.* **2014**, *24*, 2421–2440.

(20)   Emeline, A. V.; Furubayashi, Y.; Zhang, X.; Jin, M.; Murakami, T.; Fujishima, A. Photoelectrochemical Behavior of Nb-Doped TiO$_2$ Electrodes. *J. Phys. Chem. B* **2005**, *109*, 24441–24444.

(21)   Guo, Y.; Zhang, N.; Wang, X.; Qian, Q.; Zhang, S.; Li, Z.; Zou, Z. A Facile Spray Pyrolysis Method to Prepare Ti-Doped ZnFe$_2$O$_4$ for Boosting Photoelectro-

chemical Water Splitting. *J. Mater. Chem. A* **2017**, *5*, 7571–7577.

(22) He, H.; Berglund, S. P.; Rettie, A. J. E.; Chemelewski, W. D.; Xiao, P.; Zhang, Y.; Mullins, C. B. Synthesis of BiVO$_4$ Nanoflake Array Films for Photoelectrochemical Water Oxidation. *J. Mater. Chem. A* **2014**, *2*, 9371–9379.

(23) Li, W.; Zhan, F.; Li, J.; Liu, C.; Yang, Y.; Li, Y.; Chen, Q. Enhancing Photoelectrochemical Water Splitting by Aluminum-Doped Plate-like WO$_3$ Electrodes. *Electrochim. Acta* **2015**, *160*, 57–63.

(24) Schneider, J.; Matsuoka, M.; Takeuchi, M.; Zhang, J.; Horiuchi, Y.; Anpo, M.; Bahnemann, D. W. Understanding TiO$_2$ Photocatalysis: Mechanisms and Materials. *Chem. Rev.* **2014**, *114*, 9919–9986.

(25) Wang, H.; Lindgren, T.; He, J.; Hagfeldt, A.; Lindquist, S.-E. Photoelectrochemistry of Nanostructured WO$_3$ Thin Film Electrodes for Water Oxidation: Mechanism of Electron Transport. *J. Phys. Chem. B* **2000**, *104*, 5686–5696.

(26) Park, Y.; McDonald, K. J.; Choi, K. S. Progress in Bismuth Vanadate Photoanodes for Use in Solar Water Oxidation. *Chem. Soc. Rev.* **2013**, *42*, 2321–2337.

(27) Paracchino, A.; Laporte, V.; Sivula, K.; Grätzel, M.; Thimsen, E. Highly Active Oxide Photocathode for Photoelectrochemical Water Reduction. *Nat. Mater.* **2011**, *10*, 456–461.

(28) Cherepy, N. J.; Liston, D. B.; Lovejoy, J. A.; Deng, H.; Zhang, J. Z. Ultrafast Studies of Photoexcited Electron Dynamics in γ- and α-Fe$_2$O$_3$ Semiconductor Nanoparticles. *J. Phys. Chem. B* **1998**, *102*, 770–776.

(29) Kamat, P. V. Semiconductor Surface Chemistry as Holy Grail in Photocatalysis and Photovoltaics. *Acc. Chem. Res.* **2017**, *50*, 527–531.

(30) Augustynski, J. The Role of the Surface Intermediates in the Photoelectrochemical Behaviour of Anatase and Rutile TiO$_2$. *Electrochim. Acta* **1993**, *38*, 43–46.

(31) Jeon, T. H.; Choi, W.; Park, H. Photoelectrochemical and Photocatalytic Behaviors of Hematite-Decorated Titania Nanotube Arrays: Energy Level Mismatch versus Surface Specific Reactivity. *J. Phys. Chem. C* **2011**, *115*, 7134–7142.

(32)   Klahr, B.; Gimenez, S.; Fabregat-Santiago, F.; Hamann, T.; Bisquert, J. Water Oxidation at Hematite Photoelectrodes: The Role of Surface States. *J. Am. Chem. Soc.* **2012**, *134*, 4294–4302.

(33)   Le Formal, F.; Pastor, E.; Tilley, S. D.; Mesa, C. A.; Pendlebury, S. R.; Grätzel, M.; Durrant, J. R. Rate Law Analysis of Water Oxidation on a Hematite Surface. *J. Am. Chem. Soc.* **2015**, *137*, 6629–6637.

(34)   Kim, J. Y.; Magesh, G.; Youn, D. H.; Jang, J.-W.; Kubota, J.; Domen, K.; Lee, J. S. Single-Crystalline, Wormlike Hematite Photoanodes for Efficient Solar Water Splitting. *Sci. Rep.* **2013**, *3*, 2681.

Appendix

Appendix A: Supporting information for Chapter 2: Effect of the Degree of Inversion on Optical Properties of Spinel ZnFe$_2$O$_4$

Rietveld plots of zinc ferrite samples
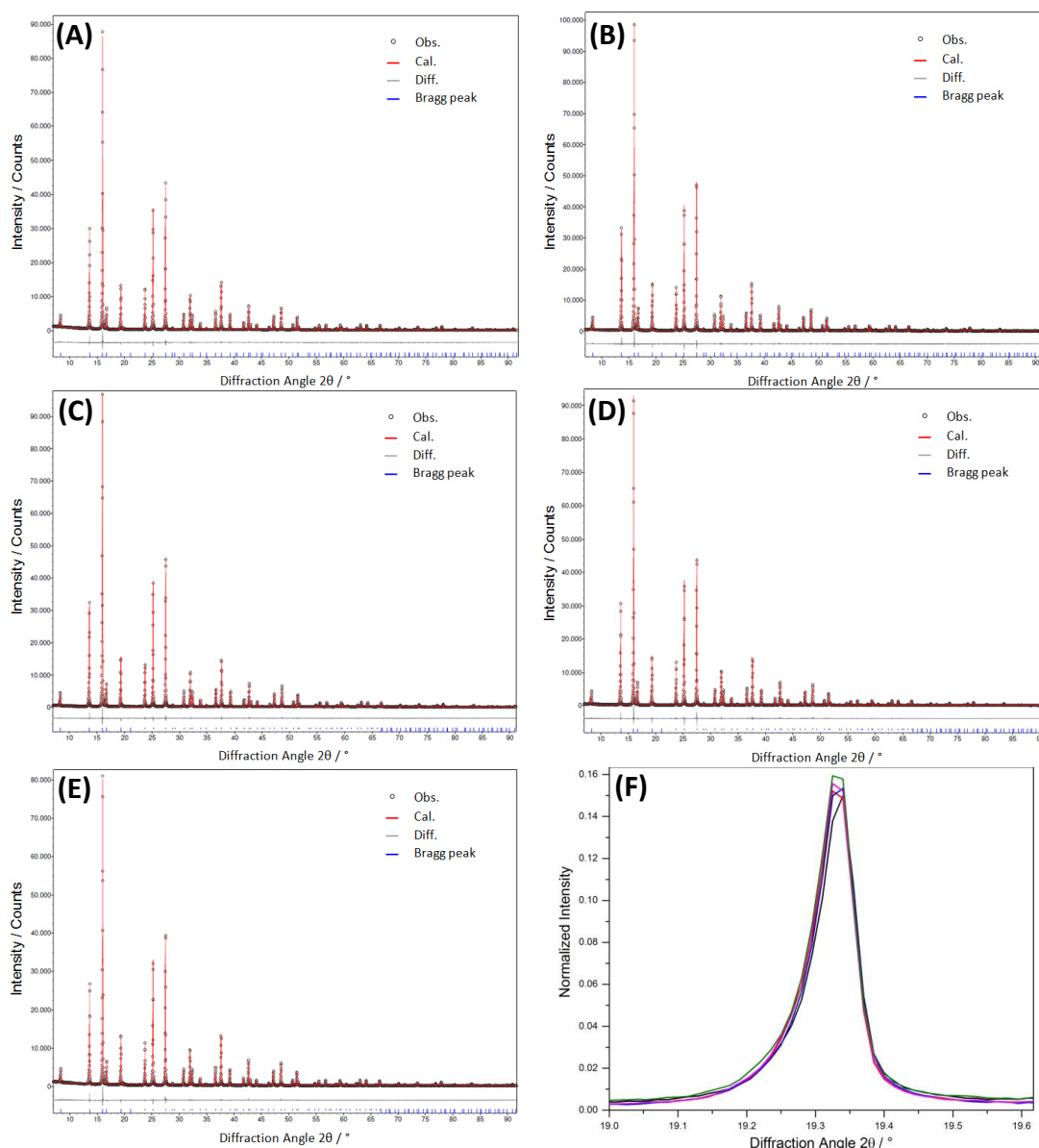
Fig. A1. Rietveld plots of the ZFO samples after calcination at **(A)** 773 K, **(B)** 873 K, **(C)** 973 K, **(D)** 1073 K, and **(E)** 1173 K. Monochromatized MoKα_1 radiation was used for the measurement. **(F)** Magnification of the diffraction peak at 19.33° of the different ZFO samples: ─ ZFO_773, $x = 0.074 \pm 0.011$; ─ ZFO_873, $x = 0.104 \pm 0.013$; ─ ZFO_973, $x = 0.134 \pm 0.008$; ─ ZFO_1073, $x = 0.159 \pm 0.010$; ─ ZFO_1173, $x = 0.203 \pm 0.017$. The diffractograms were normalized to the main diffraction peak at 16.01°. An increase in the relative intensity is observed as the degree of inversion increases from 0.07 to 0.20.

Mössbauer spectra of zinc ferrite samples and γ-Fe$_2$O$_3$
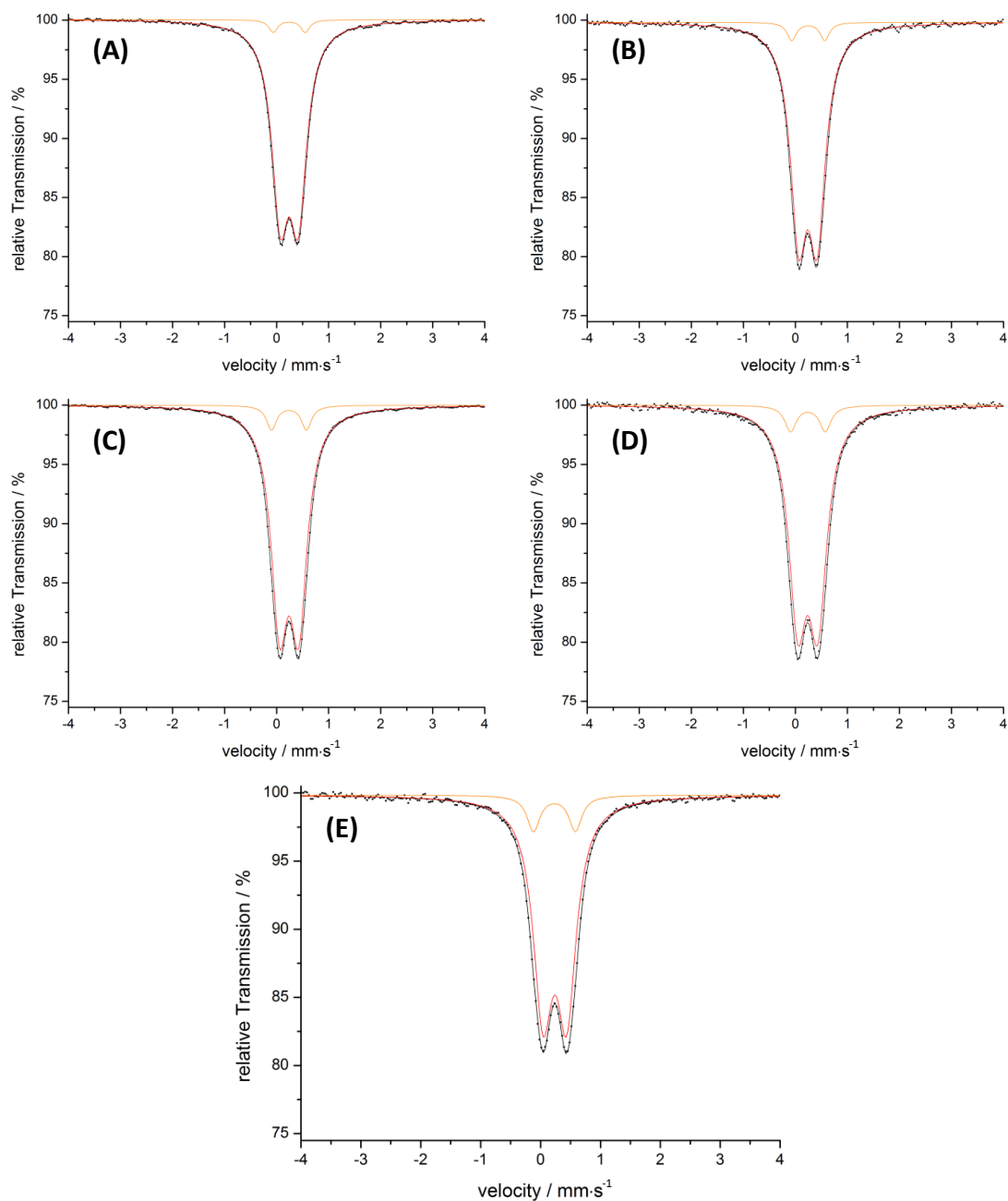
Fig. A2. Mössbauer spectra of the ZFO samples after calcination at **(A)** 773 K, **(B)** 873 K, **(C)** 973 K, **(D)** 1073 K, and **(E)** 1173 K. The black line represents the cumulative peak fit consisting of the orange and red lines.
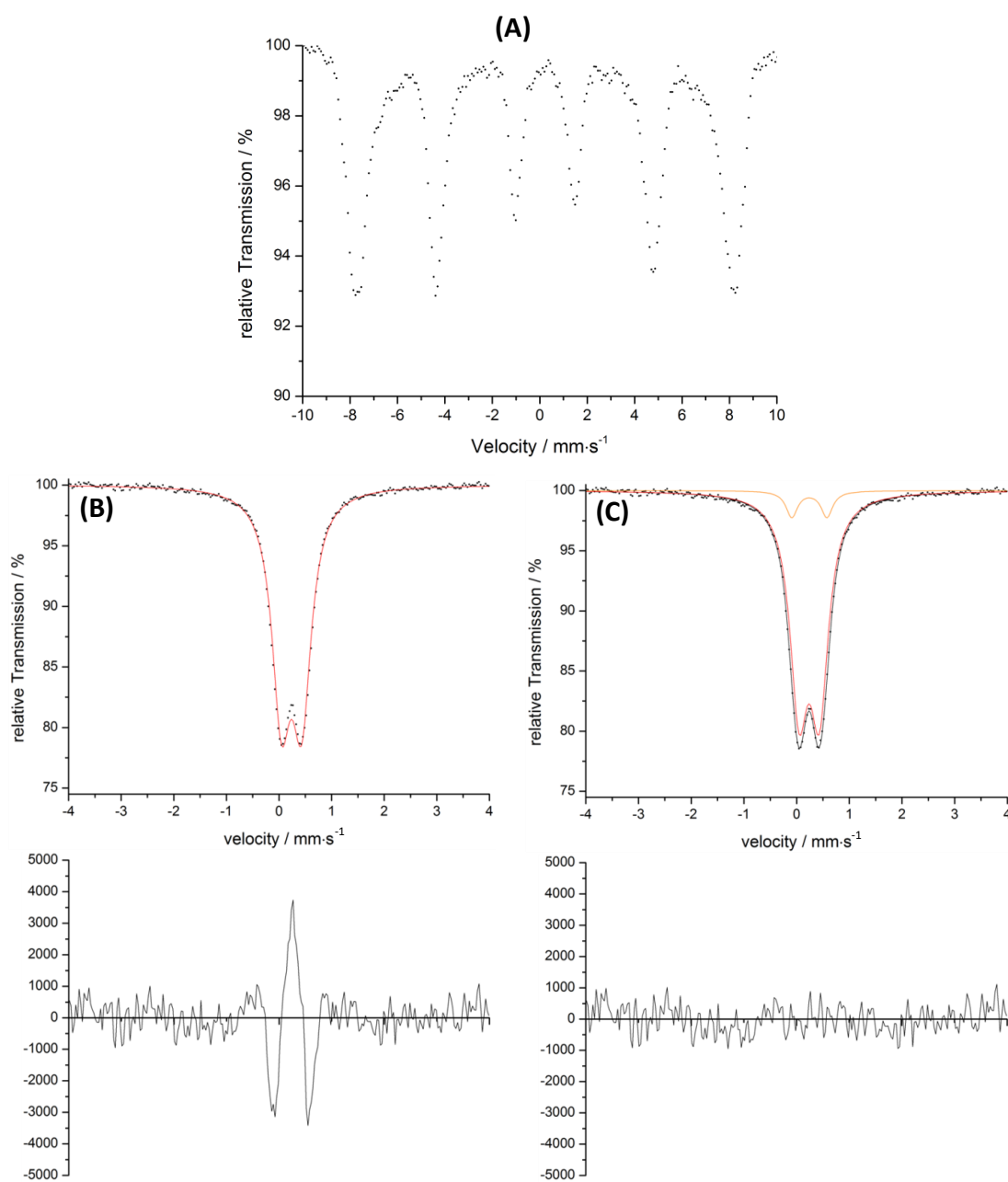
Fig. A3. **(A)** Mössbauer spectrum of a commercial γ-Fe_2O_3 sample (20-40 nm, io·li·tec). **(B-C)** Fitted Mössbauer spectrum and residual plot of ZFO_1073 obtained by considering **(B)** one and **(C)** two paramagnetic doublets. Similar results are observed for the rest of the ZFO samples.

Table A1. Mössbauer parameters of the ZFO samples with different calcination temperatures. δ_{IS}, Δ_Q, FWHM are the isomer shift, quadrupole splitting, and full width at half maximum, respectively.

Calcination temperature / K	δ_{IS} / mm·s^{-1}	Δ_Q /mm·s^{-1}	FWHM / mm·s^{-1}	Population / %
773	0.354 ± 0.001	0.344 ± 0.002	0.193 ± 0.001	96.3 ± 0.85
	0.353 ± 0.008	0.614 ± 0.023	0.103 ± 0.010	3.7 ± 0.74
873	0.352 ± 0.001	0.355 ± 0.003	0.190 ± 0.002	94.9 ± 1.2
	0.358 ± 0.009	0.634 ± 0.025	0.108 ± 0.019	5.1 ± 1.0
973	0.352 ± 0.001	0.369 ± 0.001	0.195 ± 0.001	93.2 ± 0.5
	0.349 ± 0.003	0.671 ± 0.008	0.116 ± 0.007	6.8 ± 0.5
1073	0.349 ± 0.002	0.387 ± 0.023	0.208 ± 0.006	92.2 ± 0.63
	0.352 ± 0.008	0.666 ± 0.071	0.133 ± 0.063	7.8 ± 0.58
1173	0.349 ± 0.002	0.395 ± 0.003	0.195 ± 0.003	89.5 ± 1.5
	0.343 ± 0.007	0.699 ± 0.014	0.129 ± 0.015	10.5 ± 1.4

The Mössbauer measurements were fitted by using one and two paramagnetic doublets. A comparison of the two spectra showed that a single doublet leads to a bigger deviation between the observed signals and the Lorentzian fit (Fig. A3B and A3C). Similar signals were observed by H. Ehrhardt *et al.*[1] and similar values for the isomer shift and the quadrupole splitting were obtained. The difference between the quadrupole splitting and the FWHM of the two doublets can be explained by the different lattice sites of the iron. It is well known that the quadrupole splitting of tetrahedral sites of non-magnetic spinel type oxides are larger compared to the octahedral sites.[2,3] Furthermore, the tetrahedral sites show different bond length and a smaller distribution compared to the octahedral sites in the crystals which leads to smaller influence of surface defects and therefore smaller values for the FWHM which are still bigger than the natural line width.

Configurational entropy of zinc ferrite

Considering that the change in the non-configurational entropy associated with the disordering process is negligible,[4] the total entropy is defined by the configurational entropy (S_C) alone.

$$S_C = -R \sum_{s=1}^{2} \sum_{i=1}^{2} b^s N_i^s ln N_i^s \tag{A.1}$$

$$S_C = -R \left[x \ln x + (1 - x) \ln(1 - x) + (2 - x) \ln \left(1 - \frac{x}{2} \right) + x \ln \frac{x}{2} \right] \tag{A.2}$$

where N_i^s is the fraction of species i (i = 1 for Fe and i = 2 for Zn) in site s (s = 1 for tetrahedral sites and s = 2 for octahedral sites), b^s is the number of sites of type s per formula unit, and x is the degree of inversion. From a plot of S_C vs. x (Fig. A4) it can be seen that S_c tends to 0 at x = 0, increases to a maximum at the random arrangement of x = 2/3, and then decreases towards $2R \ln 2$ for x = 1. The change in the Gibbs free energy for the disordering process, ΔG_D°, is defined as

$$\Delta G_D^\circ = \Delta H_D^\circ - T\Delta S_C^\circ \tag{A.3}$$

where ΔH_D° and ΔS_D° are the changes in enthalpy and entropy, respectively, associated with the cation distribution process, and T is the temperature. Since S_C° = 0 when x = 0, then:

$$\Delta S_C^\circ = S_C = -R \left[x \ln x + (1 - x) \ln(1 - x) + x \ln \frac{x}{2} + (2 - x) \ln \left(1 - \frac{x}{2} \right) \right] \tag{A.4}$$

Considering that ΔH_D° is T and x independent, it is clear that at high temperatures the process becomes entropy dependent and the degree of inversion increases towards the maximum of x = 2/3. O'Neill and Navrotsky[5,6] showed, from lattice energy arguments, that ΔH_D° depends linearly on x. Nevertheless, it also emerges from this more comprehensive model that the degree of inversion increases with higher calcination temperatures, as is observed from the experimental results.
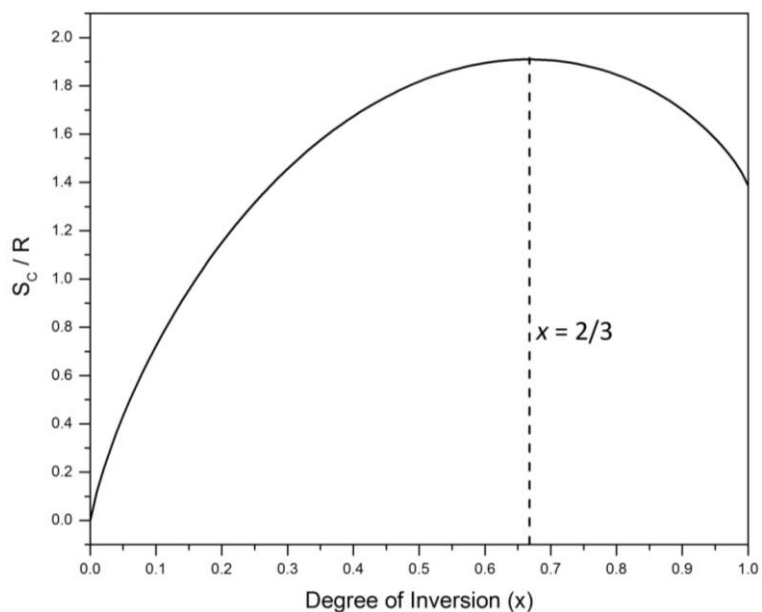
Fig. A4. Plot of the configurational entropy, S_C, of ZFO vs. the degree of inversion, x. S_c tends to 0 at $x = 0$, increases to a maximum at the random arrangement of $x = 2/3$, and then decreases towards $2R \ln 2$ for $x = 1$.

Raman spectra of zinc ferrite samples
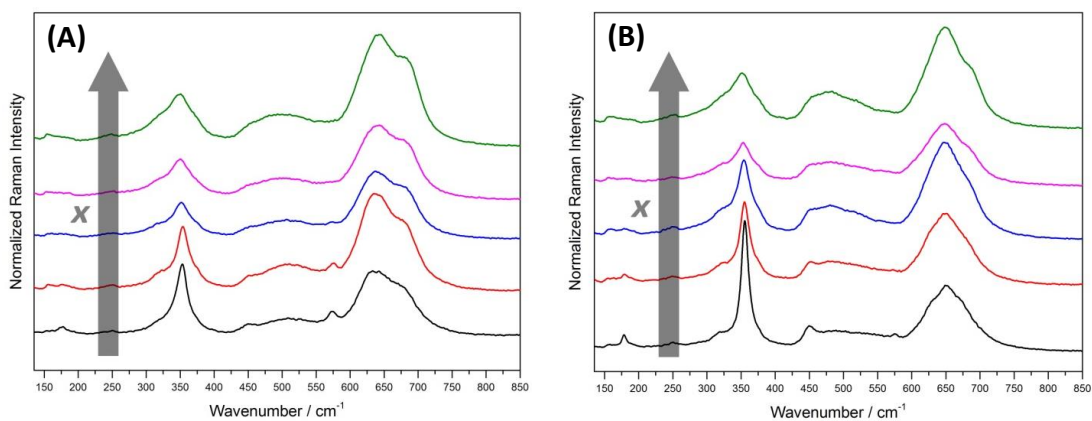
Fig. A5. Normalized Raman spectra of the ZFO samples with increasing degree of inversion (— ZFO_773, $x = 0.074 \pm 0.011$; — ZFO_873, $x = 0.104 \pm 0.013$; — ZFO_973, $x = 0.134 \pm 0.008$; — ZFO_1073, $x = 0.159 \pm 0.010$; — ZFO_1173, $x = 0.203 \pm 0.017$) obtained using **(A)** a 532 nm and **(B)** a 633 nm laser as the excitation source.

Comparison between the Raman spectra of zinc ferrite ($x \approx 0.073$) and of γ-Fe$_2$O$_3$
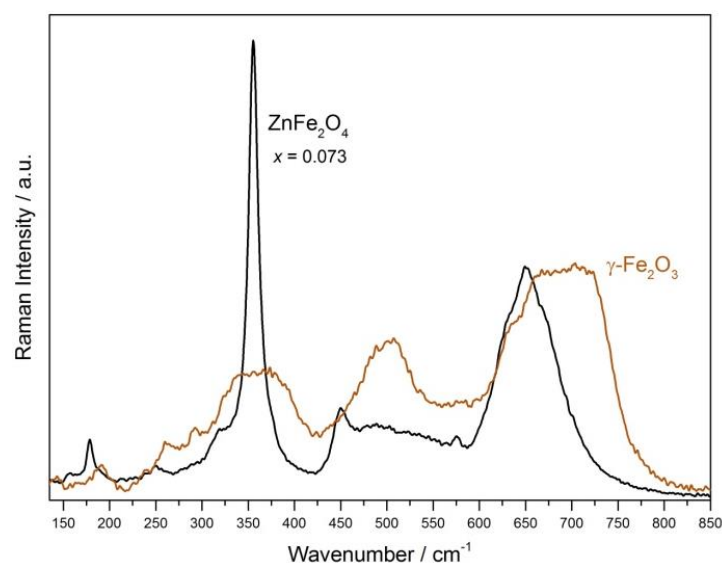
Fig. A6. Raman spectrum of a commercial γ-Fe$_2$O$_3$ sample (brown line) obtained using a 633 nm laser excitation. The Raman spectrum of ZFO_773 (black line) is included for comparison. Although most of the ZFO and γ-Fe$_2$O$_3$ Raman scattering signals are superimposed, the absence of a shoulder at ca. 718 cm^{-1} in the ZFO spectrum proves that γ-Fe$_2$O$_3$ is not present as an impurity phase.

Deconvolution of the broad Raman signal at 647 ± 3 cm^{-1}
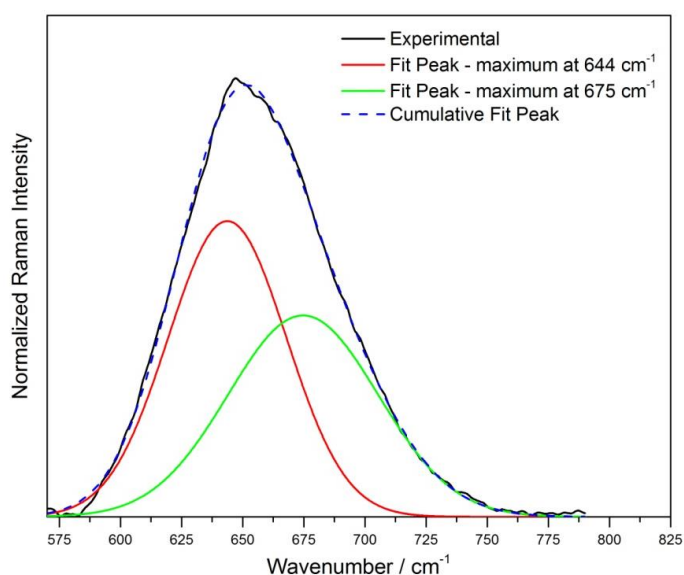
Fig. A7. Deconvolution of the broad Raman signal at 647 ± 3 cm^{-1} (785 nm laser excitation) using Gaussian-shape curves with maxima located at ca. 644 cm^{-1} and 675 cm^{-1}.

Correlation between intensity of the Raman signals and the degree of inversion

The intensity ratio between the Raman signals serves as a reference to estimate the degree of inversion of ZFO samples. Fig. A8 shows plots of the intensity ratio between the Raman shifts at 352 and 647 cm^{-1} (measured using a 785 nm, A, 633 nm, B, and 532 nm, C, laser as the excitation sources) as a function of the degree of inversion. The experimental data were fitted using an exponential decay function. To ascertain the validity of this empirical equation, the intensity ratio between the shifts at 352 and 647 cm^{-1} of a Raman spectrum presented by Wang *et al.*[7] was analyzed. For the ZFO sample with a reported degree of inversion of 0.10, a ratio of 3.02 was calculated. With this ratio and the equation given in Fig. A8, a degree of inversion of 0.12 ± 0.03 was calculated, thus being in reasonable agreement with the value give by Wang *et al*.
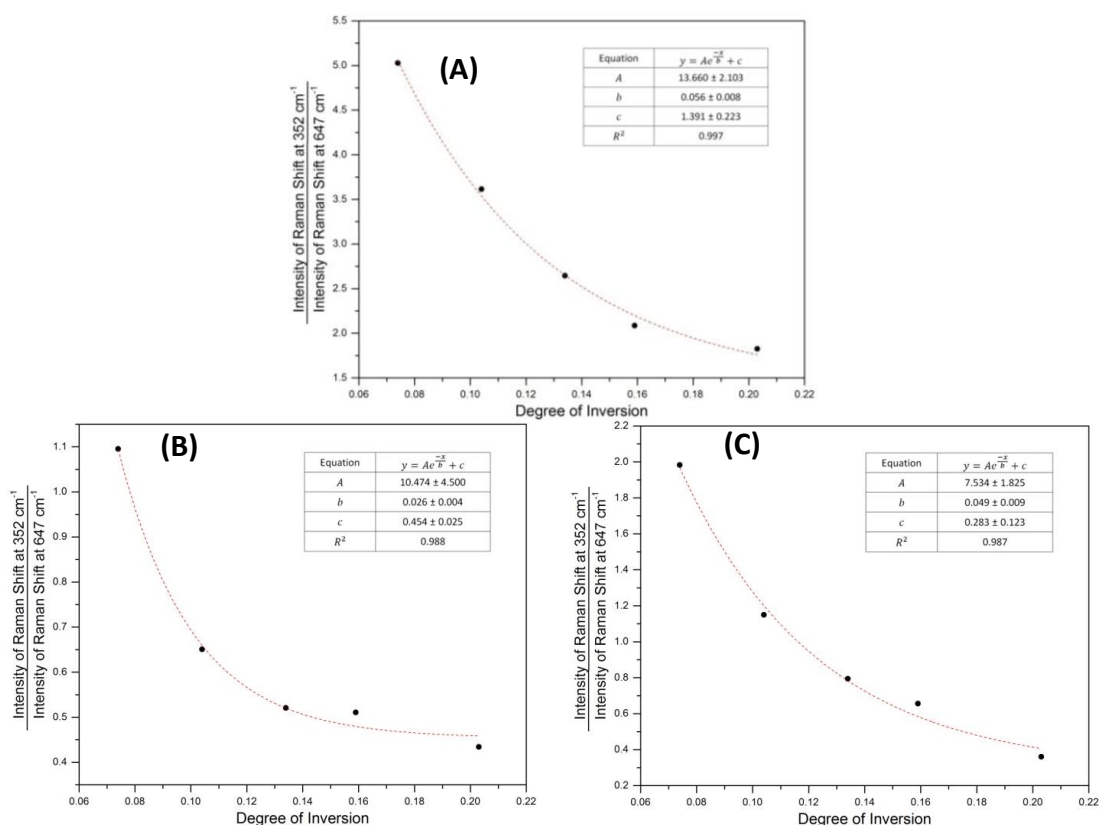
Fig. A8. Intensity ratio between the Raman shifts at 352 and 647 cm^{-1} (measured using **(A)** a 785 nm, **(B)** a 633 nm, and **(C)** a 532 nm laser as the excitation source) as a function of the degree of inversion. The insert shows the parameters of the exponential decay function used to fit the experimental data.

Photograph of zinc ferrite samples

Fig. A9. Photograph of the ZFO samples with different degrees of inversion (x = 0.074 ± 0.011, 0.104 ± 0.013, 0.134 ± 0.008, 0.159 ± 0.010, and 0.203 ± 0.017 for ZFO_773, ZFO_873, ZFO_973, ZFO_1073, and ZFO_1173, respectively). As the degree of inversion increases, the brownish orange color of the samples becomes gradually darker.

Identification and prediction of electronic transitions of zinc ferrite
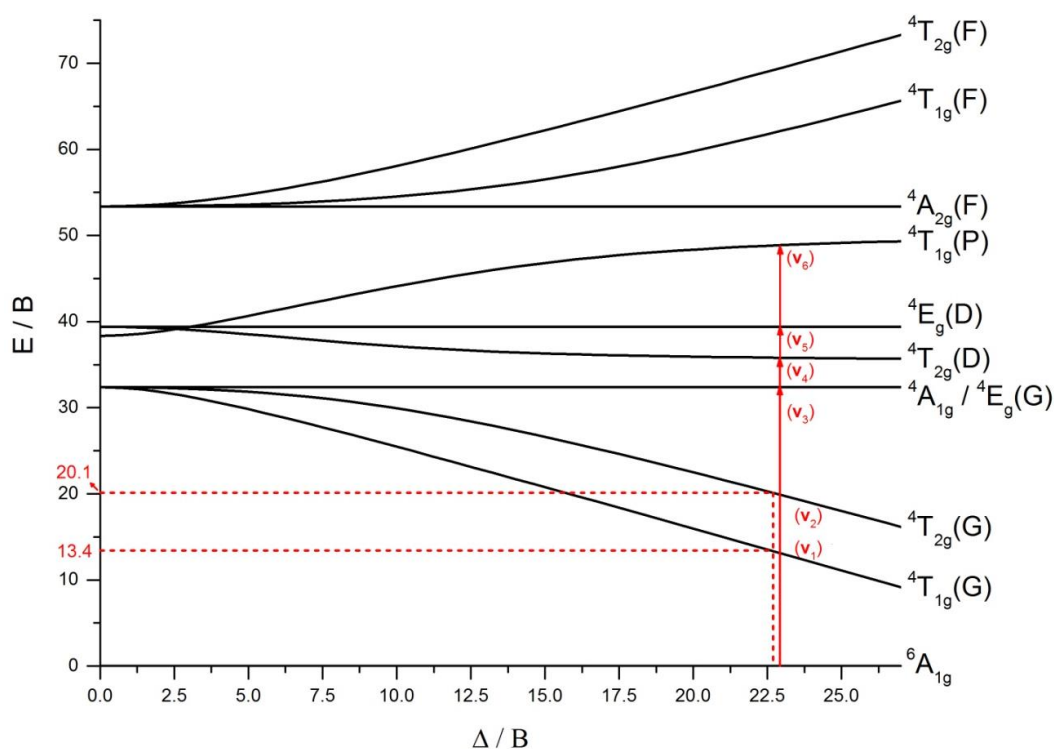
Fig. A10. Partial Tanabe-Sugano diagram for a high spin d^5 ion with octahedral symmetry. Only the excited states with spin multiplicity 4 are shown.

From an analysis based on the Tanabe-Sugano diagram for high spin d^5 octahedrally coordinated Fe^{3+} ions it is possible to obtain important parameters such as energy of the crystal field, Δ, for the FeO_6 octahedra and the Racah

parameter. Moreover, predictions concerning the possible electronic transitions can be done.

The bands observed experimentally at 1200 nm (8333.3 cm^{-1}) and 795 nm (12578.6 cm^{-1}) can be assigned to the $^6A_{1g} \rightarrow {}^4T_{1g}(G)$ (v_1) and $^6A_{1g} \rightarrow {}^4T_{2g}(G)$ (v_2) transitions, respectively. The ration between the energy of these transitions is:

$$\frac{v_2}{v_1} = \frac{12578.6\ cm^{-1}}{8333.3\ cm^{-1}} \approx 1.5 \tag{A.5}$$

A theoretical ratio of 1.5 between the energy of transitions v_2 and v_1 is observed in the Tanabe-Sugano diagram at a value of Δ/B of 22.7.

$$\frac{\Delta}{B} = 22.7 \ \rightarrow \ \frac{E_{v_2}/B}{E_{v_1}/B} = \frac{E_{v_2}}{E_{v_1}} = \frac{20.1}{13.4} = 1.5 \tag{A.6}$$

where E_{v_1} and E_{v_2} are the energies of transitions v_1 and v_2, respectively, and B is the Racah parameter. B can be calculated as:

$$\frac{E_{v_2}}{B} = 20.1 \rightarrow B = \frac{12578.6\ cm^{-1}}{20.1} \approx 626\ cm^{-1} \tag{A.7}$$

$$\frac{E_{v_1}}{B} = 13.4 \rightarrow B = \frac{8333.3\ cm^{-1}}{13.4} \approx 622\ cm^{-1} \tag{A.8}$$

obtaining an average value of 624 cm^{-1}. The energy of the crystal field, Δ, can be obtained from:

$$\frac{\Delta}{B} = 22.7 = \frac{\Delta}{624 cm^{-1}} \rightarrow \Delta \approx 14164 cm^{-1} \tag{A.9}$$

Finally, the energy of transitions v_3, v_4, v_5, and v_6 can be predicted from the Tanabe-Sugano diagram. The following values are obtained for these transitions:

Transition	Energy
$^6A_{1g} \rightarrow {}^4A_{1g}(G)$ (v_3)	20248 cm^{-1} (494 nm / 2.51 eV)
$^6A_{1g} \rightarrow {}^4T_{2g}(D)$ (v_4)	22300 cm^{-1} (448 nm / 2.76 eV)
$^6A_{1g} \rightarrow {}^4E_g(D)$ (v_5)	24592 cm^{-1} (407 nm / 3.05 eV)
$^6A_{1g} \rightarrow {}^4T_{1g}(P)$ (v_6)	30445 cm^{-1} (328 nm / 3.8 eV)

Application of DASF method to diffuse reflectance measurements

According to the absorption spectrum fitting (ASF) presented by Souri and Shomalian:[8,9]

$$\alpha = B(hc)^{m-1}\lambda\left(\frac{1}{\lambda} - \frac{1}{\lambda_g}\right)^m \tag{A.10}$$

where α is the absorption coefficient, λ is the wavelength, B is an empirical constant, h is Plank's constant, c is the velocity of light, λ_g is the wavelength corresponding to the optical band gap, and m is the index which can have different values (1/2, 2/3, 2, or 3) according to the type of transition.

The absorption coefficient α is related to the reflectance of a sample by the Kubelka-Munk radiative transfer model:[10]

$$f(R) = \frac{(1-R)^2}{2R} = \frac{\alpha}{s} \tag{A.11}$$

$$\alpha = f(R)\,s \tag{A.12}$$

where $f(R)$ is the Kubelka-Munk function, R is the reflectance, and s is the scattering coefficient.

By combining Eq. (A.10) and (A.12):

$$f(R)s = B(hc)^{m-1}\lambda\left(\frac{1}{\lambda} - \frac{1}{\lambda_g}\right)^m \tag{A.13}$$

and considering that s is wavelength independent, the DASF method is deduced as follows:

$$\frac{f(R)s}{\lambda} = B(hc)^{m-1}\left(\frac{1}{\lambda} - \frac{1}{\lambda_g}\right)^m \tag{A.14}$$

$$\ln\left[\frac{f(R)s}{\lambda}\right] = \ln\left[B(hc)^{m-1}\lambda\left(\frac{1}{\lambda} - \frac{1}{\lambda_g}\right)^m\right] \tag{A.15}$$

$$\ln\left[\frac{f(R)}{\lambda}\right] + \ln s = \ln[B(hc)^{m-1}] + m\ln\left(\frac{1}{\lambda} - \frac{1}{\lambda_g}\right) \tag{A.16}$$

$$d\left\{\ln\left[\frac{f(R)}{\lambda}\right] + \ln s\right\} = d\left\{\ln[B(hc)^{m-1}] + m\ln\left(\frac{1}{\lambda} - \frac{1}{\lambda_g}\right)\right\} \tag{A.17}$$

$$d\left\{\ln\left[\frac{f(R)}{\lambda}\right]\right\} = d\left\{m\ln\left(\frac{1}{\lambda} - \frac{1}{\lambda_g}\right)\right\} \tag{A.18}$$

$$d\left\{\ln\left[\frac{f(R)}{\lambda}\right]\right\} = \frac{m}{\left(\frac{1}{\lambda} - \frac{1}{\lambda_g}\right)}d\left(\frac{1}{\lambda}\right) \tag{A.19}$$

$$\frac{d\left\{\ln\left[\frac{f(R)}{\lambda}\right]\right\}}{d\left(\frac{1}{\lambda}\right)} = \frac{m}{\left(\frac{1}{\lambda} - \frac{1}{\lambda_g}\right)} \tag{A.20}$$

Eq. (A.20) is the DASF equivalent for diffuse reflectance measurements. However, $f(R)$ can only be used instead of α when a wavelength independent scattering coefficient is assumed.
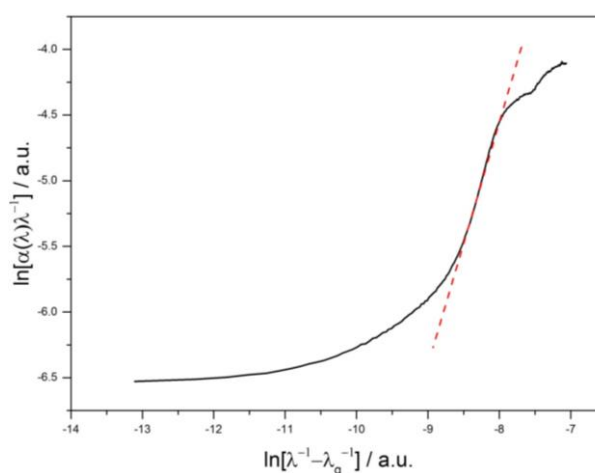
SEM pictures of the ZFO samples

126
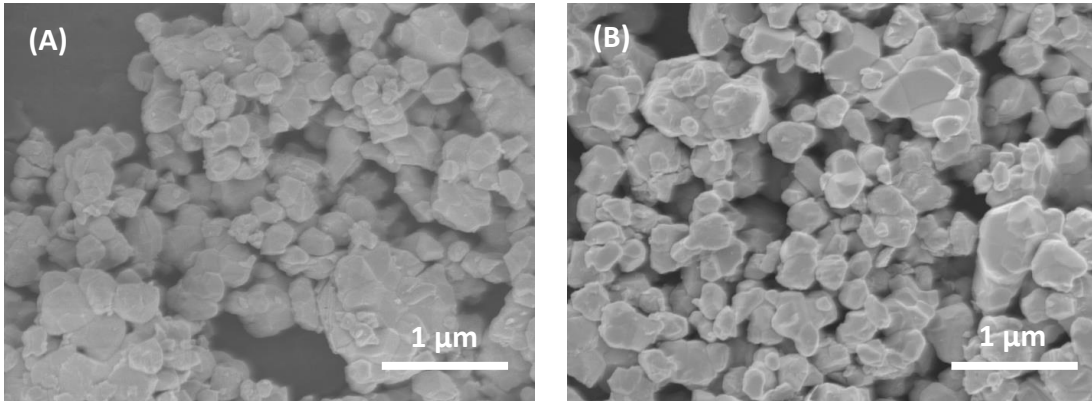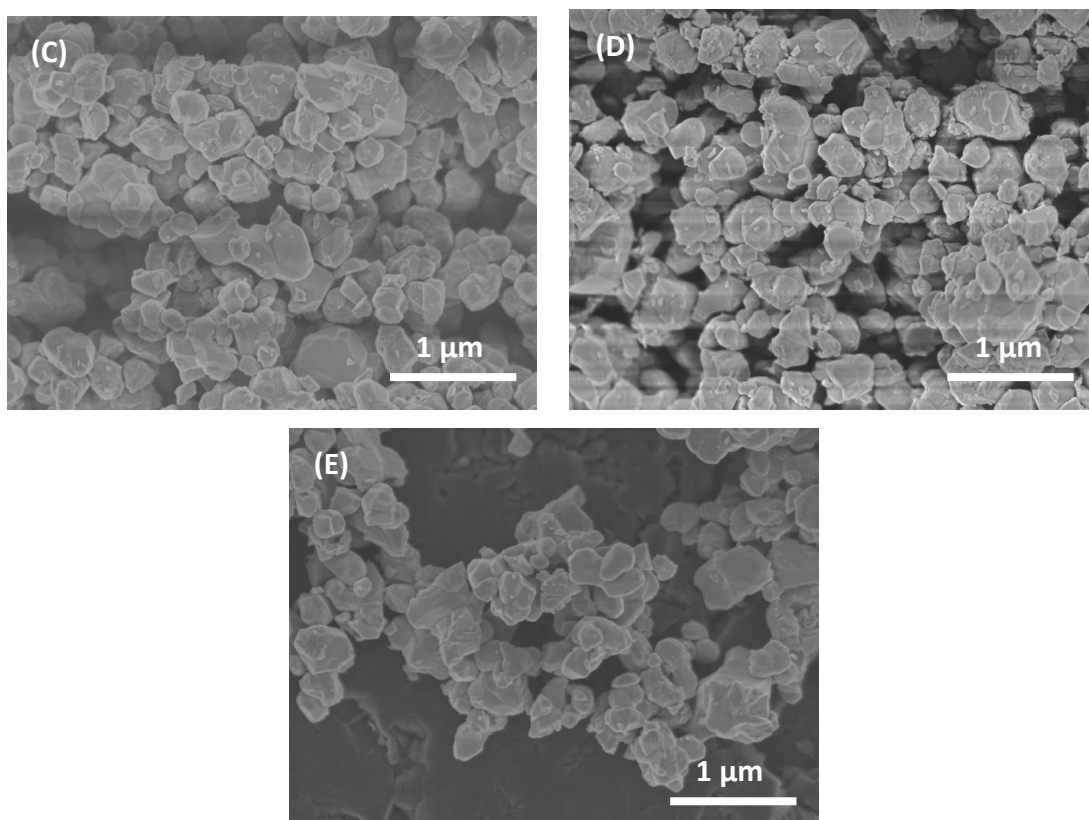
Fig. A11. SEM images of the ZFO samples after calcination at **(A)** 773 K, **(B)** 873 K, **(C)** 973 K, **(D)** 1073 K, and **(E)** 1173 K. Similar particle size and morphology are observed between the samples annealed at different temperatures.

DASF analysis of zinc ferrite sample with *x* = 0.074 ± 0.011

Fig. A12. Plot of $\ln[\alpha(\lambda)\lambda^{-1}]$ versus $\ln(\lambda^{-1} - \lambda_g^{-1})$ for the ZFO sample with *x* = 0.074 ± 0.011. λ_g = 614 nm is the wavelength of the band gap transition. The value of the slope of the linear section of the graph indicates the nature of the optical carrier transition. A slope of 1.95 (≈ 2) is observed for the red dashed line, indicating an indirect allowed band gap. Identical results are found for the samples quenched at higher temperatures.

References

(1)   H. Ehrhardt, S. J. Campbell and M. Hofmann, Structural Evolution of Ball-Milled $ZnFe_2O_4$, *J. Alloys Compd.* **2002**, 339, 255–260.

(2)   F. Grandjean, G. J. Long, G. Longworth and B. J. Laundy, Iron-57 and Antimony-121 Mössbauer-Effect Study of Several Spinel Antimonates, *Inorg. Chem.* **1984**, 23, 1886–1895.

(3)   T. Mizoguchi and M. Tanaka, The Nuclear Quadrupole Interaction of Fe^{57} in Spinel Type Oxides, *J. Phys. Soc. Japan* **1963**, 18, 1301–1306.

(4)   A. Navrotsky and O. J. Kleppa, The Thermodynamics of Cation Distributions in Simple Spinels, *J. Inorg. Nucl. Chem.* **1967**, 29, 2701–2714.

(5)   H. S. C. O'Neill and A. Navrotsky, Simple Spinels: Crystallographic Parameters, Cation Radii, Lattice Energies, and Cation Distribution, *Am. Mineral.* **1983**, 68, 181–194.

(6)   H. S. C. O'Neill and A. Navrotsky, Cation Distributions and Thermodynamic Properties of Binary Spinel Solid Solutions, *Am. Mineral.* **1984**, 69, 733–753.

(7)   Z. Wang, D. Schiferl, Y. Zhao and H. S. C. O'Neill, High Pressure Raman Spectroscopy of Spinel-Type Ferrite $ZnFe_2O_4$, *J. Phys. Chem. Solids* **2003**, 64, 2517–2523.

(8)   D. Souri and K. Shomalian, Band Gap Determination by Absorption Spectrum Fitting Method (ASF) and Structural Properties of Different Compositions of $(60-x)V_2O_5$-$40TeO_2$-xSb_2O_3 Glasses, *J. Non. Cryst. Solids* **2009**, 355, 1597–1601.

(9)   D. Souri and Z. E. Tahan, A New Method for the Determination of Optical Band Gap and the Nature of Optical Transitions in Semiconductors, *Appl. Phys. B* **2015**, 119, 273–279.

(10)   P. Kubelka, New Contributions to the Optics of Intensely Light-Scattering Materials. Part I, *J. Opt. Soc. Am.* **1948**, 38, 448–547.

Appendix B: Supporting information for Chapter 3: Effect of the Degree of Inversion on the Electrical Conductivity of Spinel ZnFe$_2$O$_4$

Experimental methods

Polycrystalline ZFO samples were synthesized by means of a solid-state reaction as was reported in Ref. 1. Shortly, stoichiometric amounts of ZnO (Sigma Aldrich, ≥ 99.0%) and Fe$_2$O$_3$ (Sigma Aldrich, ≥ 99.0%) powders were ground in an agate mortar. The mixture was calcined in air at 1073 K for 12 hours, cooled down to room temperature, and ground once again. Aliquots of 0.500 g were pressed into 13 mm diameter pellets applying a pressure of 55 MPa. The pellets were calcined at 1273 K for 2 hours, cooled down to 1073 K and kept at this temperature for 12 hours, then cooled down to 773 K and kept at this temperature for 50 hours, and finally quenched in cold water. Some of the pellets (referred as ZFO_773) were separated and the rest were divided into four sets of samples. The samples were heated up with a rate of 300 K h^{-1} and calcined at 873, 973, 1073, and 1173 K for 25, 20, 12, and 10 hours, respectively. After this period of time, the calcined pellets were immediately quenched in cold water. These samples will be referred as ZFO_873, ZFO_973, ZFO_1073, and ZFO_1173.

Impedance spectra were measured with a Novocontrol Concept 41 equipped with an Alpha-A High-Performance Modular Measure System and a Novocool Cryosystem (Novocontrol Technologies, Germany). The measurements were performed in a nitrogen atmosphere at temperature intervals of 25 K from 298 K to 448 K. A frequency range of 10 MHz to 100 mHz and a difference of 100 mV in potential were used for the measurements. The ZFO pellets were sanded with Al$_2$O$_3$ sandpaper (KK114F, grit size P320, VSM Abrasives, Germany) to a final thickness of 0.75 mm ± 0.02 mm and attached in a sandwich configuration between two 20 mm diameter gold-plated electrodes using graphite conductive adhesive (186 Ω cm^{-2} sheet resistance @ 25.4 μm in thickness, Alfa Aesar, Germany). The capacitance of the sample holder alone was equal to 1.0 pF and all the impedance

measurements were corrected to this value. The EIS Spectrum Analyser software[2] was used for fitting the obtained impedance spectra.
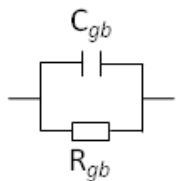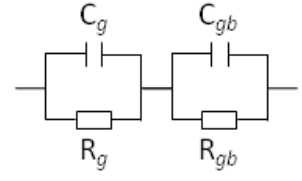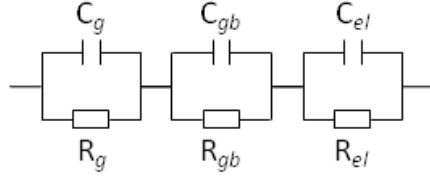
XRDs and Mössbauer spectra of the zinc ferrite samples
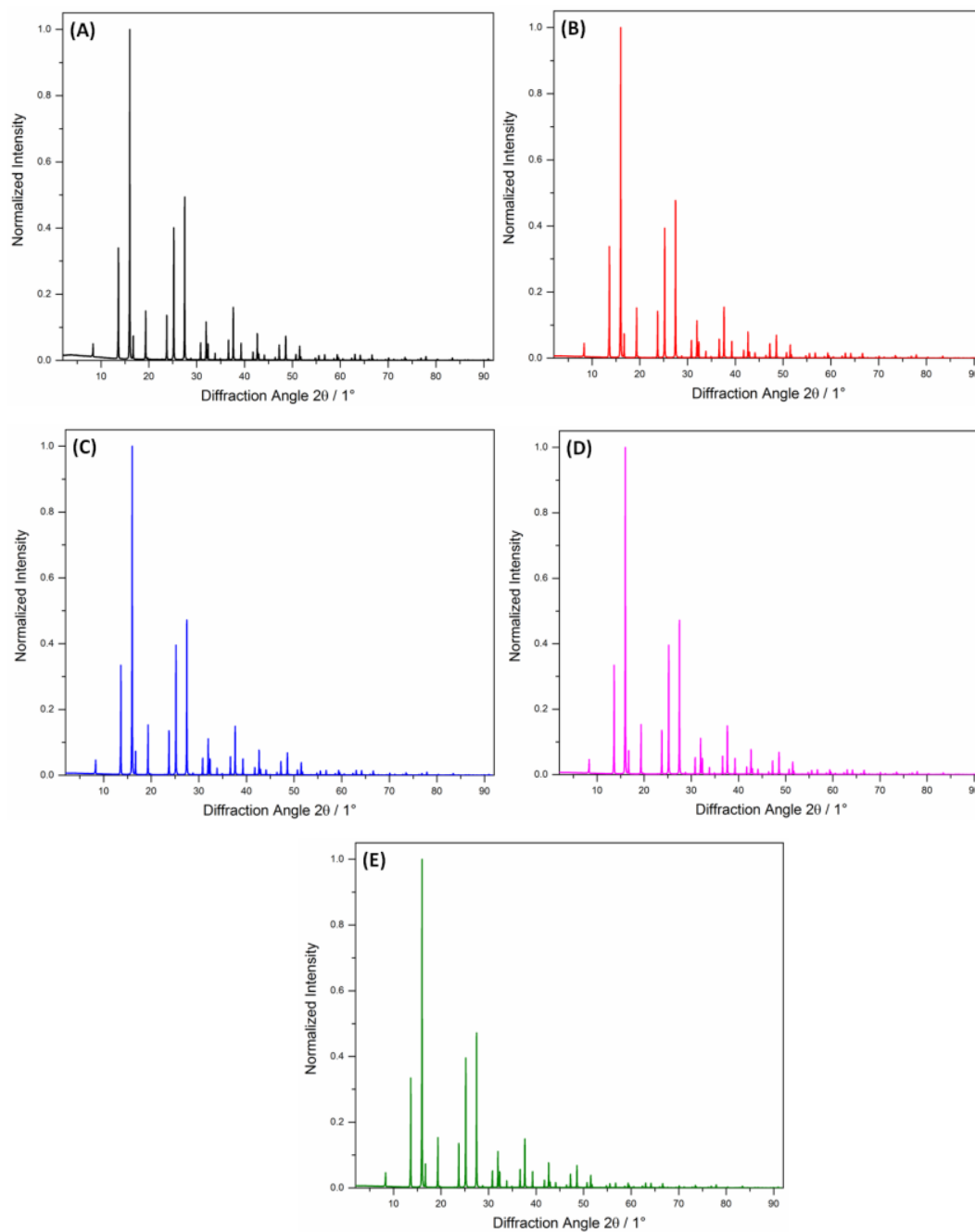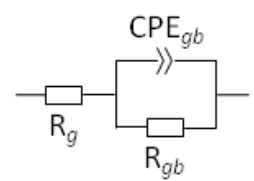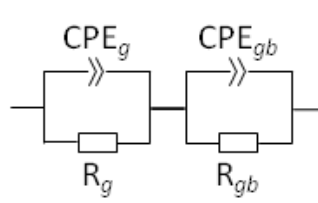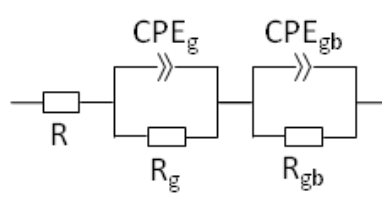

Fig. B1. XRDs of the ZFO samples after calcination at **(A)** 773 K, **(B)** 873 K, **(C)** 973 K, **(D)** 1073 K, and **(E)** 1173 K. Details are given in Ref. 1.
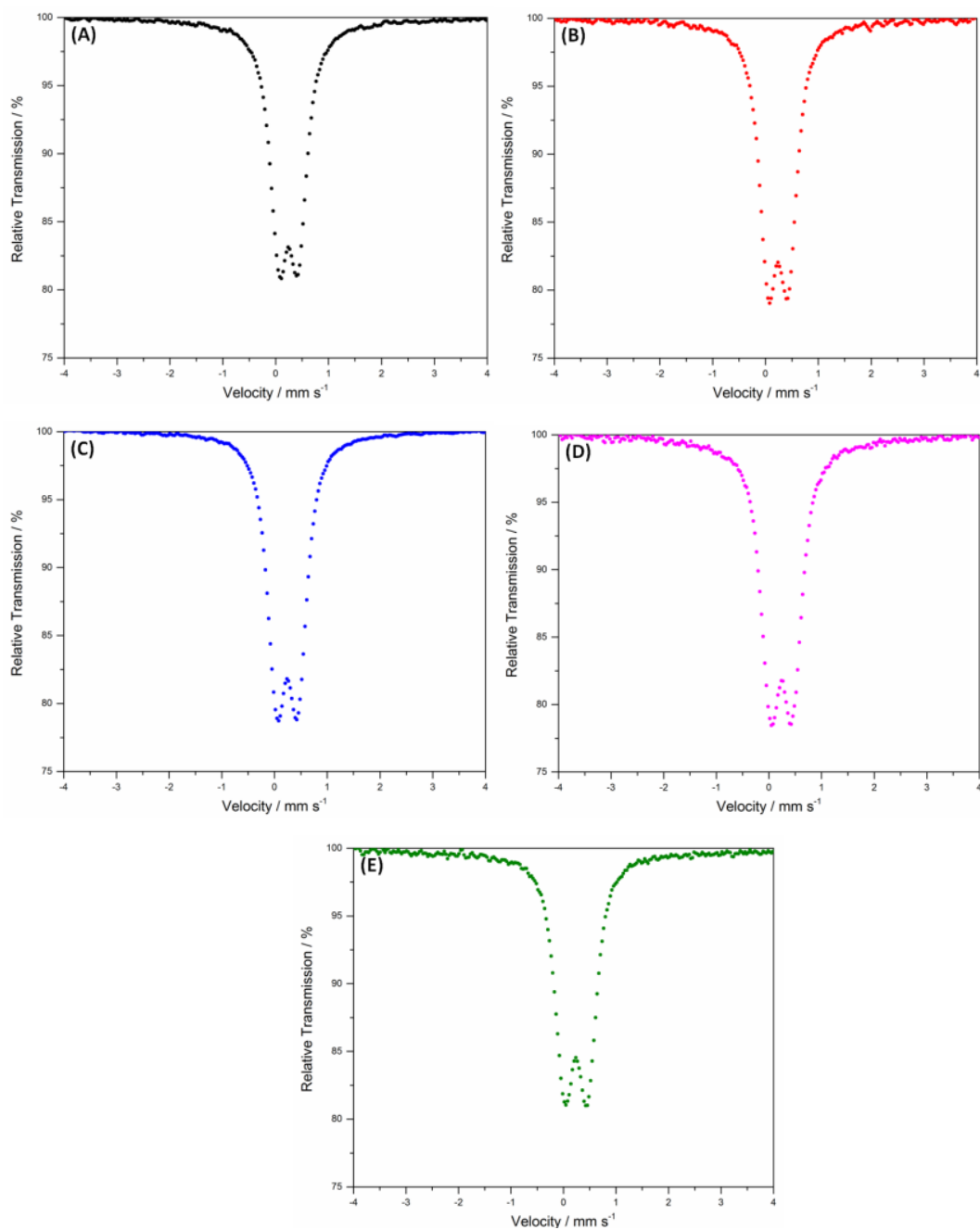
Fig. B2. Mössbauer spectra of the ZFO samples after calcination at **(A)** 773 K, **(B)** 873 K, **(C)** 973 K, **(D)** 1073 K, and **(E)** 1173 K. Details are given in Ref. 1.

Comparison of equivalent circuits commonly used for modeling the impedance spectra of spinel ferrite samples

Table B1. Overview over the equivalent circuits commonly used to model the impedance spectra of spinel ferrite materials. The C, R, and CPE elements are capacitors, resistors, and constant phase elements, respectively. The subscripts "*gb*", "*g*", and "*el*" denote the grain boundaries, the grains (bulk), and sample-electrode interface, respectively.

| Equivalent Circuit		Ferrite	Reference
I		$ZnFe_2O_4$	3
		$Zn_{0.5}Ni_{0.5}Fe_2O_4$	3
II		$ZnFe_2O_4$	4
		$Mn_{0.68}Zn_{0.26}Fe_{2.06}O_4$	5
		$(Ni_xZn_{1-x})Fe_2O_4$ $(0.2 \leq x \leq 0.5)$	6
		$Ni_{0.5}Zn_{0.5}Fe_2O_4$	7, 8
III		$ZnFe_2O_4$	9
		$(Mn_xZn_{1-x})Fe_2O_4$ $(0 \leq x \leq 1)$	10
IV		$MnFe_2O_4$	11
		$Ni_{0.65}Zn_{0.35}Fe_2O_4$	12
V		$ZnFe_2O_4$	13
		$NiFe_2O_4$	14
VI		$Ni_{0.65}Zn_{0.35}Fe_2O_4$	12

The Fig. B3–B5 show the modeling of the impedance spectra obtained at 298 K for the ZFO sample with x = 0.074 ± 0.011 by three of the equivalents circuits presented in Table B1 (Equivalent circuits I – III).
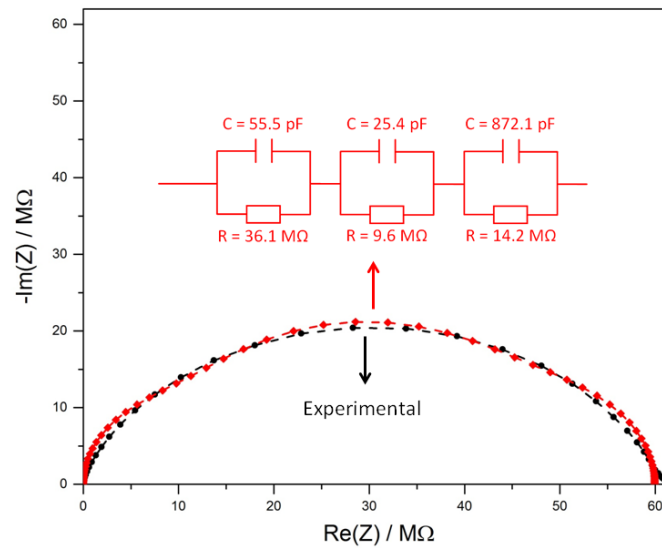
Equivalent Circuit I
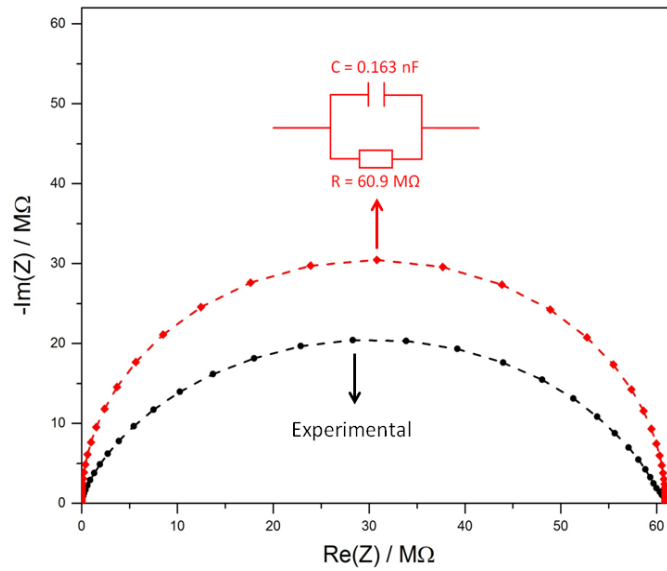
Fig. B3. Modeling of the impedance data using a simple equivalent circuit consisting of a resistor and a capacitor connected in parallel.
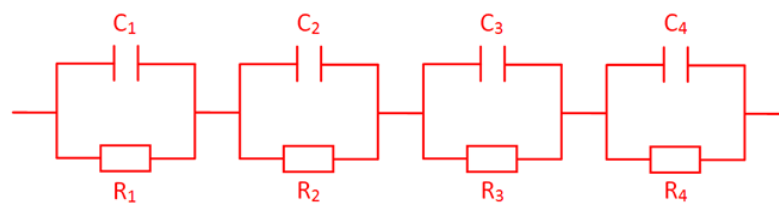
Equivalent Circuit II
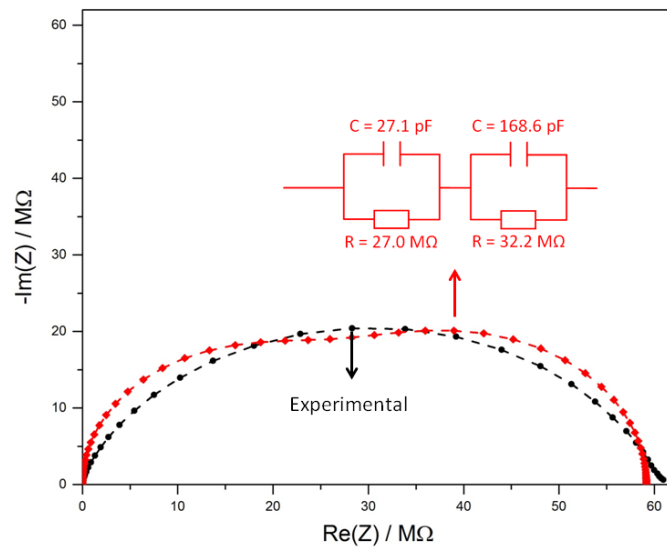
Fig. B4. Fitting of the impedance data using an equivalent circuit consisting of a series connection of two R‖C elements.

Equivalent Circuit III

C = 55.5 pF   C = 25.4 pF   C = 872.1 pF

R = 36.1 MΩ   R = 9.6 MΩ   R = 14.2 MΩ

Experimental
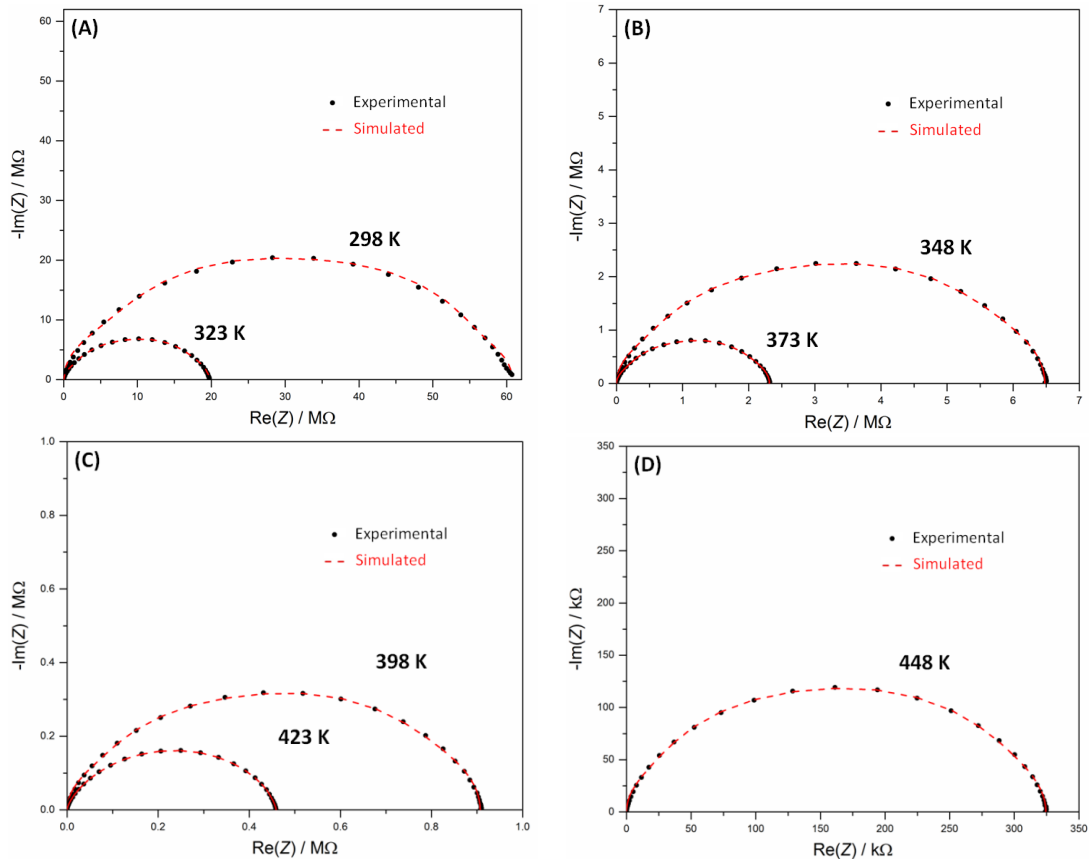
Fig. B5. Fitting of the impedance data using an equivalent circuit consisting of a series connection of three R‖C elements.

Results obtained for the modeling of the impedance spectra using an equivalent circuit with four R‖C elements connected in series

C_1 C_2 C_3 C_4

R_1 R_2 R_3 R_4

Fig. B6. Equivalent circuit proposed in this work.

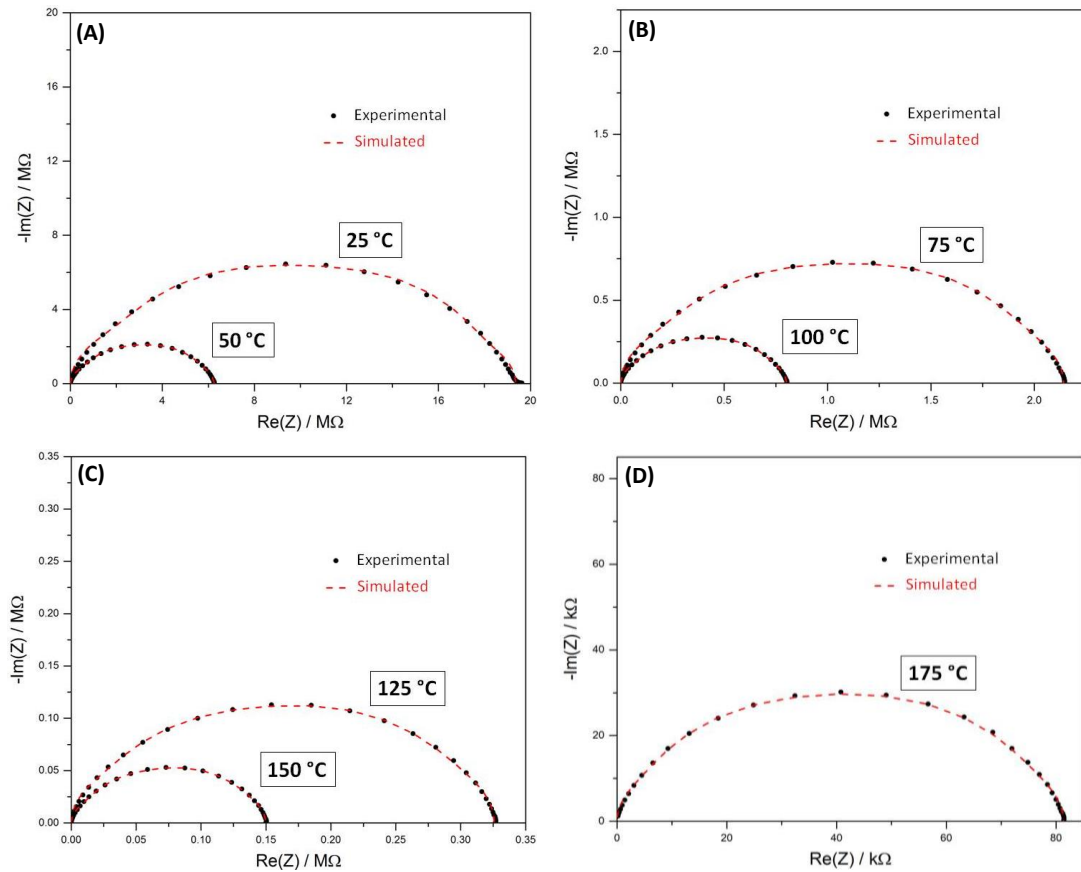*ZFO sample with x = 0.074 ± 0.011 (ZFO_773)*

Fig. B7. Experimental (black spots) and calculated (red dashed line) complex impedance data obtained at **(A)** 298 K and 323 K, **(B)** 348 K and 373 K, **(C)** 398 K and 423 K, and **(D)** 448 K for a ZFO sample with x = 0.074 ± 0.011. The complex impedance data was simulated using the equivalent circuit shown in Fig. B6.

Table B2. Parameters of the elements of the equivalent circuit (Fig. B6) used for the fitting of the complex impedance data obtained for a ZFO sample with $x = 0.074 \pm 0.011$ (Fig. B7). The bulk capacitance ($C_g = C_2$) and resistance ($R_g = R_2$) are highlighted in yellow.

Equivalent Circuit Element	Temperature / °C						
	25	**50**	**75**	**100**	**125**	**150**	**175**
C_1 / F	$9.86\ 10^{-9}$	$2.97\ 10^{-9}$	$2.52\ 10^{-9}$	$2.34\ 10^{-9}$	$2.23\ 10^{-9}$	$3.41\ 10^{-9}$	$3.04\ 10^{-9}$
C_2 / F	$2.82\ 10^{-11}$	$2.88\ 10^{-11}$	$2.83\ 10^{-11}$	$2.81\ 10^{-11}$	$2.79\ 10^{-11}$	$2.85\ 10^{-11}$	$3.43\ 10^{-11}$
C_3 / F	$4.76\ 10^{-11}$	$4.36\ 10^{-11}$	$4.16\ 10^{-11}$	$3.96\ 10^{-11}$	$3.88\ 10^{-11}$	$4.26\ 10^{-11}$	$3.69\ 10^{-11}$
C_4 / F	$2.22\ 10^{-10}$	$1.33\ 10^{-10}$	$1.22\ 10^{-10}$	$1.16\ 10^{-10}$	$1.12\ 10^{-10}$	$1.28\ 10^{-10}$	$1.10\ 10^{-10}$
R_1 / Ω	$4.64\ 10^{6}$	$2.23\ 10^{6}$	$7.62\ 10^{5}$	$2.70\ 10^{5}$	$1.04\ 10^{5}$	$4.47\ 10^{4}$	$2.89\ 10^{4}$
R_2 / Ω	$6.25\ 10^{6}$	$1.54\ 10^{6}$	$5.03\ 10^{5}$	$1.81\ 10^{5}$	$7.16\ 10^{4}$	$3.61\ 10^{4}$	$2.21\ 10^{4}$
R_3 / Ω	$2.61\ 10^{7}$	$6.90\ 10^{6}$	$2.23\ 10^{6}$	$8.01\ 10^{5}$	$3.14\ 10^{5}$	$1.64\ 10^{5}$	$1.24\ 10^{5}$
R_4 / Ω	$2.38\ 10^{7}$	$9.01\ 10^{6}$	$2.98\ 10^{6}$	$1.06\ 10^{6}$	$4.16\ 10^{5}$	$2.13\ 10^{5}$	$1.49\ 10^{5}$

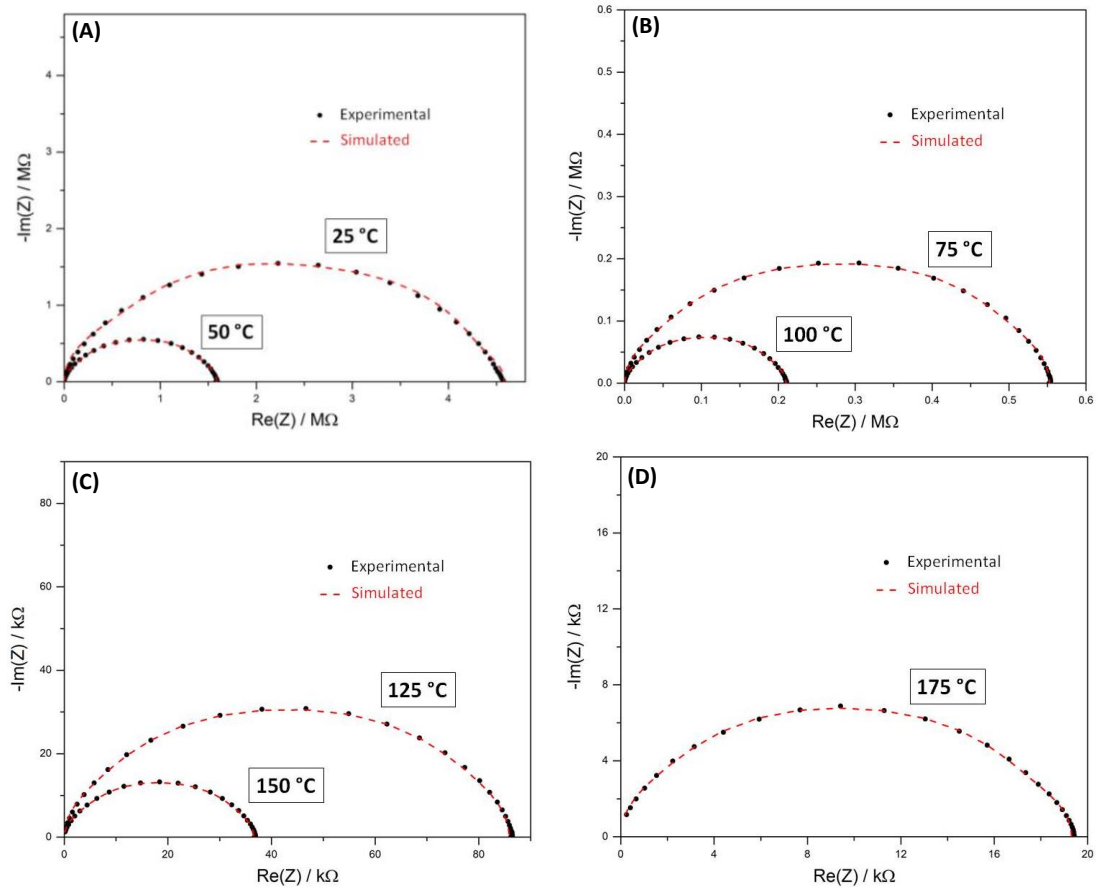*ZFO sample with x = 0.104 ± 0.013 (ZFO_873)*

Fig. B8. Experimental (black spots) and calculated (red dashed line) complex impedance data obtained at **(A)** 25 and 50 °C, **(B)** 75 and 100 °C, **(C)** 125 and 150 °C, and **(D)** 175 °C for a ZFO sample with *x* = 0.104 ± 0.013. The complex impedance data was simulated using the equivalent circuit shown in Fig. B6.

Table B3. Parameters of the elements of the equivalent circuit (Fig. B6) used for the fitting of the complex impedance data obtained for a ZFO sample with $x = 0.104 \pm 0.013$ (Fig. B8). The bulk capacitance ($C_g = C_2$) and resistance ($R_g = R_2$) are highlighted in yellow.

Equivalent Circuit Element	Temperature / °C						
	25	50	75	100	125	150	175
C_1 / F	$1.07\ 10^{-8}$	$5.27\ 10^{-9}$	$5.50\ 10^{-9}$	$4.57\ 10^{-9}$	$3.39\ 10^{-9}$	$2.89\ 10^{-9}$	$4.38\ 10^{-9}$
C_2 / F	$2.76\ 10^{-11}$	$2.76\ 10^{-11}$	$2.70\ 10^{-11}$	$2.70\ 10^{-11}$	$2.73\ 10^{-11}$	$2.82\ 10^{-11}$	$3.40\ 10^{-11}$
C_3 / F	$5.17\ 10^{-11}$	$4.76\ 10^{-11}$	$4.54\ 10^{-11}$	$4.26\ 10^{-11}$	$4.08\ 10^{-11}$	$4.29\ 10^{-11}$	$3.76\ 10^{-11}$
C_4 / F	$2.37\ 10^{-10}$	$1.73\ 10^{-10}$	$1.72\ 10^{-10}$	$1.55\ 10^{-10}$	$1.34\ 10^{-10}$	$1.20\ 10^{-10}$	$1.20\ 10^{-10}$
R_1 / Ω	$1.49\ 10^{6}$	$5.84\ 10^{5}$	$1.90\ 10^{5}$	$7.27\ 10^{4}$	$3.20\ 10^{4}$	$1.56\ 10^{4}$	$6.43\ 10^{3}$
R_2 / Ω	$2.11\ 10^{6}$	$6.02\ 10^{5}$	$2.15\ 10^{5}$	$7.94\ 10^{4}$	$3.05\ 10^{4}$	$1.23\ 10^{4}$	$5.50\ 10^{3}$
R_3 / Ω	$8.12\ 10^{6}$	$2.38\ 10^{6}$	$8.36\ 10^{5}$	$3.10\ 10^{5}$	$1.21\ 10^{5}$	$5.17\ 10^{4}$	$3.27\ 10^{4}$
R_4 / Ω	$7.64\ 10^{6}$	$2.68\ 10^{6}$	$9.01\ 10^{5}$	$3.40\ 10^{5}$	$1.42\ 10^{5}$	$7.02\ 10^{4}$	$3.67\ 10^{4}$

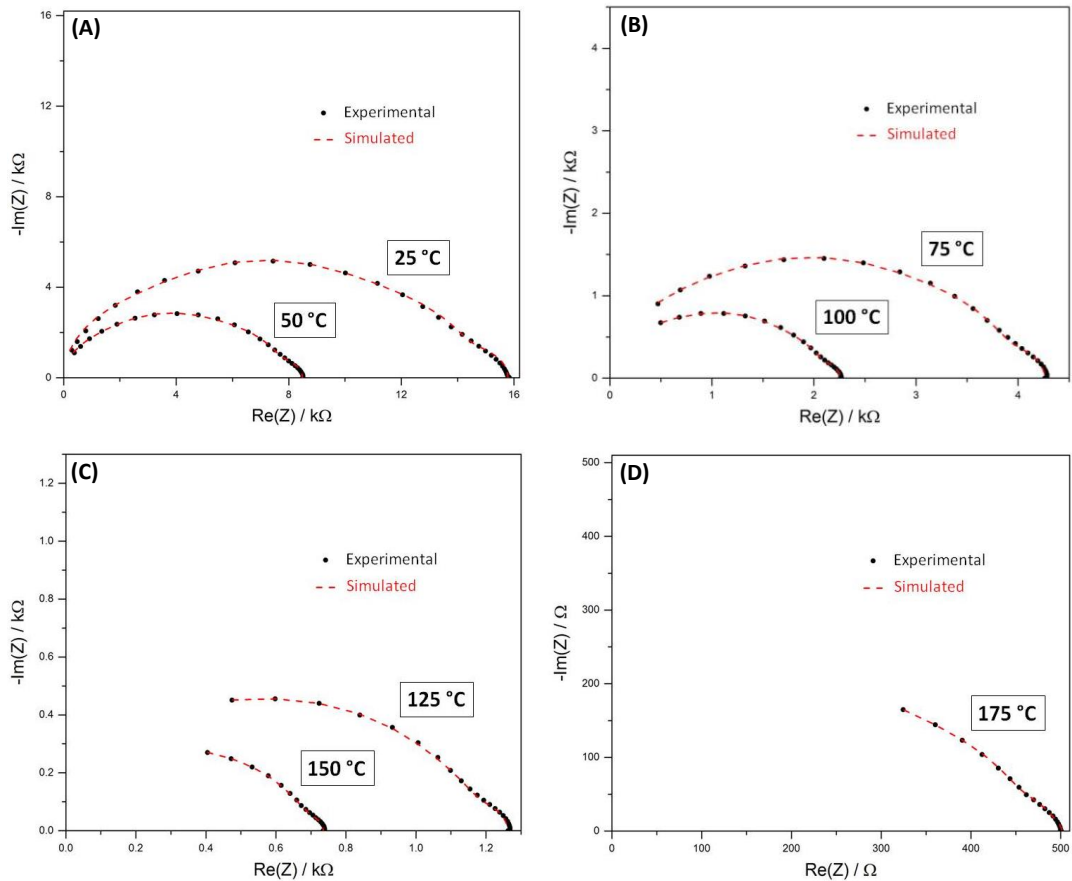***ZFO sample with x = 0.134 ± 0.008 (ZFO_973)***

Fig. B9. Experimental (black spots) and calculated (red dashed line) complex impedance data obtained at **(A)** 25 and 50 °C, **(B)** 75 and 100 °C, **(C)** 125 and 150 °C, and **(D)** 175 °C for a ZFO sample with *x* = 0.134 ± 0.008. The complex impedance data was simulated using the equivalent circuit shown in Fig. B6.

Table B4. Parameters of the elements of the equivalent circuit (Fig. B6) used for the fitting of the complex impedance data obtained for a ZFO sample with $x = 0.134 \pm 0.008$ (Fig. B9). The bulk capacitance ($C_g = C_2$) and resistance ($R_g = R_2$) are highlighted in yellow.

Equivalent Circuit Element	Temperature / °C						
	25	50	75	100	125	150	175
C_1 / F	$1.41\ 10^{-8}$	$3.83\ 10^{-9}$	$3.05\ 10^{-9}$	$2.91\ 10^{-9}$	$2.43\ 10^{-9}$	$2.86\ 10^{-9}$	$3.08\ 10^{-9}$
C_2 / F	$2.48\ 10^{-11}$	$2.63\ 10^{-11}$	$2.66\ 10^{-11}$	$2.71\ 10^{-11}$	$2.75\ 10^{-11}$	$2.60\ 10^{-11}$	$2.65\ 10^{-11}$
C_3 / F	$4.24\ 10^{-11}$	$3.75\ 10^{-11}$	$3.54\ 10^{-11}$	$3.35\ 10^{-11}$	$3.22\ 10^{-11}$	$3.37\ 10^{-11}$	$3.32\ 10^{-11}$
C_4 / F	$2.40\ 10^{-10}$	$1.36\ 10^{-10}$	$1.22\ 10^{-10}$	$1.14\ 10^{-10}$	$1.10\ 10^{-10}$	$1.29\ 10^{-10}$	$1.28\ 10^{-10}$
R_1 / Ω	$2.84\ 10^{5}$	$1.46\ 10^{5}$	$5.37\ 10^{4}$	$1.98\ 10^{4}$	$8.20\ 10^{3}$	$3.20\ 10^{3}$	$1.95\ 10^{3}$
R_2 / Ω	$5.69\ 10^{5}$	$1.49\ 10^{5}$	$4.94\ 10^{4}$	$1.84\ 10^{4}$	$7.61\ 10^{3}$	$4.00\ 10^{3}$	$2.01\ 10^{3}$
R_3 / Ω	$2.12\ 10^{6}$	$6.25\ 10^{5}$	$2.14\ 10^{5}$	$8.23\ 10^{4}$	$3.43\ 10^{4}$	$1.55\ 10^{4}$	$8.05\ 10^{3}$
R_4 / Ω	$1.61\ 10^{6}$	$6.70\ 10^{5}$	$2.35\ 10^{5}$	$8.95\ 10^{4}$	$3.57\ 10^{4}$	$1.39\ 10^{4}$	$7.29\ 10^{3}$

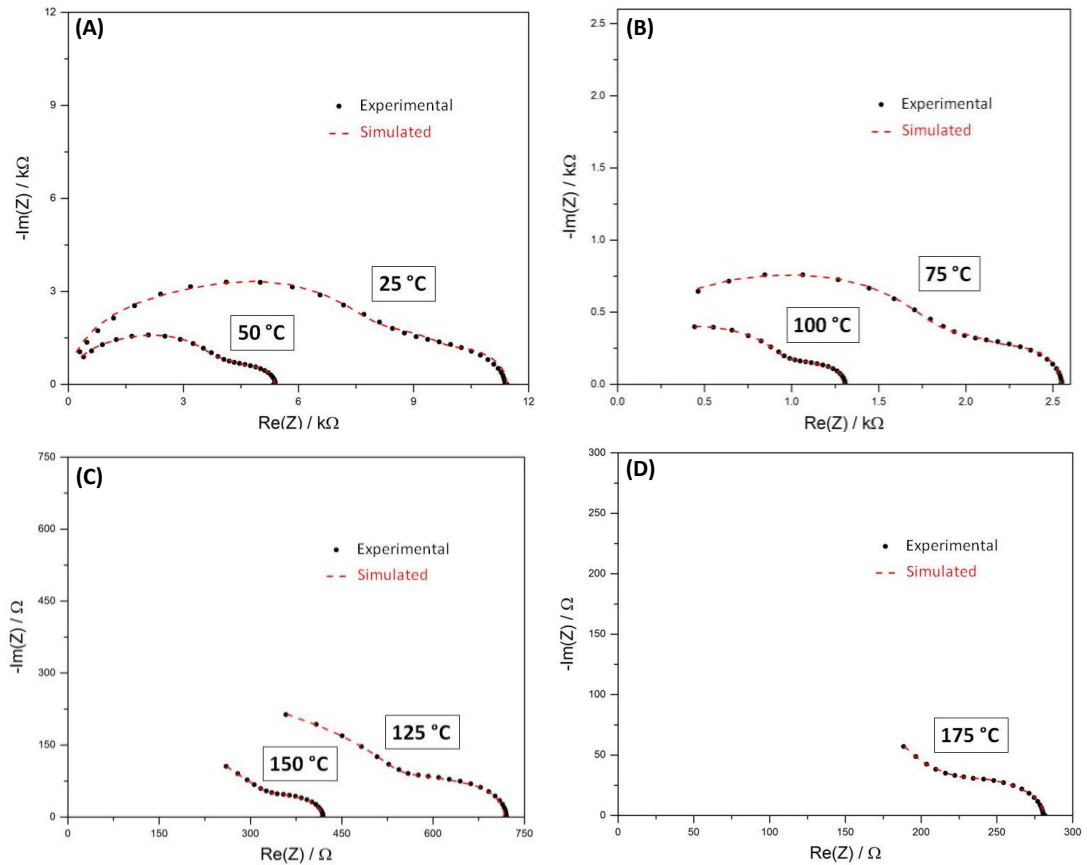*ZFO sample with x = 0.159 ± 0.010 (ZFO_1073)*

Fig. B10. Experimental (black spots) and calculated (red dashed line) complex impedance data obtained at **(A)** 25 and 50 °C, **(B)** 75 and 100 °C, **(C)** 125 and 150 °C, and **(D)** 175 °C for a ZFO sample with x = 0.159 ± 0.010. The complex impedance data was simulated using the equivalent circuit shown in Fig. B6.

Table B5. Parameters of the elements of the equivalent circuit (Fig. B6) used for the fitting of the complex impedance data obtained for a ZFO sample with $x = 0.159 \pm 0.010$ (Fig. B10). The bulk capacitance ($C_g = C_2$) and resistance ($R_g = R_2$) are highlighted in yellow.

Equivalent Circuit Element	Temperature / °C						
	25	**50**	**75**	**100**	**125**	**150**	**175**
C_1 / F	1.06×10^{-8}	7.59×10^{-9}	8.19×10^{-9}	9.66×10^{-9}	1.13×10^{-8}	1.37×10^{-8}	1.42×10^{-7}
C_2 / F	1.94×10^{-11}	2.07×10^{-11}	2.06×10^{-11}	1.99×10^{-11}	1.87×10^{-11}	1.79×10^{-11}	1.79×10^{-11}
C_3 / F	3.92×10^{-11}	3.56×10^{-11}	3.65×10^{-11}	4.44×10^{-11}	6.51×10^{-11}	1.38×10^{-10}	3.04×10^{-10}
C_4 / F	4.26×10^{-10}	2.88×10^{-10}	3.30×10^{-10}	5.29×10^{-10}	1.16×10^{-9}	3.28×10^{-9}	6.41×10^{-9}
R_1 / Ω	1.42×10^{3}	790	369	178	89.8	43.4	10.2
R_2 / Ω	3.22×10^{3}	1.60×10^{3}	913	655	528	443	352
R_3 / Ω	7.71×10^{3}	4.03×10^{3}	2.06×10^{3}	1.06×10^{3}	521	208	101
R_4 / Ω	3.43×10^{3}	2.05×10^{3}	921	364	124	40.6	38.0

*ZFO sample with x = 0.203 ± 0.017 (ZFO_1173)*

Fig. B11. Experimental (black spots) and calculated (red dashed line) complex impedance data obtained at **(A)** 25 and 50 °C, **(B)** 75 and 100 °C, **(C)** 125 and 150 °C, and **(D)** 175 °C for a ZFO sample with x = 0.203 ± 0.017. The complex impedance data was simulated using the equivalent circuit shown in Fig. B6.

Table B6. Parameters of the elements of the equivalent circuit (Fig. B6) used for the fitting of the complex impedance data obtained for a ZFO sample with $x = 0.203 \pm 0.017$ (Fig. B11). The bulk capacitance ($C_g = C_2$) and resistance ($R_g = R_2$) are highlighted in yellow.

Equivalent Circuit Element	Temperature / °C						
	25	**50**	**75**	**100**	**125**	**150**	**175**
C_1 / F	1.48×10^{-8}	1.13×10^{-8}	1.30×10^{-8}	1.56×10^{-8}	1.85×10^{-8}	2.29×10^{-8}	5.12×10^{-8}
C_2 / F	1.98×10^{-11}	1.98×10^{-11}	1.92×10^{-11}	1.85×10^{-11}	1.83×10^{-11}	1.90×10^{-11}	2.00×10^{-11}
C_3 / F	5.75×10^{-11}	5.81×10^{-11}	7.23×10^{-11}	1.11×10^{-10}	2.64×10^{-10}	7.97×10^{-10}	1.63×10^{-9}
C_4 / F	1.50×10^{-9}	1.54×10^{-9}	1.95×10^{-9}	2.59×10^{-9}	3.51×10^{-9}	4.73×10^{-9}	7.69×10^{-9}
R_1 / Ω	1.54×10^3	790	357	171	85.1	42.2	20.6
R_2 / Ω	3.10×10^3	1.56×10^3	895	582	412	282	197
R_3 / Ω	4.88×10^3	2.24×10^3	937	377	131	46.0	28.9
R_4 / Ω	1.91×10^3	799	357	174	89.1	47.7	34.3

Comparison between R₂ and R₃ as the bulk resistance of the ZFO samples
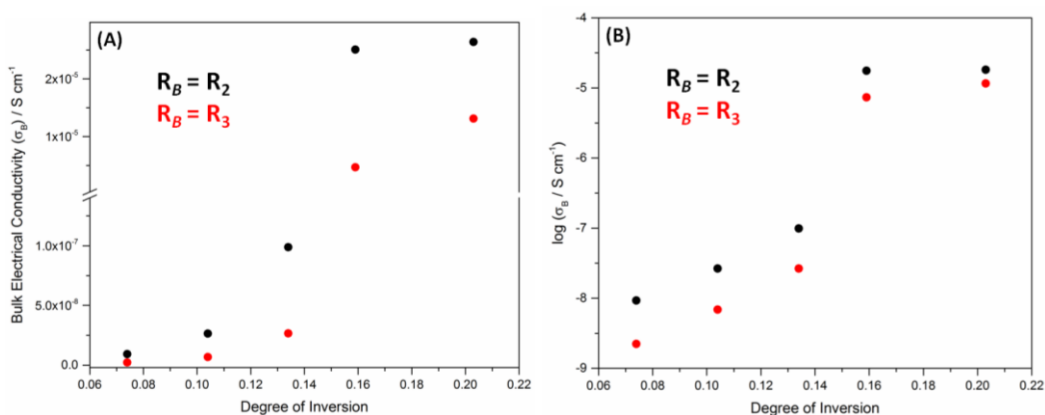
Fig. B12. **(A)** Bulk conductivity and **(B)** logarithm of the bulk conductivity at 298 K obtained when considering R$_2$ (black spots) or R$_3$ (red spots) as the bulk resistance (R_g) of the ZFO samples having different degrees of inversion. The results obtained are in the same order of magnitude and exhibit the same trend whether R$_2$ or R$_3$ are correlated to R_g.

References

(1)   L. I. Granone, A. C. Ulpe, L. Robben, S. Klimke, M. Jahns, F. Renz, T. M. Gesing, T. Bredow, R. Dillert, D. W. Bahnemann, Effect of the Degree of Inversion on Optical Properties of Spinel ZnFe$_2$O$_4$, *Phys. Chem. Chem. Phys.* **2018**, *20*, 28267–28278.

(2)   A. S. Bondarenko, G. A. Ragoisha, Inverse Problem in Potentiodynamic Electrochemical Impedance. In: Progress in Chemometrics Research. A. L. Pomerantsev, Ed.; Nova Science Publishers: New York 2005, pp. 89–102.

(3)   S. K. Mandal, S. Singh, P. Dey, J. N. Roy, P. R. Mandal, T. K. Nath, Frequency and Temperature Dependence of Dielectric and Electrical Properties of TFe$_2$O$_4$ (T = Ni, Zn, Zn$_{0.5}$Ni$_{0.5}$) Ferrite Nanocrystals. *J. Alloys Compds.* **2016**, *656*, 887–896.

(4)   N. Ponpandian, A. Narayanasamy, Influence of Grain Size and Structural Changes on the Electrical Properties of Nanocrystalline Zinc Ferrite. *J. Magn. Magn. Mater.* **2002**, *92*, 2770–2778.

(5)   H. Inaba, Impedance Measurement of Single-crystalline and Polycrystalline Manganese–zinc Ferrites with Various Non-stoichiometries. *J. Mater. Sci.*

1997, *32*, 1867–1872.

(6)   Y. P. Jiang, R. Li, X. G. Tang, Q. X. Liu, D. G. Chen, Dielectric Relaxation Behavior in Co-precipitation Derived Ferrite $(Zn_{1-x}Ni_x)Fe_2O_4$ $(0.2 \leq x \leq 0.5)$ Ceramics. *Mod. Phys. Lett. B* **2016**, *30*, 1550277.

(7)   D. Venkatesh, K. V. Ramesh, C. V. S. S. Sastry, Effect of Sintering Temperature on Micro Structural and Impedance Spectroscopic Properties of $Ni_{0.5}Zn_{0.5}Fe_2O_4$ Nano Ferrite. *AIP Conf. Proc.* **2017**, *1859*, 020035.

(8)   D. G. Chen, X. G. Tang, Q. X. Liu, Y. P. Jiang, C. B. Ma, R. Li, Impedance Response and Dielectric Relaxation in Co-precipitation Derived Ferrite $(Ni,Zn)Fe_2O_4$ Ceramics. *J. Appl. Phys.* **2013**, *113*, 214110.

(9)   A. Mekap, P. R. Das, R. N. P. Choudhary, Dielectric, Magnetic and Electrical Properties of $ZnFe_2O_4$ Ceramics. *J. Mater. Sci.: Mater. Electron.* **2013**, *24*, 4757–4763.

(10)   M.-R. Syue, F.-J. Wei, C.-S. Chou, C.-M. Fu, Magnetic, Dielectric, and Complex Impedance Properties of Nanocrystalline Mn–Zn Ferrites Prepared by Novel Combustion Method. *Thin Solid Films* **2011**, *519*, 8303–8306.

(11)   M. J. Akhtar, M. Younas, Structural and Transport Properties of Nanocrystalline $MnFe_2O_4$ Synthesized by Co-precipitation Method. *Solid State Sci.* **2012**, *14*, 1536–1542.

(12)   D. K. Pradhan, P. Misra, V. S. Puli, S. Sahoo, D. K. Pradhan, R. S. Katiyar, Studies on Structural, Dielectric, and Transport Properties of $Ni_{0.65}Zn_{0.35}Fe_2O_4$. *J. Appl. Phys.* **2014**, *115*, 243904.

(13)   Ž. Z. Lazarević, Č. Jovalekić, A. Milutinović, D. Sekulić, M. Romčević, M. Slanakamenac, N. Romčević, Spectroscopy Investigation of Nanostructured Zinc Ferrite Obtained by Mechanochemical Synthesis. *Optoelectron. Adv. Mat.* **2013**, *7*, 720–725.

(14)   Ž. Z. Lazarević, Č. Jovalekić, D. L. Sekulić, A. Milutinović, S. Baloš, M. Slankamenac, N. Ž. Romčević, Structural, Electrical and Dielectric Properties of Spinel Nickel Ferrite Prepared by Soft Mechanochemical Synthesis. *Mater. Res. Bull.* **2013**, *48*, 4368–4378.

List of Publications

Granone L. I., Nikitin K., Emeline A., Dillert R., Bahnemann D. W. Effect of the Degree of Inversion on the Photoelectrochemical Activity of Spinel $ZnFe_2O_4$. *Catalysts* **2019**, 9, 434.

AlSalka Y., **Granone L. I.**, Ramadan W., Hakki A, Dillert R., Bahnemann D. W. Iron-Based Photocatalytic and Photoelectrocatalytic Nano-Structures: Facts, Perspectives, and Expectations. *Applied Catalysis B: Environmental* **2019**, 244, 1065-1095.

Tolosana-Moranchel A., Casas J. A., Bahamonde A., Pascual L., **Granone L. I.**, Schneider J., Dillert R., Bahnemann D. W. Nature and Photoreactivity of TiO_2-rGO Nanocomposites in Aqueous Suspensions under UV-A Irradiation. *Applied Catalysis B: Environmental* **2019**, 241, 375-384.

Granone L. I., Dillert R., Heitjans P., Bahnemann D. W. Effect of the Degree of Inversion on the Electrical Conductivity of Spinel $ZnFe_2O_4$. *ChemistrySelect* **2019**, 4, 1232-1239.

Curti M, Kirsch A., **Granone L. I.**, Tarasi F, López-Robledo G., Bahnemann D. W., Murshed M. M., Gesing Th. M., Mendive C. B. Visible-Light Photocatalysis with Mullite-Type $Bi_2(Al_{1-x}Fe_x)_4O_9$: Striking the Balance between Bandgap Narrowing and Conduction Band Lowering. *ACS Catalysis* **2018**, 8, 8844-8855.

Arimi A., Megatif L., **Granone L. I.**, Dillert R., Bahnemann D. W. Visible-Light Photocatalytic Activity of Zinc Ferrites. *Journal of Photochemistry and Photobiology A: Chemistry* **2018**, 366, 118-126.

Granone L. I., Ulpe A. C., Robben L., Klimke S., Jahns M., Renz F., Gesing Th. M., Bredow Th., Dillert R., Bahnemann D. W. Effect of the Degree of Inversion on Optical Properties of Spinel $ZnFe_2O_4$. *Physical Chemistry Chemical Physics* **2018**, 20, 28267-28278.

Selvamani T., Anandan, S., **Granone L. I.**, Bahnemann D. W., Ashokkumar, M. Phase-Controlled Synthesis of Bismuth Oxide Polymorphs for Photocatalytic Applications. *Materials Chemistry Frontiers* **2018**, 2, 1664-1673.

Granone L. I., Sieland F., Zheng N., Dillert R., Bahnemann D. W. Photocatalytic Conversion of Biomass into Valuable Products: A Meaningful Approach?. *Green Chemistry* **2018**, 20, 1169-1192.

Curriculum Vitae

Personal Data

Surname, forename	**Granone, Luis Ignacio**
Date of birth	**May 11th, 1989**
Place of Birth	**Mar del Plata, Argentine Republic**

Academic Background

Mar. 25th, 2019	**Dr. rer. nat.** degree. Overall grade: *with distinction*. Institut für Technische Chemie, Leibniz Universität Hannover.
Feb. 2016 – Mar. 2019	**Ph.D. Study in Chemistry** at the Institut für Technische Chemie, Leibniz Universität Hannover.
Nov. 25th, 2015	**Licenciado en Química**. Outstanding graduate diploma. National University of Mar del Plata, Argentine Republic.
Mar. 2009 – Oct. 2015	**Study of Chemistry** at the National University of Mar del Plata, Argentine Republic.
Mar. 2005 – Dec. 2007	**High School** at Colegio San Agustín, Mar del Plata, Argentine Republic.